Assessing the Connectivity of Groundwater Wells to Surface-Water Using a Volumetric Capture Delineation Tool

by

Mashrur Anam Chowdhury

A thesis
presented to the University of Waterloo
in fulfillment of the
thesis requirement for the degree of
Master of Applied Science
in
Civil Engineering (Water)

Waterloo, Ontario, Canada, 2016

I hereby declare that I am the sole author of this thesis. This is a true copy of the thesis, including any required final revisions, as accepted by my examiners.

I understand that my thesis may be made electronically available to the public.

Abstract

Existing groundwater modeling methods for determining the degree of groundwater well connectivity to surface-water either provide weak guidance (i.e., analytical methods), only examine the hydrological impacts of pumping (i.e., mapping method developed by Leake et al. (2010)), or are too computationally expensive (i.e., solute transport modeling methods) (Ceric & Haitjema, 2005). As such, a modeling technique is required that can accurately estimate the amount of water a particular well sources from surface-water at low computational costs. Here, we present some novel applications of a software tool called FlowSource (Black and Foley, 2013) in assessing well and surface-water connectivity. FlowSource is a MODFLOW-based (Harbaugh et al., 2000) software and can completely describe the flow connectivity between specified parts of the aquifer system without the use of particle tracking or advective transport simulation.

First, an algorithm was developed to reduce numerical dispersion in FlowSource calculations that result from the assumption of fully mixed groundwater model cells. For any given set of flows along the faces of a three-dimensional rectilinear finite-difference groundwater model cell, the algorithm can evaluate the volumetric flow from each inflow face to each outflow face by either applying mass balance inside the cell or analytically recreating the internal streamtube geometry using the semi-analytical particle tracking method developed by Pollock (1988). The calculations of the algorithm are exact. The algorithm may be applied on a cell-by-cell basis to establish the volumetric flow connections inside the cell before performing the flow connectivity calculations in FlowSource. Its potential to reduce numerical dispersion in FlowSource calculations is demonstrated with a hypothetical example.

Second, a novel FlowSource-based modeling tool was developed for assessing well and surface-water connectivity. The tool deploys FlowSource within the framework of the mapping method developed by Leake et al. (2010) (the LRD method). The differences in the results of the novel tool and the LRD method are demonstrated. Numerous applications of the modeling tool are demonstrated using a synthetic model, which include the ability to rapidly: (1) screen for wells that are surface-water dominated and are at risk of contamination from non-point sources, (2) infer the volume of water removed by pumpage from surface-water and, (3) generate diagnostic maps that illustrate how the location and time of pumping affects: (a) volumetric connectivity with surface-water, (b) the connectivity of existing wells to surface-water and, (c) hyporheic flows.

Most importantly, the use of FlowSource enables these assessments to be performed without performing any solute transport modeling. Hence, the modeling tool developed here has the potential to aid water managers to inexpensively assess the risks posed to public health and/or the local environment of existing and planned pumping operations so that they can effectively prioritize monitoring and modeling efforts.

Acknowledgements

First and foremost I would like to thank my supervisor, Dr. James Craig, for guiding me along every step of the way through my graduate studies. He is an immense reservoir of knowledge and ideas, two of which sprouted the work in this thesis, and I am truly grateful to have had the opportunity to work with him.

I would like to thank Alastair Black and Chris Foley from Groundwater Science Ltd. for answering all my questions regarding FlowSource and collaborating with us.

Finally, I would like to thank Mukita Chowdhury for her constant support and encouragement. She helped me stay on course and get over the finish line.

Dedication

This is dedicated to my parents. The opportunities I have today came at the cost of your collective sacrifices. Thank you.

Table of Contents

List of Figures viii
List of Tables xiii
Introduction 1
1.1 Overview 1
1.2 Problem Statement 5
1.3 Thesis Objective 5
1.4 Scope of Research 6
1.5 Thesis Outline 7
Background 9
2.1 Interaction of groundwater withdrawal wells and surface-water bodies 9
2.1.1 Well Withdrawal Impacts on Surface-water 9
2.1.2 Groundwater Under Direct Influence of Surface-water (GUDI) 11
2.2 Groundwater and Solute Transport Modeling 13
2.2.1 Overview 13
2.2.2 MODFLOW 15
2.2.3 Particle Tracking 16
2.3 Determining Connectivity of Groundwater Wells and Surface-Water Bodies 18
2.3.1 Capture Zone Delineation 18
2.3.2 Capture-Fraction Mapping (the LRD Method) 21
2.3.3 Flow-Based Capture Delineation 23
2.4 FlowSource 24
2.4.1 FlowSource Method 25
2.4.2 Current and Future Applications 29
2.4.3 Sources of Errors 31
Methodology 32
3.1 Reducing Numerical Dispersion in FlowSource 32
3.2 Pollock's Method 33
3.3 Computing Flow Connections in a Two-Dimensional Rectilinear Cell (2D-Algorithm) 37
3.3.1 Trivial Cases 39
3.3.2 Two Inflows-Two Outflows 39

3.3.3 All Other Cases 51
3.3.4 Summary of 2D-Algorithm 54
3.4 Computing Flow Connections in a Three-Dimensional Rectilinear Cell 56
3.4.1 Trivial Cases 56
3.4.2 Single Inflow and/or Single Outflow 57
3.4.3 Stagnation Point Cases 59
3.4.4 Cases compatible with 2D-Algorithm 63
3.4.5 All Other Cases (Streamtube Recreation Cases) 64
3.4.6 Summary of Algorithm 80
3.4.7 Sources of Errors 84
3.5 Determining connectivity of wells and surface-water features 87
3.5.1 Determining Volumetric Contribution from Features of Interest 88
3.5.2 Incorporation of Mapping Capabilities 89
Results and Discussion 93
4.1 Application of Algorithm to Compute Volumetric Flow Connections in a Three-Dimensional Rectilinear Cell 93
4.1.1 Single Cell Test Cases 93
4.1.2 Reduction of Numerical Dispersion in FlowSource 99
4.2 Comparison with the LRD Method 104
4.2.1 Single Stream Case 105
4.2.2 Two Stream Case 110
4.3 Applications for Screening Existing Wells 118
4.3.1 Assessing Connectivity to Surface-Water 118
4.3.2 Assessing Connectivity to Non-Point Source Pollution 125
4.4 Applications for Planning New Well Sites 127
4.4.1 Volumetric Capture-Fraction Contour Maps 127
4.4.2 Impact of Seasonality 131
4.4.3 Impact on Existing Wells 132
4.4.4 Impact on Hyporheic Flows 134
Conclusions and Recommendations 137
References 141

List of Figures

Figure 2.1. Interaction of a groundwater well and a stream (modified from Winter et al., 1998).10

Figure 2.2. Model discretization in MODFLOW-2005 (modified from Harbaugh, 2005). 16

Figure 2.3. An example capture-fraction map (modified from Leake et al., 2010). 22

Figure 2.4. Cell-by-cell flows from a hypothetical groundwater flow model (modified from Foley and Black, 2013). 25

Figure 2.5. Directed graph representation of cell-by-cell flows from the example in Figure 2.4 (modified from Foley and Black, 2013). 26

Figure 2.6. Nodes from directed graph sorted topographically in order of downstream flow (Figure from Foley and Black, 2013). 26

Figure 2.7. Calculated FlowSource metrics for the cell-by-cell flows from the example in Figure 2.4 (modified from Foley and Black, 2013). 27

Figure 2.8. Directed graph with horizontal edge between nodes B and C reversed (modified from Foley and Black, 2013). 28

Figure 2.9. New topological sorting of nodes in order of downstream flow (Figure from Foley and Black, 2013). 28

Figure 2.10. Impact of competing abstraction pressures on well capture zones (modified from Black and Foley, 2013) 30

Figure 3.1. Orientation of finite-difference cell and definition of cell face flows (Figure from Pollock, 1988). 33

Figure 3.2 A particle being tracked through a two-dimensional cell from (x_p, y_p) at time t_p to its exit (x_e, y_e) at time t_e (Figure from Pollock, 1988). 37

Figure 3.3. Orientation of a two-dimensional finite-difference cell and definition of cell face flows. 38

Figure 3.4. Schematics of some trivial case. 39

Figure 3.5. Schematics of the two general flow regime types of two inflows-two outflows. 40

Figure 3.6. Schematic of Case 1A. 41

Figure 3.7. Plot of velocity profile along *x*-axis for Case 1A. 42

Figure 3.8. Schematic of Case 1B. 44

Figure 3.9. Plot of velocity profile along y-axis for Case 1B. 45

Figure 3.10. Schematics of the three potential flow regimes for Case 2A. 47

Figure 3.11. Three examples of remaining cases. 51

Figure 3.12. Flow chart of algorithm for computing volumetric flow connections in a two-dimensional rectilinear finite-difference cell. 55

Figure 3.13. Schematics of trivial cases for three-dimensional cell. 57

Figure 3.14. Example of a single outflow case for a three-dimensional rectilinear finite-difference cell of unit dimensions. 58

Figure 3.15. Example of a single inflow case for a three-dimensional rectilinear finite-difference cell of unit dimensions. 59

Figure 3.16. Examples of stagnation point cases for a three-dimensional rectilinear finite-difference cell. 60

Figure 3.17. Three-dimensional stagnation point case with six non-zero flows. 61

Figure 3.18. Examples of three-dimensional cases that are compatible with the 2D-algorithm. . 63

Figure 3.19. An example of a case for which the internal streamtube geometry has to be recreated to determine volumetric flow connections (a); 50 particles forward tracked using Pollock's method from each inflow edge (b). 65

Figure 3.20. Cell face $y1$ (x-z face at $y = 0$) from the cell in Figure 3.19. 65

Figure 3.21. Throughflow and non-throughflow areas on cell face $y1$ (x-z face at $y = 0$) from the cell in Figure 3.19. 67

Figure 3.22. Developing analytically integrable expression for adjacent curves. 68

Figure 3.23 Developing analytically integrable expression for opposite curves. 72

Figure 3.24. Determining limits of flow connection area curves as per conditions 1 and 2. 77

Figure 3.25. Determining limits of flow connection area curves as per condition 3. 79

Figure 3.26. Flow chart of algorithm for computing volumetric flow connections in a three-dimensional rectilinear finite-difference cell. 82

Figure 3.27. Flowchart of algorithm for determining volumetric flow connections by analytically recreating internal streamtube geometry. 83

Figure 3.28. Examples of cases with zero-velocity gradients inside cell. 86

Figure 3.29. Graph illustrating the sensitivity in the accuracy of flow calculations to the magnitude of flow correction for the cases shown in Figure 3.28. 87

Figure 3.30. Steps to generate a contour map. 91

Figure 4.1. Cell-by-cell flows from a planar flow field with a SE-NW downward gradient. 99

Figure 4.2. Directed acyclic graph for the cell-by-cell flows shown in Figure 4.1. 100

Figure 4.3. FlowSource cell-by-cell fraction-through values for a three row-three column grid with planar flow under fully-mixed assumption. 100

Figure 4.4. Internal streamtubes recreated by forward tracking inflow corners inside each cell using Pollock's method. 101

Figure 4.5. Directed acyclic graph with flows represented as inter-cell flows. 102

Figure 4.6. FlowSource cell-by-cell fraction-through values for a three-row three-column grid with planar flow after revoking fully-mixed assumption. 103

Figure 4.7. Steady-state head distribution without any pumping wells for single stream case. . 106

Figure 4.8. Head distributions of single stream case after one year for pumping at 5000 m^3/d immediately adjacent to the stream (a), midway along the model domain (b), and furthest away from the stream (c). 107

Figure 4.9. Graph of LRD-capture, increased stream leakage, and reduced baseflow fractions along column 5 of the single stream case model. 108

Figure 4.10. Contour maps of increased stream leakage component of LRD-capture fraction (a), and volumetric-capture fraction (b) for single stream case. 109

Figure 4.11. Graph of increased stream leakage component of LRD-capture fraction and volumetric-capture fraction along column 5 of the single stream case model. 110

Figure 4.12. Steady-state head distribution without any pumping wells for two stream case.... 111

Figure 4.13. Head distributions of two stream case after one year for pumping at -20,000 m^3/d at row 2 (a), row 15 (b), and row 31 (c). 112

Figure 4.14. Contour maps of LRD-capture fraction (a), reduced baseflow fraction (b), increased stream leakage fraction (c), and volumetric-capture fraction (d) for two stream case. 113

Figure 4.15. Graph of increased stream leakage component of LRD-capture fraction and volumetric-capture fraction along column 5 of the two stream case model. 113

Figure 4.16. Contour maps of increased stream leakage component of LRD-capture fraction (a) and volumetric-capture fraction (b) for stream A (the losing stream). 114

Figure 4.17. Graph of increased stream leakage component of LRD-capture fraction and volumetric-capture fraction along column 5 for stream A (the losing stream)..... 115

Figure 4.18. Contour maps of increased stream leakage component of LRD-capture fraction (a) and volumetric-capture fraction (b) for stream B (the gaining stream). 116

Figure 4.19. Graph of increased stream leakage component of LRD-capture fraction and volumetric-capture fraction along column 5 for stream B (the gaining stream)..... 116

Figure 4.20. MODFLOW-2000 model of synthetic well field case: steady-state head distributions shown for layer 1 (a), layer 2 (b) and the cross-section along row 1 (c). 120

Figure 4.21. Map illustrating the connectivity of wells and the steam for the synthetic well field model..... 122

Figure 4.22. Map illustrating connectivity of wells to specified features of interest..... 123

Figure 4.23. Daily rate of water removal by each well from features of interest (a), and the cumulative daily rates of water removal from each feature of interest (b). 124

Figure 4.24. Map illustrating the fraction of recharge obtained by each well from adjacent farms. 126

Figure 4.25. Contour maps of fractional volumetric capture from the whole stream after 180 days of pumping at 2,000 m^3/d along layer 1 (a), and layer (2). 128

Figure 4.26. Specified reaches of interest along the stream for contour maps. 129

Figure 4.27. Contour maps of fractional volumetric capture from the main tributary after 180 days of pumping at 2,000 m^3/d along layer 1 (a), and layer (2). 129

Figure 4.28. Contour maps of fractional volumetric capture from the Western tributary after 180 days of pumping at 2,000 m^3/d along layer 1 (a), and layer (2). 130

Figure 4.29. Contour maps of fractional volumetric capture from the Eastern tributary after 180 days of pumping at 2,000 m^3/d along layer 1 (a), and layer (2). 130

Figure 4.30. Contour maps of fractional volumetric capture from whole stream after 180 days of pumping at 11,000 m^3/d along layer 2 under uniform areal recharge of 2e-03 m/d (a), 1e-03 m/d (b), and 5e-04 m/d (c). 131

Figure 4.31. Locations of Well A and Well E. 132

Figure 4.32. Change in volumetric-capture fraction in Well E (a), and Well A (b) for pumping at 11,000 m^3/d along layer 2 for 180 days. 133

Figure 4.33. Manifestation of hyporheic zones due to abrupt changes in streambed slope (a) and stream meanders (b) (modified from Winter et al., 1998) 134

Figure 4.34. Potential hyporheic zone between Reach A and Reach B of the synthetic model. 135

Figure 4.35. Change in hyporheic flow (m^3/d) from Reach A to Reach B after 180 days for pumping at 11,000 m^3/d along layer 2. 136

List of Tables

Table 2.1. Conditions for GUDI well determination under Ontario's Terms of Reference for Hydrogeological Study to Examine Groundwater Sources Potentially Under Direct Influence of Surface-water (2001). 12

Table 4.1. Results for three special cases. 96

Table 4.2. Results for three general cases. 97

Table 4.3. Results for two zero-velocity gradient cases. 98

Table 4.4. Inter-cell flows from hypothetical case expressed as constituent flows. 102

Table 4.5. Model details for single stream case. 105

Table 4.6. Model details for two stream case. 110

Table 4.7. Model details of synthetic well field case. 119

Table 4.8. Well locations and pumping rates of synthetic well field case 119

Table 4.9. FlowSource results for synthetic well field case 121

Chapter 1

Introduction

1.1 Overview

Groundwater wells which derive some or all of their water directly from surface-water sources are referred to as "groundwater under the direct influence of surface-water" (GUDI or GWUDI) wells. GUDI wells are particularly susceptible to contamination from pathogens and pollutants typically present in surface-water (Medema et al., 2003). In addition, pumping from wells hydraulically connected to streams, lakes, and wetlands may adversely affect local ecosystems and downstream water supplies by depleting water levels. Thus, it is important to be able to determine the degree of connectivity and interaction between groundwater wells and adjacent surface-water features in order to protect both water quality and quantity (Winter et al., 1998).

The identification and management of GUDI wells assumed new importance particularly in Canada following the Walkerton tragedy in 2000, when seven people died and 2,300 fell ill after a drinking water well became contaminated from adjacent farm runoff in Walkerton, Ontario (Frind et al., 2002). Soon after, the Ontario government passed the Safe Drinking Water Act in 2002 to ensure GUDI wells receive adequate treatment before discharging to public water systems. This was followed by the Clean Water Act in 2006 to protect existing and future sources of drinking water. As a part of the Clean Water Act, all existing and planned drinking water supply wells deemed to be GUDI are required to be regulated and monitored (Government of Ontario 2002; Ontario Ministry of Environment 2008). Similar laws were also passed in other

provinces in Canada and elsewhere internationally (Government of Alberta 2003; Government of Saskatchewan 2002; USEPA 1992).

A problem in Canada, and elsewhere, is the large number of groundwater supply wells that are in close proximity to surface-water features and which may need to be regulated as GUDI. Also, with increasing demand for water, it is inevitable that the development of new groundwater resources will require drilling wells adjacent to some surface-water features. Thus, water managers must ideally be able to screen for wells that are likely to develop connections to surface-water before commencing any costly field testing and monitoring programs.

Groundwater modelling can be a potentially useful component of the screening process. This involves using a groundwater model to delineate the capture zone of a well or a well field. A capture zone of a well is the physical area of the subsurface and surface from which it obtains its water from over a given time period. Capture zone delineation methods may range from simply drawing a circle of fixed-radius around the well to sophisticated groundwater flow and solute transport modeling (Ceric and Haitjema, 2005). Standard capture zone delineation approaches are often complicated by the presence of surface-water features and it is typically difficult to assess the degree of connections between wells and surface-water using the simpler methods.

Some provincial GUDI assessment schemes suggest conducting groundwater modeling investigations as part of the screening process. However, others recommend monitoring and testing programs begin immediately after carrying out a rapid screening process that involves assessing available well construction, well water quality and aquifer data (Alberta Environment 2006; B.C. Ministry of Health 2015; Govt. of Newfoundland and Labrador 2013; Nova Scotia Environment 2002; Saskatchewan Environment 2004). This is in part because at present,

available modeling techniques are either too simplistic (i.e., fixed-radius approach or analytical methods) and cannot provide any additional insights above those generated by the rapid screening processes or too computationally involved (i.e., particle tracking and solute transport methods) and do not offer any significant reductions in the cost of assessment (Ceric and Haitjema, 2005). Thus, what is desirable is a scientifically rigorous yet inexpensive modeling technique to determine the degree of connectivity of wells and surface-water features.

Here, a novel modeling tool is presented that has the potential to fill this need. The tool derives from a mapping method developed by Leake et al. (2010) which can map the hydrological impacts of pumping on surface-water, referred to here as the LRD method, and FlowSource (Black and Foley, 2013), which is a MODFLOW-based (Harbaugh et al., 2000) software tool that can completely describe the flow connectivity between specified parts of the aquifer system. The LRD method is here extended to map the degree of hydraulic connectivity between wells and surface-water source areas (i.e., rivers, lakes, and recharge areas) using FlowSource. The utility of the tool is provided by FlowSource. FlowSource takes in the cell-by-cell flows obtained from a MODFLOW finite-difference groundwater flow model and represents them as a directed acyclic graph (DAG). The use of DAGs is considered unique and it enables FlowSource to explicitly calculate the volume of water from each groundwater model cell that reaches user-defined ‘destination cell(s)’ without the use of any particle tracking or solving the solute transport equation. As such, FlowSource has very fast run times. In addition, FlowSource can group a large number of cells into destination cells and process them simultaneously without notable increases in setup or run times and the destination cells need not necessarily be a point of abstraction or even be adjacent to one another (Black and Foley, 2013). This makes FlowSource particularly suitable for analyzing the connectivity of groundwater wells to surface-water

features. However, an important limitation of FlowSource is that its calculations are sensitive to the model grid size and orientation. FlowSource implicitly assumes that all flows in each groundwater model cell are fully mixed and this can cause numerical dispersion in its calculations when using coarse grids.

The first of part of this thesis describes the development of a novel method in order to address the numerical dispersion issues in FlowSource. The method determines the volumetric flow connections within a three dimensional rectilinear finite-difference groundwater model cell using either mass balance or by analytical recreation of the internal streamtube geometry and thereby offers a suitable alternative to invoking the fully mixed assumption. The dividing streamtubes inside the cell are recreated analytically using extensions of the equations from Pollock's semi-analytical particle tracking method (Pollock, 1988).

The second part of the thesis discusses the novel modeling tool and some of its applications for analyzing well connectivity to surface features are presented. The tool enables the estimation of the volume (or percentage) of well water that is sourced from surface features such as surface-water bodies or agricultural lands (as opposed to aquifer storage) without requiring any particle tracking or solute transport modeling. Consequently, this connectivity metric can be generated for a large number of wells and/or a large area in a relatively short time frame and offers simultaneous insights into the vulnerability of the well and its hydrological impact on surface-water. The results can be outputted to a simple table for existing well fields showing the well location or identifier and the volume (or percentage) of water it draws from user-specified features of interest, or to generate contour maps for a new planned well, showing the spatial distribution of the volumetric contribution from user-specified features of interest to the well. The simple mechanics and outputs of the tool may be easily communicated to non-technical

stakeholders. Thus, it has the potential to serve as a useful screening and planning tool with which water managers can effectively focus data collection efforts at reduced costs of assessment.

1.2 Problem Statement

FlowSource (Black and Foley, 2013) is a capture delineation software that can delineate groundwater flow pathways volumetrically without the use of particle tracking or advective transport simulation. However, its calculations are sensitive to the model grid size because it implicitly assumes that all flows are fully mixed inside each model cell. Thus, a solution is warranted that can accurately determine how flows are distributed in a three-dimensional rectilinear finite-difference cell for any set of flows along the cell faces (i.e., the volumetric flow connections between all the cell faces). The solution must also be computationally inexpensive so as not to significantly compromise the performance of FlowSource.

On a separate note, water managers need a modeling tool that will enable them to rapidly screen for wells which pose risks to public health and/or the local environment so that they can effectively prioritize modeling and monitoring efforts. Hence, the tool must be able to accurately determine the degree of connectivity of wells to surface-water features at low computational costs.

1.3 Thesis Objective

The objective of this thesis is twofold. The first is to **develop and test a method that can reduce numerical dispersion in FlowSource (Black and Foley, 2013) calculations**. For any given set of flows along the faces of a three-dimensional rectilinear finite-difference groundwater model cell, the method evaluates the volumetric flow from each inflow face to each outflow face

by either applying mass balance inside the cell or by analytically recreating the internal streamtube geometry using the semi-analytical particle tracking method developed by Pollock (1988). Its potential to reduce numerical dispersion in FlowSource calculations will be demonstrated with a simple hypothetical example.

The second objective of this thesis is to **develop and test a novel FlowSource-based modeling tool that can explicitly determine the volume of water in a well that is sourced from surface-water features without the use of particle tracking or solute transport modeling**. This novel tool uses FlowSource within the framework of the LRD method (Leake et al., 2010). The differences in the results of the novel tool and the LRD method will be demonstrated. With the use of some simple synthetic models, the thesis will also attempt to demonstrate the ability of the tool (1) to screen for potentially vulnerable and/or ecologically harmful wells from an existing well field and, (2) to generate maps from which the risks to public health and adverse impacts on local ecology can be inferred for new pumping operations.

1.4 Scope of Research

The method to compute volumetric flow connections inside a groundwater model cell is restricted to rectilinear grids. In addition, it assumes quasi-steady-state flow (i.e., in the instant in which the flows are computed, they are steady-state) and that there is no internal removal or addition of water inside the cell for which the volumetric connections are computed (i.e., there are no weak sinks or sources present inside the cell). The incorporation of the method into FlowSource (Black and Foley, 2013) is also beyond the scope of this research.

The modeling tool is exclusively MODFLOW-based (Harbaugh et al., 2000) and thus it inherits all the assumptions embedded in the conceptualization of MODFLOW. Also, currently the tool can only handle features of interest that are contained entirely within one model layer.

Finally, the application of the modeling tool to a real world model and a comparison of its performance to solute transport modeling approaches and/or tracer studies were also considered outside the scope of this research.

1.5 Thesis Outline

The thesis outline is as follows:

Chapter 1 provides the motivation behind the development of the modeling tool and the method to determine the volumetric flow connections inside a three-dimensional rectilinear finite-difference groundwater model cell. It discusses the need for a quality screening tool for estimating the connectivity of wells and adjacent surface-water features. The suitability of FlowSource (Black and Foley, 2013) to assess well and surface-water connectivity is also briefly discussed and the source of its numerical dispersion issues is introduced. Finally, the objectives and the scope of this research are defined.

Chapter 2 presents a general overview of well and surface-water interactions and, groundwater and solute transport modeling. It also provides background information on the different approaches available to assess well and surface-water connectivity, where the LRD method (Leake et al., 2010) is introduced. Afterwards, the calculation method used in FlowSource is described in length and some of its applications and the source of numerical dispersion in its calculations are also discussed.

Chapter 3 provides an explanation of Pollock's method (Pollock, 1988) and a detailed description of the development of the algorithm to reduce numerical dispersion in FlowSource. This is followed by a description of how FlowSource can be used to determine the volume of well water derived from surface-water sources and how it can be deployed within the framework of the LRD method to generate maps for assessing well and surface-water connectivity.

Chapter 4 presents results demonstrating the performance of the algorithm and some applications of the modeling tool. First, the results of a few single cell test cases are presented to demonstrate the performance of the algorithm in evaluating volumetric flow connections within a single model cell. Next, a hypothetical example is presented to show how the algorithm may reduce numerical dispersion in FlowSource calculations. As for the modeling tool, a synthetic model is used to demonstrate its applications for screening an existing well field based on volumetric connectivity to surface-water features and non-point sources of pollution (i.e., agricultural lands). The same synthetic model is then used to generate maps with the modeling tool that show the impacts of pumping location and duration on the volumetric connectivity with surface-water features and how seasonality may affect this connectivity. Applications of the modeling tool in assessing the impacts of pumping location and duration on surface-water connectivity of existing wells and hyporheic flows are also demonstrated.

Chapter 5 summarized the main conclusions and recommendations of this research.

Chapter 2

Background

2.1 Interaction of groundwater withdrawal wells and surface-water bodies

Groundwater and surface-water are commonly hydraulically connected. Thus, the development and management of groundwater resources should consider how it can affect and be affected by surface-water (Winter et al., 1998; Sophocleous, 2002). From a water quantity and ecology perspective, it is important to consider the hydrological impact of well withdrawals on adjacent surface-water features; while from a water quality perspective, it is important to consider the contamination threat posed to wells from adjacent surface-water features.

2.1.1 Well Withdrawal Impacts on Surface-water

Aquifers are considered to be in a state of dynamic equilibrium under natural conditions. This is shown in Figure 2.1 (a), where the total recharge to the aquifer is equal to the total discharge to the stream. Note, in this case a broad definition is applied to 'stream', where it may also imply a river, pond, lake, or wetland. Now, if a new well with a constant withdrawal rate of Q_1 is drilled at some distance from the stream, it disrupts the predevelopment equilibrium. A cone of depression will be formed around the well and after removing water from storage, the well will begin to intercept some of the water that would otherwise have been discharged to the stream. As a consequence, a local groundwater divide will be induced in between the stream and the well, which is a line separating opposite directions of groundwater flow, and baseflow to the stream will be reduced. This is illustrated in Figure 2.1 (b). The system will then begin to approach a new dynamic equilibrium where recharge to the aquifer will be equal to the sum of

the well withdrawal and the reduced discharge to the stream. If the withdrawal rate is then increased to Q_2, a new equilibrium is achieved as shown in Figure 2.1 (c). In this equilibrium, the boundary of the cone of depression reaches the stream and the groundwater divide disappears. The higher withdrawal rate has to be balanced by inducing recharge, or extracting water, directly from the stream. Thus, the stream shown Figure 2.1 is converted from a gaining stream to a losing stream (Winter et al., 1998; Sophocleous, 2002).

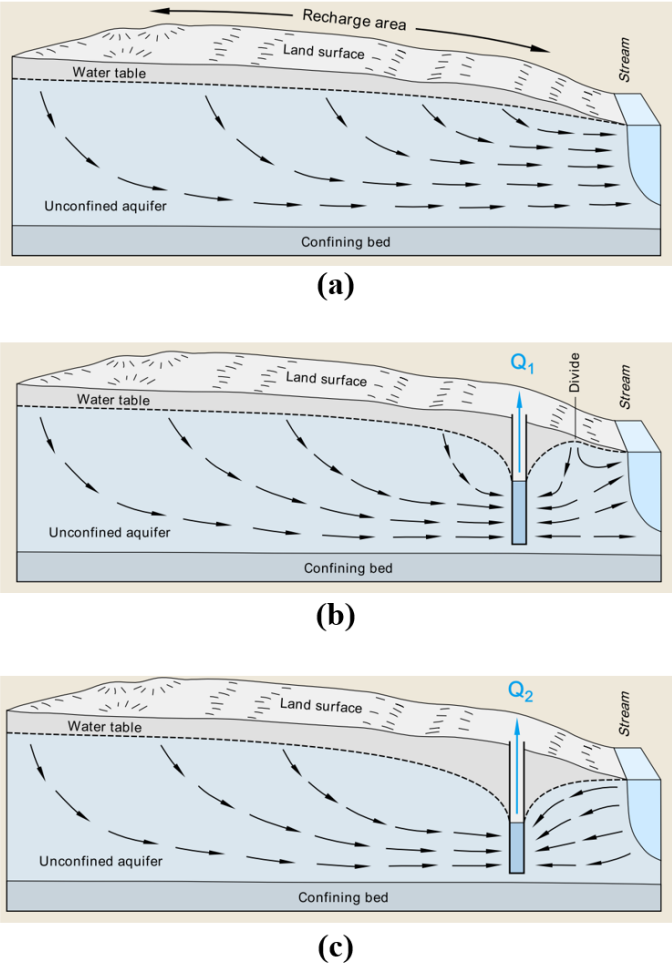

Figure 2.1. Interaction of a groundwater well and a stream: pre-development conditions where recharge to aquifer is equal to discharge to stream (a); a well with a constant withdrawal rate Q_1 is drilled at some distance from the stream and induces a new equilibrium where pumpage is balanced by areal recharge and reduced discharge to the stream (b); the withdrawal rate is increased to Q_2 which induces recharge directly from the stream (c) (modified from Winter et al., 1998).

Note in Figure 2.1, that if the pumping rate is increased further and the areal recharge remains unchanged, then the added withdrawal has to come from depleting the storage and the stream until the pumpage itself is limited by the amount of water available for capture.

2.1.2 Groundwater Under Direct Influence of Surface-water (GUDI)

The fundamental factors that control whether a well is GUDI or non-GUDI are hydraulic connection, the presence of an aquitard that provides a physical barrier to pathogen movement, and finally the travel-time between a surface-water source or area of surface-water recharge and a connected well. In the most extreme case, surface-water runoff will make its way directly to a connected well without having passed through the subsurface. In most cases, the water may simply have a short travel time from the surface-water source to the well (i.e., wells in shallow unconfined aquifers or wells in bedrock with highly connected fracture networks and close to surface-water). As a result, the travel time is too short for all the pathogens to die off and/or undergo filtration by subsurface processes and the water retains surface-water characteristics (Medema et al., 2003; Govt. of Newfoundland and Labrador 2013).

Most provinces in Canada have developed specific protocols and guidelines for the identification of GUDI wells. Alberta, Saskatchewan, and Nova Scotia all have a three-step GUDI assessment scheme. The first step in all three schemes involves rapidly screening for obvious non-GUDI wells based on the well setting (i.e., wells in confined aquifers), proximity to surface-water (i.e., greater than 60 metres from the nearest surface-water body), well construction (i.e., capped and deep watertight casings), and water quality (i.e., no confirmed records of bacterial contamination) (Alberta Environment 2006; Nova Scotia Environment 2002; Saskatchewan Environment 2004). The schemes then require hydrogeological investigations

(i.e., computer modeling, monitoring, and field testing) to be carried out in the next step for wells which fail the initial screening criteria.

The GUDI assessment scheme in Ontario is relatively more stringent in that it does not include an initial screening step. All drinking water supply wells are "flagged" as GUDI if they meet the conditions summarized in Table 2.1, and they are considered GUDI unless a hydrogeological study proves otherwise (Ontario Ministry of Environment 2001).

Table 2.1. Conditions for GUDI well determination under Ontario's Terms of Reference for Hydrogeological Study to Examine Groundwater Sources Potentially Under Direct Influence of Surface-water (2001).

Condition	Summary
i.	Wells regularly contain Total Coliforms and/or periodically contain E. coli; or
ii.	Wells located within approximately 50 days horizontal saturated travel time from surface-water or within 100 meters (for overburden wells) or 500 meters (for bedrock wells) of surface-water (whichever is greater) and meet one or more of the following criteria:
ii. a)	Wells may be drawing water from an unconfined aquifer;
ii. b)	Wells may be drawing water from formations within approximately 15 meters of surface;
ii. c)	Wells are part of an enhanced recharge/infiltration project;
ii. d)	When pumped, adjacent surface-water levels change rapidly or hydraulic gradients next to surface-water increases significantly in a downward direction; and/or,
ii. e)	Chemical water quality parameters (i.e., temperature, conductivity, pH, turbidity) in the well are more consistent with nearby surface-water than local groundwater and/or fluctuate significantly and rapidly in response to climatological or surface-water conditions.

Note, for most of the conditions in Table 2.1, monitoring or field testing is required to determine if they are met. Also, the travel time for condition ii in Table 2.1 requires some level of modeling support. Running GUDI assessment modeling, monitoring and field testing programs for all drinking water wells is likely infeasible and as such water managers could benefit from the use of quality screening tools that would enable them to effectively focus their data collection efforts.

2.2 Groundwater and Solute Transport Modeling

Groundwater modeling can provide useful insight into when and where a particular well may become connected to a surface-water feature before costly monitoring programs are initiated. For planning purposes, it becomes a necessary tool for simulating future conditions to aid in the selection of future well sites.

2.2.1 Overview

The premise of groundwater modeling is the representation of the real system with a governing equation based on the principles of physics that govern groundwater flow. The governing equation for groundwater flow is based on Darcy's Law and conservation of mass.

Darcy's law describes the flow of a fluid through a saturated porous medium and for one-dimensional flow in homogenous isotropic porous media this is given by,

$$q = -K\frac{dh}{dl} \quad \textbf{(Eq. 2.1)}$$

where, q is the Darcy flux or specific discharge [L/T]; K is the hydraulic conductivity of the medium [L/T]; and $\frac{dh}{dl}$ is the hydraulic gradient, or the change in hydraulic head per unit change in length, along the direction of flow [L/L].

Combining the continuity equation and Darcy's Law for an arbitrary control volume of porous media yields the governing equation for three-dimensional transient flow of constant density groundwater in a heterogeneous anisotropic aquifer (Konikow et al., 1996),

$$\frac{\partial}{\partial x_i}\left(K_{ij}\frac{\partial h}{\partial x_i}\right) = S_s\frac{\partial h}{\partial t} + W \quad \textbf{(Eq. 2.2)}$$

where, x_i are the Cartesian coordinates [L], K_{ij} is a second-order tensor for the hydraulic conductivity values along the x, y, and z coordinate axes respectively, which are assumed to be parallel to the major axes of hydraulic conductivity [L/T]; S_s is the specific storage of the porous

media [1/L]; t is time [T]; and W is the volumetric flux per unit volume of aquifer for any source or sink terms [1/T]. For conditions or assumptions where the media is homogenous and isotropic ($K_{xx} = K_{yy} = K_{zz}$), the flow is steady-state ($\partial h/\partial t = 0$) and there are no source or sink terms ($W = 0$), then Eq. 2.2 becomes the three-dimensional Laplace's equation.

To simulate an aquifer system, this governing equation must be solved for the entire aquifer domain after being fed with boundary conditions specifying heads or flows along the boundaries of the model domain, and in the case of a transient problem, initial conditions specifying heads within the model domain at the start of the simulation. The model then solves the governing equation to yield the distribution of head in space, and for transient problems, in time (Anderson et al., 2015).

The concept of solute transport modeling is effectively the same – instead of groundwater it entails simulating the transport of solutes through the subsurface. For purposes of simulating surface-water and well connections, a non-reactive solute can be used, which requires solving the standard advection-dispersion solute transport equation given by (Konikow, 2011),

$$\frac{\partial}{\partial x_i}\left(\varepsilon D_{ij}\frac{\partial C}{\partial x_j}\right) - \frac{\partial}{\partial x_i}(\varepsilon v_i C) - C'W = \frac{\partial(\varepsilon C)}{\partial t} \qquad \textbf{(Eq. 2.3)}$$

where, ε is the effective porosity of the porous medium; D_{ij} is a second order tensor indicating the coefficient of hydrodynamic dispersion [L^2/T]; C is the solute concentration [M/L^3]; v_i is the average linear groundwater velocity in the i^{th} direction given by dividing the Darcy flux in the corresponding direction by the effective porosity, ε; and C' is the solute concentration in the source or sink fluid.

Again, boundary conditions are specified and then the model solves Eq. 2.3 to yield the spatial and temporal distribution of the solute concentration through the model domain.

2.2.2 MODFLOW

MODFLOW is a three-dimensional finite-difference groundwater model developed by the U.S. Geological Survey (USGS). At present, it is the most widely used groundwater model in industry and research settings. It was first released in 1984 and since then the USGS has gone on to release four more versions. The first three, Modular Three-Dimensional Finite-Difference Ground-Water Flow Model (McDonald and Harbaugh, 1984), MODFLOW-88 (McDonald and Harbaugh, 1988), and MODFLOW-96 (Harbaugh and McDonald, 1996), were solely groundwater flow simulation codes. MODFLOW-2000 (Harbaugh et al., 2000) was then developed to incorporate transport and parameter estimation capabilities. The latest version, MODFLOW-2005, made improvements on the management of internal data (Harbaugh, 2005).

The groundwater simulation code in the MODFLOW software packages, known as the Ground-Water Flow (GWF) Process in MODFLOW-2005, numerically solves Eq. 2.2. The method involves first spatially discretizing the model domain into a grid of blocks, or finite-difference cells with nodes at the centre of the cells, as shown in Figure 2.2. This is known as block-centered finite-difference cells. Then a discrete version of Eq. 2.2 is written for each cell in the grid. The left-hand side of this equation accounts for flows from all adjacent cells and flows from features or processes external to the aquifer such as rivers, drains, areal recharge, evapotranspiration or wells, and the right-hand side of the equation is discretized in time using a backward-difference approach. The system of equations are then solved simultaneously using the heads specified for initial conditions to obtain the heads at the cell centres, or nodes, for the first time step. The same is done for the next time step, using the heads obtained for the first time step as the initial heads this time. This is repeated until heads for all the specified time steps are obtained (Harbaugh, 2005).

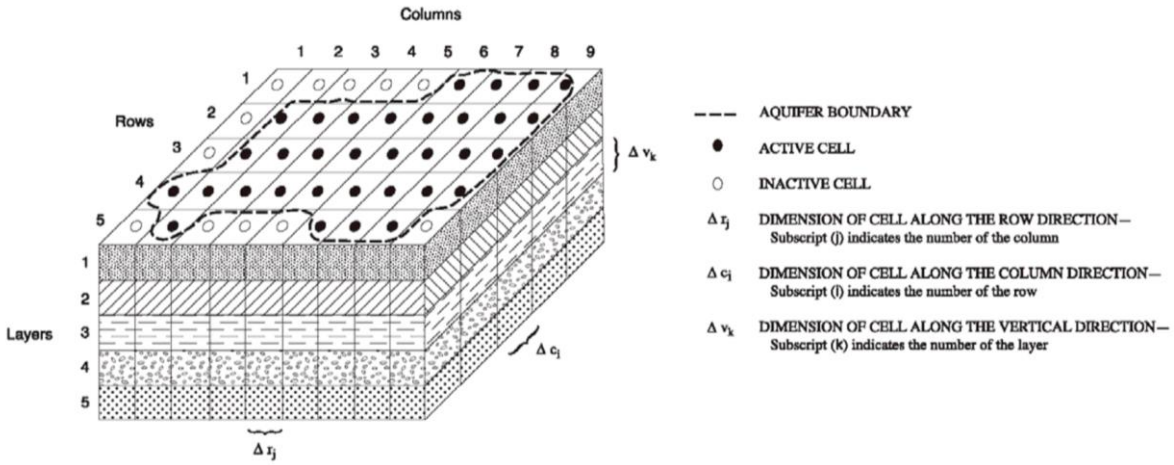

Figure 2.2. Model discretization in MODFLOW-2005 (modified from Harbaugh, 2005).

2.2.3 Particle Tracking

Particle tracking is a technique generally used in the framework of a numerical groundwater flow model. Using the computed head distribution and flows from the groundwater flow model, the movement of imaginary mass-less "particles" are tracked through the model domain (Zheng, 1994). The assumption is that a particle represents a parcel of water and it moves as a discrete volume along a flow path (Anderson et al., 2015). Particles are tracked by computing a particle's velocity at the current location and then multiplying that velocity by a finite time step to obtain its location at the end of that time step. Repeating this process over a number of time steps traces the path of the particle through the flow field over the total elapsed time. Thus, the position of a particle can be obtained as a function of time (Pollock, 1988). If the flow is assumed to be two-dimensional and steady-state with no areal recharge, the particle path lines become streamlines (Anderson et al., 2015). For block-centered finite-difference models, the head distribution is discrete. As such, the velocity field inside each cell has to be interpolated to enable the calculation of a particle's velocity at every point in the flow field (Pollock, 1988).

Particles can be tracked forward or backward in time. In the first case, the particles are typically placed along the water table, recharge areas, and/or inflow boundaries to visualize the

flow of groundwater from these features of interest. In the latter case, the particles are typically placed in discharge locations such as streams or pumping wells and used to determine the source area or capture zone of these features. Particle tracking schemes are also widely used as a component of solute transport models, where they computerize advection or advective transport. Advection refers to transport due to the bulk motion of the fluid and most solute transport problems in the field tend to be advection dominated (Konikow et al., 1996). For solute transport modeling, particles can be tracked forward-in-time from a contamination source area to estimate the propagation of the plume through the model domain or backward-in-time from an area of contamination to estimate the potential source areas (Anderson et al., 2015).

Despite its numerous applications in groundwater modeling, particle tracking is also subject to many errors and thus results obtained from particle tracking schemes need to be interpreted accordingly. The cause of errors may be the build of the groundwater flow model or the particle tracking scheme itself. For example, the number and placement of particles, particularly around areas of converging flow such as pumping wells or gaining streams, affect the delineation of the resulting capture zones (Anderson et al., 2015). The presence of "weak" sinks or sources inside a model cell or model layers with varying vertical cell dimensions may yield erroneous path line and travel time calculations (Zheng, 1994). Note, a "strong" sink induces the flows along all the cell faces to be directed inward, however a "weak" sink is not strong enough and so one or more of the cell face flows may still be directed outwards. Also, particle tracking calculations may not be realistic if the model spatial discretization is too coarse around sinks or source or too coarse to capture important changes in hydraulic conductivity in heterogeneous aquifers. Estimations of effective porosity values also affect particle tracking calculations since they are used to compute cell face velocities (Anderson et al., 2015). These

errors may all impact tracking-based determination of capture zones and connectivity of wells and surface-water.

There are two additional important points to note regarding particle tracking travel time and path line computations. First, due to dispersion and the presence of aquifer heterogeneity, solute arrival times calculated using particle tracking do not represent the time of first arrival but merely when a particular particle reaches a point of interest in the model domain (Anderson et al., 2015). Second, path lines of mass-less particles do not contain any information regarding the volume of water linked to the streamline, i.e., a particle may correspond to a streamtube of negligible flowthrough.

2.3 Determining Connectivity of Groundwater Wells and Surface-Water Bodies

2.3.1 Capture Zone Delineation

The standard method for determining the source of well water through groundwater modeling is capture zone delineation. The capture zone of a well refers to the area in the subsurface and surface from which it sources its water at a given point in time. The boundary of a capture zone represents a line of equal travel time to the well, or an isochrone (Bakker and Strack, 1996). So if a surface-water feature is contained in part or whole inside the capture zone of a well, it provides an estimate of the travel time of groundwater flow between the connected parts of the surface-water feature and the well. Note, the extents of a capture zone for a well depend on both the aquifer hydrogeology and the existing hydrological conditions. Thus, the shape and size of the capture zone may change in response to changes in aquifer recharge, interactions with an adjacent stream and/or pumping operations (Rock and Kupfersberger, 2002).

Hantush (1965), Hunt (1999), Anderson (2000), Bakker and Anderson (2003), Hantush , (2005), Rushton (2007), Intaraprasong and Zhan (2009), Asadi-Aghbolaghi et al. (2013), and numerous others have developed analytical solutions for examining well and surface-water connections. These analytical methods typically require invoking several simplifying assumptions such as, steady-state flow, two-dimensional flow, single aquifer system, homogeneity, isotropy, aquifer of infinite extents, fully penetrating wells, and/or a constant pumping rate amongst others (Todd, 1980; Grubb, 1993; Bakker and Strack, 1996). While capture zones delineated analytically provide acute insights into how hydrogeological and pumping parameters can affect well and surface-water connections, they may be inaccurate in estimating the true connections under field conditions as a result of the simplifying assumptions. For example, the assumption of steady-state or uniform flow may prove adequate in the case of a single well but less so for well fields when the flow field is ambient due to well interference. Similarly, assumptions of two-dimensional flow may be valid in the short-term when aquifer recharge is negligible, but not in the long-term or in close vicinity of the well (Ceric and Haitjema, 2005; Grubb, 1993; Rock and Kupfersberger, 2002). Lastly, assumptions of homogeneity and isotropy are often not representative of real aquifers.

Most real world problems warrant the use of numerical methods for determining well and surface-water connections through capture zone delineation. The most common approach at present is to establish the steady-state flow field using a groundwater flow model and then use backward-in-time advective particle tracking to delineate the capture zone. In this approach, time-dependent capture zones can be established by tracking particles over different time intervals and ultimate capture zones can be established by tracking the particles until they exit to the ground surface (Frind et al., 2002). If these capture zones intersect with a surface-water

boundary, then the travel time of groundwater flow between the surface-water boundary and the well can be inferred. One important limitation of using advective particle tracking, in addition to those inherent with particle tracking schemes, is that individual particles do not delineate capture zones with continuous boundaries and to do so would require an unfeasibly large number of particles (Frind et al., 2002). More importantly, the use of mass-less particles only show which points are hydraulically connected but cannot provide any information about the potential concentration of surface-water contaminants that may be seen at a well (i.e., it is difficult to ascertain the degree of connection between wells and surface-water features).

In this regard, solute transport modeling approaches may be employed to establish the degree of groundwater and surface-water connections (Winter et al., 1998; Keefe, 2004; Stauffer and Stone, 2005). Solute transport modeling requires first solving the groundwater flow equation, shown in Eq. 2.2, to establish the head distribution and the resulting velocity field distribution. Then, the standard advection-dispersion solute transport equation, shown in Eq. 2.3, may be solved with boundary conditions where a conservative tracer is released from a surface-water boundary. This simulates the transport of the tracer through the model domain and the concentration of the tracer in the well indicates the strength of the connection with the surface-water boundary it was released from. Not only is solute transport modeling more computationally expensive, but also accurately solving the solute transport equation using numerical methods is generally more difficult than the groundwater flow equation owing to the difficulties in characterizing which transport mechanisms (i.e., advection or dispersion) are dominant in a system spatially and temporally (Konikow et al., 1996).

2.3.2 Capture-Fraction Mapping (the LRD Method)

Leake et al. (2010) developed a method to spatially map the hydrological impacts of pumping on surface-water features, referred to here as the LRD method. The premise of the method was articulated in the classic paper by Theis (1940) – "all water discharged by wells is balanced by a loss of water somewhere". The "loss of water" can come from either the storage in the aquifer itself or 'capture'. 'Capture' is defined as "any withdrawal induced changes in inflow to or outflow from an aquifer" (Leake et al., 2010). This may be reducing the baseflow to a stream and/or inducing recharge from the stream as shown in Figure 2.1. Capture can also come from reduced evapotranspiration due to a lowering of the water table and/or increased infiltration in areas where it was previously precluded due to high water tables (Leake et al., 2010). Thus, the withdrawal rate at the well, Q, can be expressed as,

$$Q = D + \sum_{i=1}^{n} C_i = D + C \qquad \textbf{(Eq. 2.4)}$$

where, D is the rate of depletion of the aquifer storage, or the depletion rate, $\sum_{i=1}^{n} C_i$ represents the sum of the capture rates from all possible sources, or the total capture rate, C.

Using Eq. 2.4, the depletion rate and capture rate can then be expressed as the following dimensionless fractions,

$$depletion\ fraction = D/Q \qquad \textbf{(Eq. 2.5)}$$

$$capture\ fraction = C/Q \qquad \textbf{(Eq. 2.6)}$$

The method entails first running a groundwater flow model simulation without any pumping and establishing the capture from features with specified-head (Dirichlet) or head-dependent (Cauchy) boundary conditions. These may include recharge from stream to the aquifer, discharge from aquifer to the stream, areal recharge, evapotranspiration, etc., and

represent the baseline capture. Next, a well is added in a single model cell and the simulation is re-run. The capture for the well can then be calculated as the difference between all the capture components from the base case run and the run with the well. Once the capture is calculated, it is converted to the dimensionless capture-fraction as shown in Eq. 2.6. This is repeated (i.e., a well with the same pumping parameters is added in another model cell and the capture for a well in that location is calculated) until the desired resolution is reached. Then, a contour map can be generated where each point indicates the fraction of pumping rate that would be supplied from capture if a well pumping at the specified rate were to be placed there (Leake et al., 2010).

Figure 2.3 shows a contour map indicating the fraction of pumping that is supplied from capture for a selected river segment after 5 years in Michigan, U.S.

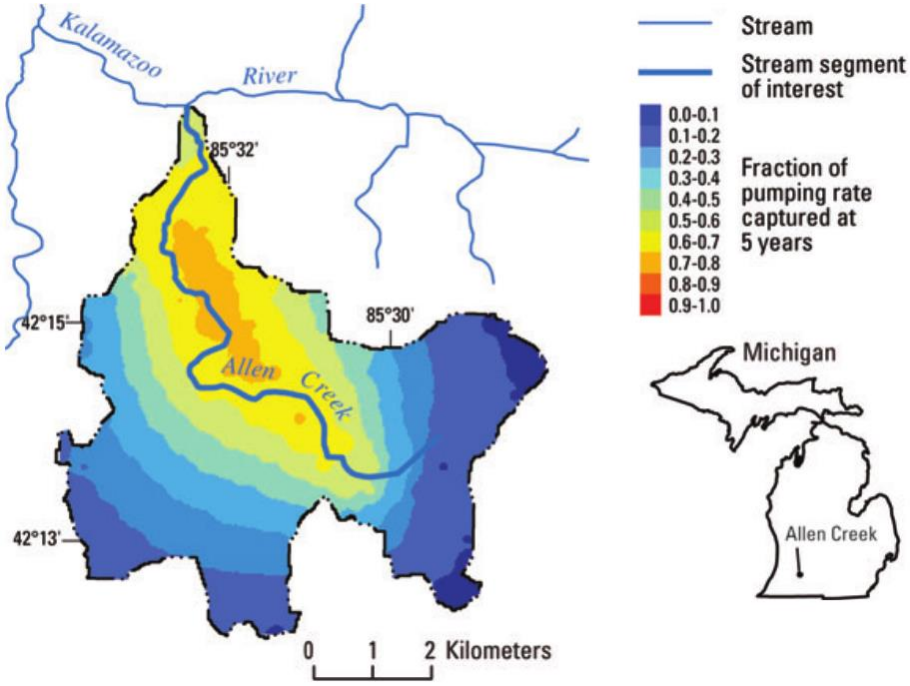

Figure 2.3. An example capture-fraction map; the map shows the fraction of pumping supplied from capture after 5 years for a selected river segment in Michigan, U.S. (modified from Leake et al., 2010).

Using this method, valuable insights can be gained into the sustainability of pumping operations. However, note that since the definition of capture includes any changes in flows to

and out of the aquifer as a result of pumping, it does not exclusively show the impact on the stream, which is a factor of only two components of capture: (1) reduced baseflow to the stream from the aquifer and, (2) increased recharge from the stream to the aquifer. For cases where these two components do not dominate the other withdrawal induced changes, then simply removing the other components from the calculation of capture will yield the capture only from the stream (i.e., stream-specific capture), and for cases where the stream-flow components are the most dominant, the other components need not be removed as the stream-specific capture-fraction map and the 'total' capture-fraction map would effectively be the same. Note, it is possible for a well to hydrologically impact a surface-water feature but not be GUDI (i.e., a well within the high capture areas shown in Figure 2.3 may not necessarily be GUDI), and hence this mapping approach is inadequate for examining the hydraulic connections between wells and surface-water features as needed here.

2.3.3 Flow-Based Capture Delineation

Flow-based capture delineation methods have the potential to combine the functions of capture zone delineation methods, which show the contamination threat posed to wells, and LRD method (Leake et al., 2010), which shows hydrological impacts of pumping. Flow-based capture delineation methods can delineate capture zones volumetrically without the use of particle tracking or solute transport modeling. The basic output of these methods is the estimation of the volume of water that each model cell contributes to a specified sink or source. For a well, this is effectively the volume of water that it has sourced from each model cell. When these cells are all stream cells, a direct estimate of the volume of well water that is originating from the stream can be obtained. This simultaneously serves as an indicator of (1) the contamination threat posed to

the well from surface-water sources and, since the amount of water that is being removed from the stream is known, (2) the hydrological impact of pumping on the stream.

At present, there are two flow-based capture delineation tools to the knowledge of the author, MODALL (Potter et al., 2008) and FlowSource (Black and Foley, 2013). MODALL uses cell-by-cell flows obtained from steady-state MODFLOW (Harbaugh et al., 2000) simulations to compute the flow balance in each groundwater model cell and determine the fraction of flow, termed 'capture-fraction' or CF, in each cell that originates from a given source(s) or reaches a given sink(s). The cell-by-cell CF calculations are then used to generate CF isopleths that delineate capture areas based on their fractional contribution to the withdrawal rate at the well (Potter et al., 2008). FlowSource can provide the same outputs as MODALL, but employs a topology storage method, is much faster, and has additional capabilities. It is described in more detail in Section 2.4.

2.4 FlowSource

FlowSource (Black and Foley, 2013) is a MODFLOW-based (Harbaugh et al., 2000) software tool that can volumetrically delineate steady-state and quasi-steady-state capture zones. MODALL (Potter et al., 2008) however, can only be used to delineate steady-state capture zones. FlowSource takes MODFLOW drawdown, discretization and cell-by-cell files as inputs and then uses directed acyclic graphs (DAGs) to represent the groundwater flow path information. This enables it to estimate the volume of water that ultimately reaches a predefined 'destination' from each groundwater model cell. The 'destination' can be a single cell or a group of cells and the cells need not be adjacent to one another. From determining the volumetric contribution of each model cell to the destination cell(s), FlowSource is able to calculate a range of different metrics. These include, the volume of water passing through or originating in a cell that is ultimately

captured in the destination cells(s), called ‘volume-through’ and ‘volume-from’ respectively; fractional equivalents of both, called ‘fraction-from’ and ‘fraction-through’ respectively; and statistical summaries and probabilistic outputs of the volumetric capture data. The MODALL outputs are equivalent to the fraction-through output in FlowSource.

2.4.1 FlowSource Method

To illustrate the method of calculation in FlowSource, consider the hypothetical cell-by-cell flows from a groundwater model shown in Figure 2.4.

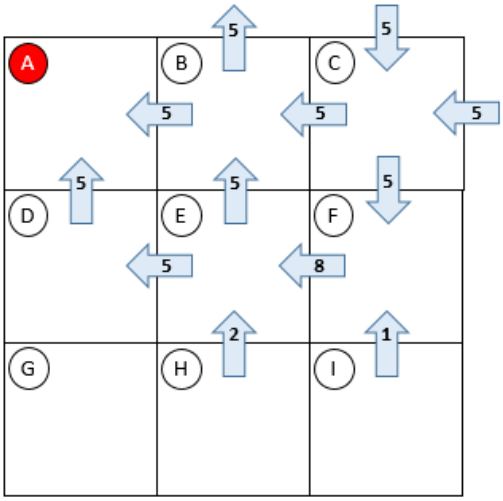

Figure 2.4. Cell-by-cell flows from a hypothetical groundwater flow model; the arrows represent the volume of flow across each cell face; cell A is a sink and the ‘destination cell’ (modified from Foley and Black, 2013).

In Figure 2.4, each cell is identified with a letter (A through I) and the arrows represent the volume of flow across each cell face (i.e., there are 5 units of water flowing from cell B to cell A across the cell face shared by the two cells). Note, Cell A is a sink and defined as the destination cell in this case.

Figure 2.5 now shows the same flow distribution as a directed graph. In a directed graph structure, each cell is represented as a node and the flows across the cell faces are represented as edges. Note that it was necessary to create dummy nodes for cells B and C to represent flows to

and from outside the model grid and also for cells F, H and I to conserve mass balance in those cells (Foley and Black, 2013).

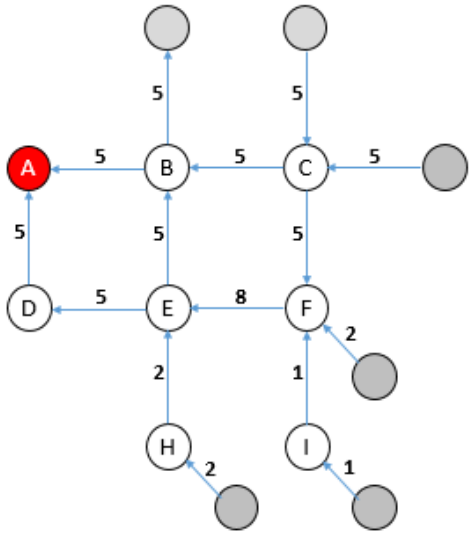

Figure 2.5. Directed graph representation of cell-by-cell flows from the example in Figure 2.4 (modified from Foley and Black, 2013).

Using a directed graph allows the groundwater flow path information to be represented in terms of the actual topology of the flow field. Thus, the cells can be sorted in the order of downstream flow as shown in Figure 2.6, instead of the row and column order shown in Figure 2.4 (Foley and Black, 2013).

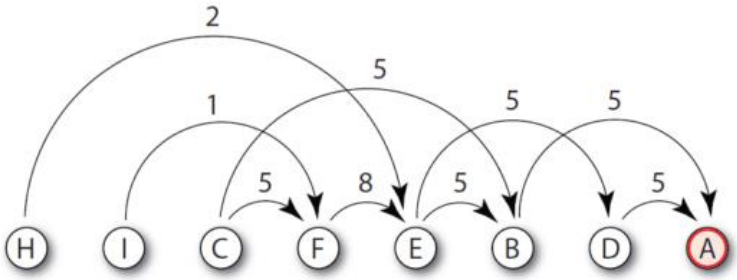

Figure 2.6. Nodes from directed graph sorted topographically in order of downstream flow (Figure from Foley and Black, 2013).

It is now possible to look at each cell and calculate its volumetric contribution to the destination cell (cell A) by simply using arithmetic operations. FlowSource starts with the most

downstream cell and sequentially move upstream. For example, cell A is the most downstream cell and has 10 units of water flowing in. Since it is the destination cell, all the water entering cell A is extracted. Thus, cell A has a volume-through of 10 units and a fraction through of 100%. As none of the water that is extracted in cell A originated in cell A, it has a volume-from and fraction-from of 0 and 0% respectively. Next, cell D has 5 units of water flowing in and 5 units of water flowing out to cell to A, where all of it is extracted. Thus, cell D has a volume-through of 5 units and a fraction through of 100%. Again, since none of the water that is extracted in cell A originated in cell D, it too has a volume-from and fraction-from of 0 and 0% respectively. Similar calculations can be made for all the remaining cells, sequentially going upstream. Figure 2.7 shows a schematic of the calculated metrics.

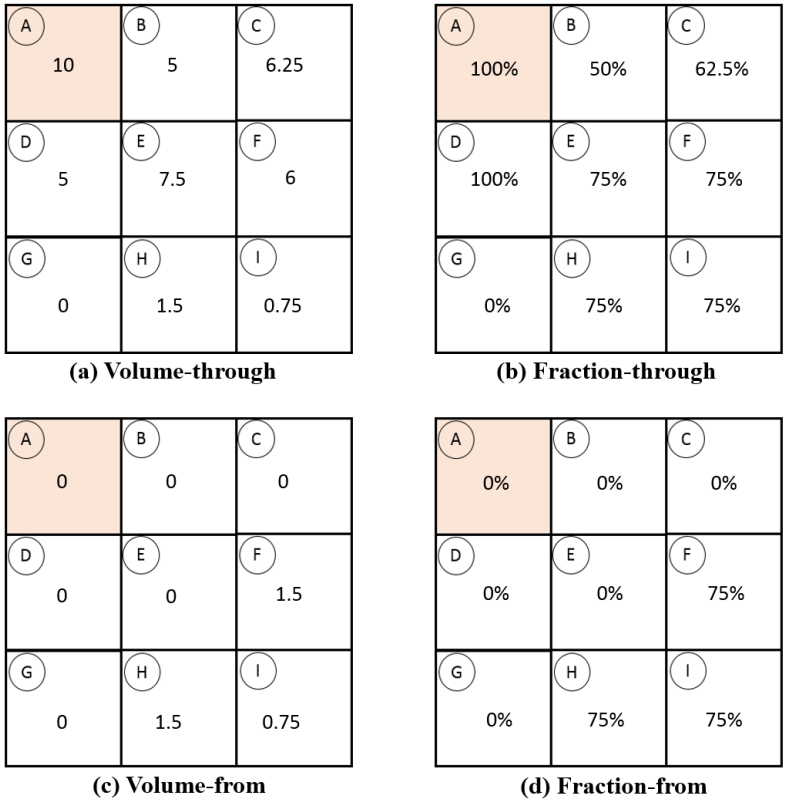

Figure 2.7. Calculated FlowSource metrics for the cell-by-cell flows from the example in Figure 2.4 (modified from Foley and Black, 2013).

All the metrics in Figure 2.7 were determined in a single traversal of the topologically sorted nodes. This is because there were no cycles along the nodes. To demonstrate the problem associated with cycles, consider again the same model but with the horizontal edge between nodes B and C reversed as shown in Figure 2.8.

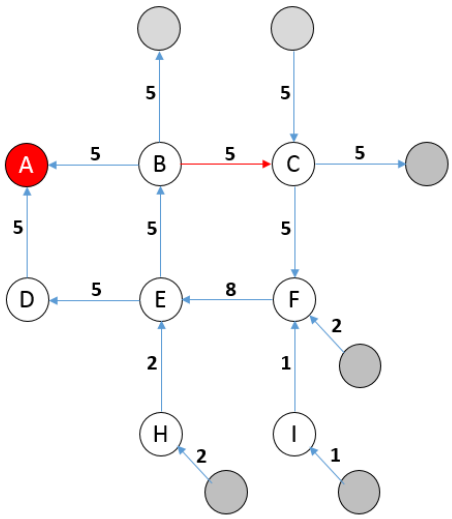

Figure 2.8. Directed graph with horizontal edge between nodes B and C reversed (modified from Foley and Black, 2013).

The new cell flow topology associated with the directed graph in Figure 2.8 is shown in Figure 2.9. Note the presence of a cycle between cell B and cell C.

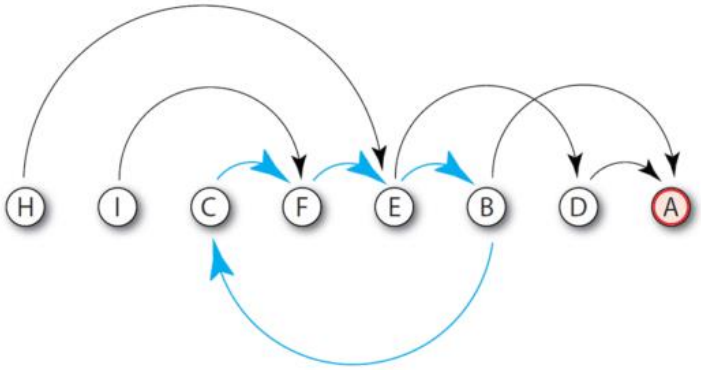

Figure 2.9. New topological sorting of nodes in order of downstream flow (Figure from Foley and Black, 2013).

Now it is not possible to complete the calculations because cell B would require cell C to be processed first, while cell C would require cell B to be process first. The solution to the

groundwater flow equation would not actually permit this scenario since it is physically impossible. The only time cyclical paths are introduced are due to numerical errors in the groundwater mass balance. These flows are typically very small in converged MODFLOW simulations. To avoid this, the FlowSource method first checks for the presence of cycles in the graph before doing the calculations. If a cycle is found, then the edge with the lowest volume in the cycle is removed from the graph. This is repeated until the graph is acyclic (Foley and Black, 2013).

In summary, FlowSource first converts the MODFLOW cell-by-cell flows into a directed graph. It then proceeds to check for cycles in the graph and eliminates them if they exist. The nodes are then sorted topologically according to the flow field and finally the FlowSource metrics are calculated for each cell, starting with the most downstream and finishing with the most upstream. For transient models, the volumetric metrics are calculated at each time-step as time-instant steady-state cases. FlowSource can then output the cell-by-cell minimum, maximum, and mean values from the entire simulation. Additionally, it can compute probabilities within range and always/sometimes/never values for each cell by looking at the number of times a cell becomes hydraulically connected to the destination cell(s) (Foley and Black, 2013).

For a transient model with an estimated 4,000,000 active nodes and 150,000 destination cells, or locations of interest, the program run time on a computer with a basic processor is approximately 30 seconds for each stress period (Foley and Black, 2013).

2.4.2 Current and Future Applications

FlowSource has been widely used in the U.K. by industry, consultants, and regulators for a variety of purposes such as well head protection, pump and treat optimization and transient

capture zone analysis (Black and Foley, 2013). For example, Figure 2.10 shows the ability of FlowSource to demonstrate how well capture zones change in response to competing abstraction pressures.

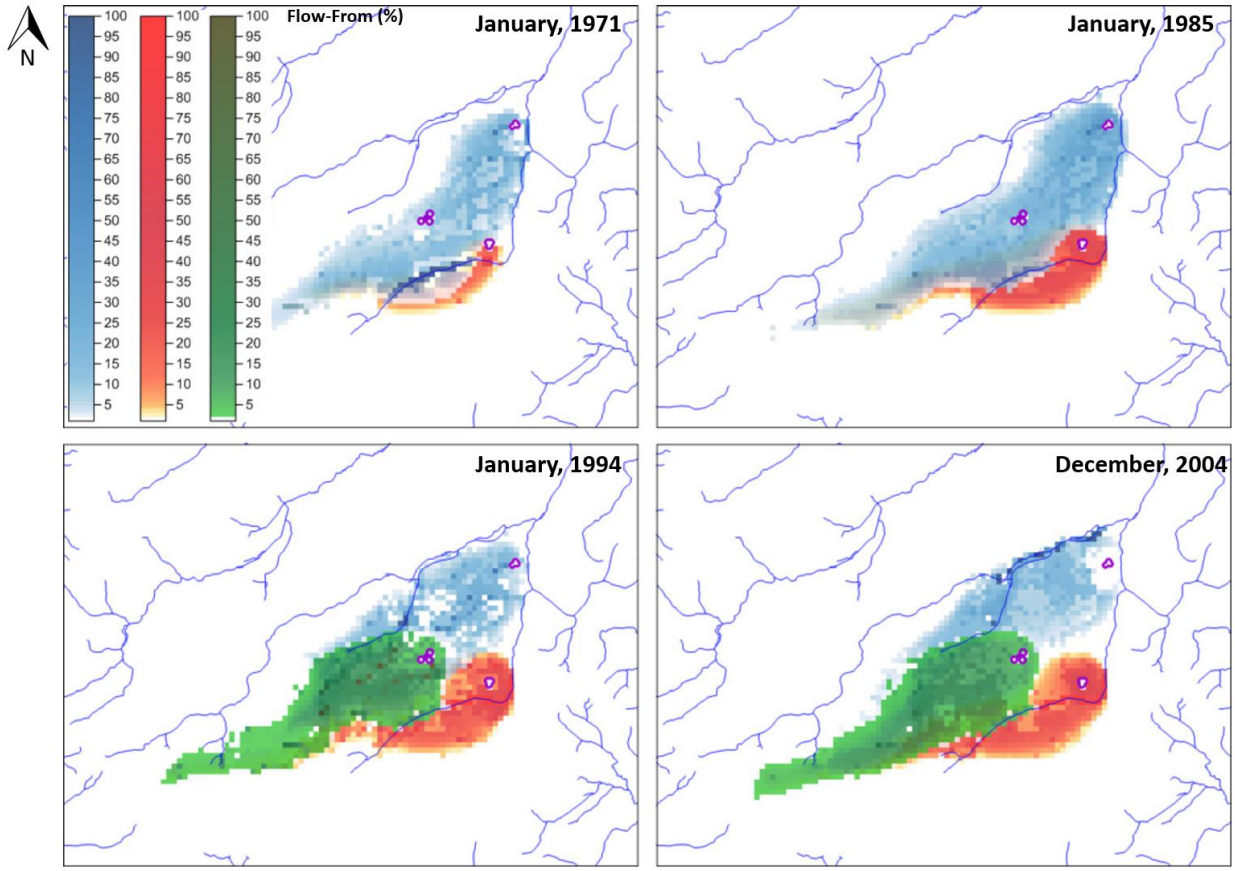

Figure 2.10. Impact of competing abstraction pressures on well capture zones; FlowSource flow-from metric shown for three different well fields from January 1971 to December 2004 (modified from Black and Foley, 2013)

In Figure 2.10, the initial capture zone of the blue well field is shown to include the southern water course. However, with the development of additional abstractions to the south, the capture zone of the blue well field gradually drifts northward until it eventually includes the previously unaffected northern watercourse (Foley and Black, 2013).

The abilities to determine the volume of water passing through or originating in each model cell that is ultimately captured by a well for both steady-state and transient (which are

treated as quasi-steady-state) models and process multiple source or sink cells simultaneously makes FlowSource particularly useful for assessing well and surface-water connections

2.4.3 Sources of Errors

As a result of using cell-by-cell flows from a finite-difference model like MODFLOW, FlowSource calculations are sensitive to grid size. This is because the cell-by-cell flows are represented as orthogonal flows at the cell faces. This implicitly assumes that the flows in the cell are fully mixed, whereby all inflows to a cell are assumed to be evenly distributed to the output faces. Though this does not manifest any major problems with fine grids, coarse grids may show significant numerical dispersion. This is because the fully mixed assumption fails to account for the streamtubes that develop inside the cells. Thus, periphery cells that do not have any advective flow lines flowing into the destination cell may still be included in the calculations. As such, a solution is warranted that can accurately determine the connections between the cell faces without being too computationally expensive.

Chapter 3

Methodology

3.1 Reducing Numerical Dispersion in FlowSource

To address the numerical dispersion issues in FlowSource (Black and Foley, 2013), a method was developed to evaluate the volumetric flow connections within a three-dimensional rectilinear finite-difference cell by either applying mass balance or by analytically recreating the streamtube geometry within the cell. This method has been embedded in an algorithm that can be incorporated into FlowSource. The algorithm takes flows at the cell faces as inputs, which are obtained from running a groundwater flow model such as MODFLOW (Harbaugh et al., 2000) and outputs the volumetric flows from each inflow face to each outflow face.

The method is based on Pollock's semi-analytical particle tracking method (Pollock, 1988). Thus, the underlying assumptions in Pollock's method are carried over. These include: (1) the flow field is steady-state, (2) orthogonal cell face flows, and (2) the principal components of the groundwater velocity vector vary linearly within the cell with respect to their own coordinate direction (i.e., linear interpolation of the groundwater velocity vector). It should also be noted in assuming orthogonal cell face flows, Pollock's method also implicitly assumes that the cell face flow velocity is evenly distributed over the entire area of the cell face. The method developed for thesis also has some assumptions of its own. These include: (1) no addition or removal of water inside the cell and, (2) that the principal components of the velocity gradients within the cell are non-zero.

The algorithm has been developed in MATLAB and will be translated into VisualBasic.NET for incorporation into FlowSource.

3.2 Pollock's Method

Pollock (1988) developed a semi-analytical particle tracking method for block-centered finite-difference groundwater flow models. The method generates particle path lines using conservation of mass inside the cell and will here be extended to generate three-dimensional streamtube surfaces for the purposes of this thesis.

Figure 3.1 shows the how the finite-difference cells are orientated and how the cell face flows are defined for the method.

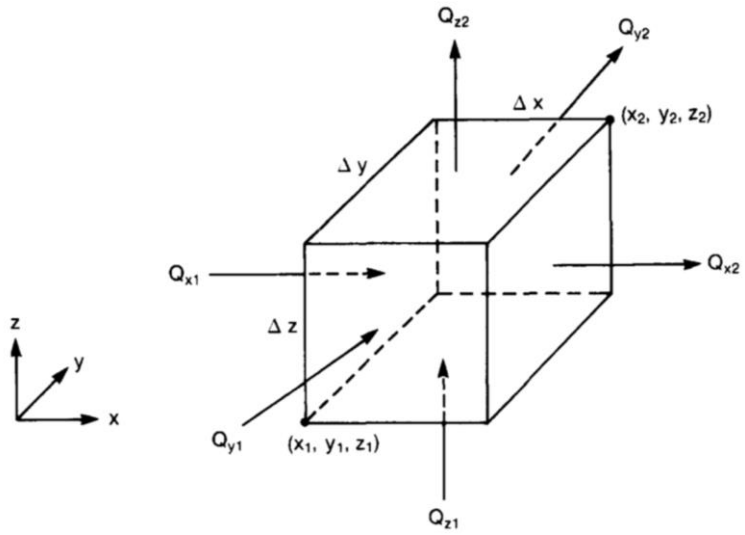

Figure 3.1. Orientation of finite-difference cell and definition of cell face flows (Figure from Pollock, 1988).

The six cell faces are defined as x_1, x_2, y_1, y_2, z_1, and z_2. Cell face x_1 lies along $x = x_1$, and cell face x_2 lies along $x = x_2$. Analogous definitions hold for the remaining four cell faces.

Pollock's method assumes a steady-state flow field and that the principal components of the groundwater velocity vector vary linearly within the cell with respect to their own coordinate direction. Thus, in each of the three principal directions, the velocity gradients, A_x, A_y, and A_z are constant and can be expressed as:

$$A_x = \frac{(v_{x2} - v_{x1})}{\Delta x} \quad \textbf{(Eq. 3.1)}$$

$$A_y = \frac{(v_{y2} - v_{y1})}{\Delta y} \quad \textbf{(Eq. 3.2)}$$

$$A_z = \frac{(v_{z2} - v_{z1})}{\Delta z} \quad \textbf{(Eq. 3.3)}$$

where, v_{x1}, v_{x2}, v_{y1}, v_{y2}, v_{z1}, and v_{z2} are the cell face velocities and Δx, Δy, and Δz are the dimensions of the cell along each of the coordinate axes.

It follows then, that the principal velocity components within a cell are given by:

$$v_x = A_x(x - x_1) + v_{x1} \quad \textbf{(Eq. 3.4)}$$

$$v_y = A_y(y - y_1) + v_{y1} \quad \textbf{(Eq. 3.5)}$$

$$v_z = A_z(z - z_1) + v_{z1} \quad \textbf{(Eq. 3.6)}$$

where, v_x, v_y, and v_z represent the velocity functions in each of the coordinate directions inside the cell.

The velocity component functions of the particle are then expressed as:

$$\left(\frac{dv_x}{dt}\right)_p = A_x v_{xp} \quad \textbf{(Eq. 3.7)}$$

$$\left(\frac{dv_y}{dt}\right)_p = A_y v_{yp} \quad \textbf{(Eq. 3.8)}$$

$$\left(\frac{dv_z}{dt}\right)_p = A_z v_{zp} \quad \textbf{(Eq. 3.9)}$$

where, $(dv_x/dt)_p$, $(dv_y/dt)_p$, and $(dv_z/dt)_p$ represent the velocity component functions of the particle in each of the coordinate directions and v_{xp}, v_{yp}, and v_{zp} represent the rate of change of the particles position in each of the coordinate directions.

Eq. 3.7 to Eq. 3.9 can then be directly integrated and combined with Eq. 3.4 to Eq. 3.6 to yield analytical expressions for the particle path line segments within each cell. These expressions are shown below:

$$x_p(t_2) = x_1 + \left(\frac{1}{A_x}\right)[v_{xp}(t_1)\exp(A_x\Delta t) - v_{x1}] \quad \textbf{(Eq. 3.10)}$$

$$y_p(t_2) = y_1 + \left(\frac{1}{A_y}\right)[v_{yp}(t_1)\exp(A_y\Delta t) - v_{y1}] \quad \textbf{(Eq. 3.11)}$$

$$z_p(t_2) = z_1 + \left(\frac{1}{A_z}\right)[v_{zp}(t_1)\exp(A_z\Delta t) - v_{z1}] \quad \textbf{(Eq. 3.12)}$$

where, $v_{xp}(t_1)$, $v_{yp}(t_1)$, and $v_{zp}(t_1)$ are the principal components of the particle velocity in the current time step, t_1; $x_p(t_2)$, $y_p(t_2)$, and $z_p(t_2)$ indicate the location of the particle within the three-dimensional cell at some future time step, t_2; and Δt is the elapsed time between t_1 and t_2.

Eq. 3.10 to Eq. 3.12 can then be used to directly evaluate the exit location of the particle (x_e, y_e, z_e), using $\Delta t = \Delta t_e$, where Δt_e is the time it takes the particle to exit the cell. Note, the particle can exit through any of the outflow faces. The cell face a particle actually exits through

will correspond to the direction of its shortest travel time (i.e., if the particle exits through cell face y_1 or y_2, then its shortest travel time is in the y-direction). The time required for a particle to reach a given cell face can be calculated as:

$$\Delta t_x = \frac{1}{A_x} \ln\left(\frac{v_{xp}(t_2)}{v_{xp}(t_1)}\right) \quad \textbf{(Eq. 3.13)}$$

$$\Delta t_y = \frac{1}{A_y} \ln\left(\frac{v_{yp}(t_2)}{v_{yp}(t_1)}\right) \quad \textbf{(Eq. 3.14)}$$

$$\Delta t_z = \frac{1}{A_z} \ln\left(\frac{v_{zp}(t_2)}{v_{zp}(t_1)}\right) \quad \textbf{(Eq. 3.15)}$$

where, Δt_x, Δt_y, and Δt_z represent the time required for a particle to exit the cell in each of the coordinate directions.

Thus, if cell face y_2 is the actual exit face, then Δt_e will be equal to Δt_{y2}, given by,

$$\Delta t_{y2} = \frac{1}{A_y} \ln\left(\frac{v_{y2}}{v_{yp}(t_1)}\right) \quad \textbf{(Eq. 3.16)}$$

Note, in Eq. 3.16 it was assumed that the *y*-component of the velocity gradient, A_y, is non-zero. However, if it turns out that A_y is zero, then Eq. 3.16 will be indeterminant. In this special case, the exit time in a particular direction is simply calculated as the distance travelled by the particle in that direction divided by the velocity component in that direction. Thus, if the velocity gradient was zero in the *y*-direction, Eq. 3.16 would be replaced by,

$$\Delta t_{y2} = \frac{(y_2 - y_p(t_1))}{v_{y1}} \quad \textbf{(Eq. 3.17)}$$

where, $y_p(t_1)$ is the y-coordinate of the starting location of the particle.

Figure 3.2 shows a schematic from the original paper by Pollock (1988) of a particle, *p*, being tracked through a two-dimensional cell. The particle is released from cell face x_1 and exits through cell face y_2.

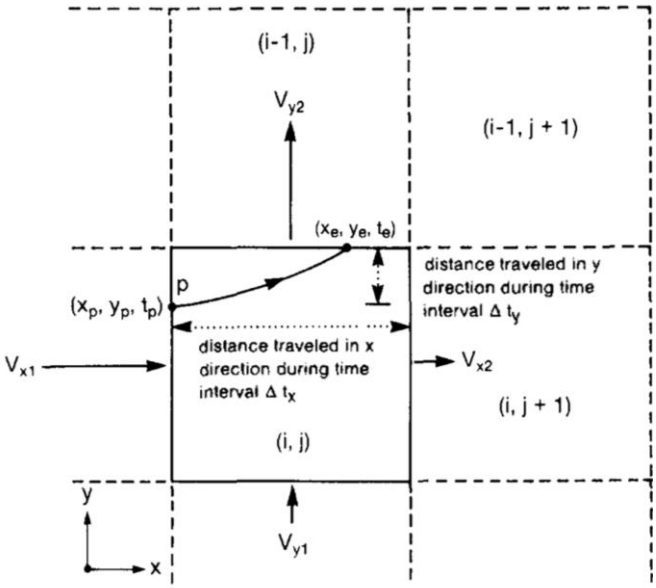

Figure 3.2 A particle being tracked through a two-dimensional cell from (x_p, y_p) at time t_p to its exit (x_e, y_e) at time t_e (Figure from Pollock, 1988).

3.3 Computing Flow Connections in a Two-Dimensional Rectilinear Cell (2D-Algorithm)

For a two-dimensional rectilinear finite-difference cell, the streamtube geometry need not be fully recreated to determine volumetric flows from the inflow faces to the outflow faces. Assuming there are no internal sources or sinks inside the cell that add or remove water and a steady-state flow field, then conservation of mass in the cell requires that the total inflows equal the total outflows. Using this simple mass balance approach, the volumetric flow connections in a two-dimensional cell can be evaluated solely in terms of the cell face flows. This obviates the need for numerical or analytical particle tracking, greatly reducing computation time. In addition, because all calculations are exclusively in terms of the cell face flows, the effectiveness of this method is not sensitive to the model grid size.

Figure 3.3 illustrates how the cell face flows may be defined for a two-dimensional rectilinear finite-difference model cell. Cell faces x_1 and x_2 lie perpendicular to the x-axis at $x = x_1$ and $x = x_2$ respectively, while cell faces y_1 and y_2 lie perpendicular to the y-axis at $y = y_2$ and $y = y_2$ respectively.

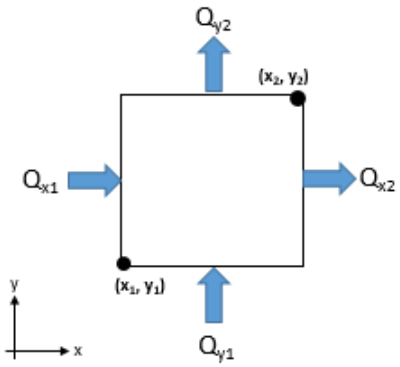

Figure 3.3. Orientation of a two-dimensional finite-difference cell and definition of cell face flows.

Thus, all volumetric flow connections can be expressed as $Q_{i,j}$, where *i* is index of the cell face from which the flow originates and *j* is the index of the cell face at which the flow exits (i.e., the flow from cell face x_1 to cell face y_2 would be expressed as $Q_{x1,y2}$). The four corners of the cell can also be now defined using this indexing routine, whereby corner *i,j* refers to the corner between cell face *i* and cell face *j*.

In a two-dimensional rectilinear cell with orthogonal flows at each cell face, each cell face can either be (1) an inflow boundary, (2) an outflow boundary, or (3) a no-flow boundary. Thus, there are 3^4 or 81 possible permutations of flow boundaries that can arise. Careful observation reveals that the 81 cases can effectively be reduced to three general sets of cases: (1) trivial cases, (2) two inflows-two outflows and (3) all other cases. The discussions following will explain the development of the set of equations used to calculate volumetric flow connections for each of the three general cases.

3.3.1 Trivial Cases

Cases where none of the cell faces are hydraulically connected are defined as trivial, since for these cases, volumetric flow connections need not be calculated. Trivial cases include all cases where all cell face flows are directed inwards (i.e., a "strong" sink), or where all cell faces are directed outwards (i.e., a "strong" source), or when there are no flows inside the cell. Examples of some trivial cases are shown in Figure 3.4.

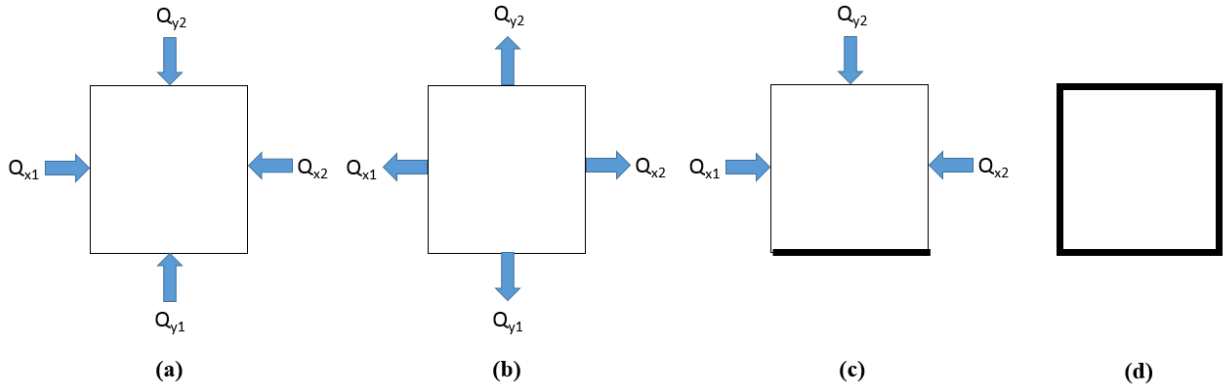

Figure 3.4. Schematics of some trivial cases: strong sink (a), strong source (b), strong sink with a no-flow boundary at cell face y1 (c), all no-flow boundaries (d).

Note, the assumption of no internal removal or addition of water inside the cell is not affected by encountering strong sinks or sources inside the cell. This is because even though all the water that enters a cell is removed inside the cell in the presence of a strong sink, since all the cell faces are inflow faces, no calculations need to be made for the amount of flow transferred from each inflow face to each outflow face. Similarly, even though water is added when there is strong source inside the cell, since none of the cell faces are hydraulically connected no calculations need to be made.

3.3.2 Two Inflows-Two Outflows

Two inflows-two outflows is a flow boundary combination comprising of six different permutations. It turns out that four of the six permutations are just rotations of one flow regime,

while the remaining two permutations are rotations of another flow regime. Thus, the flow boundary combination of two inflows-two outflows can yield two general types of flow regimes, Type 1 and Type 2. Type 1 has two rotations and Type 2 has four. This is illustrated in Figure 3.5. For the Type 2 cases, shown in Figure 3.5 (e) to (f), the inflow corner (i.e., corner shared by two inflow edges) was forward tracked and the outflow corner (i.e., corner shared by two outflow edges) was backward tracked using Pollock's method (Pollock, 1988) to recreate the dividing streamtubes inside each cell for visualization.

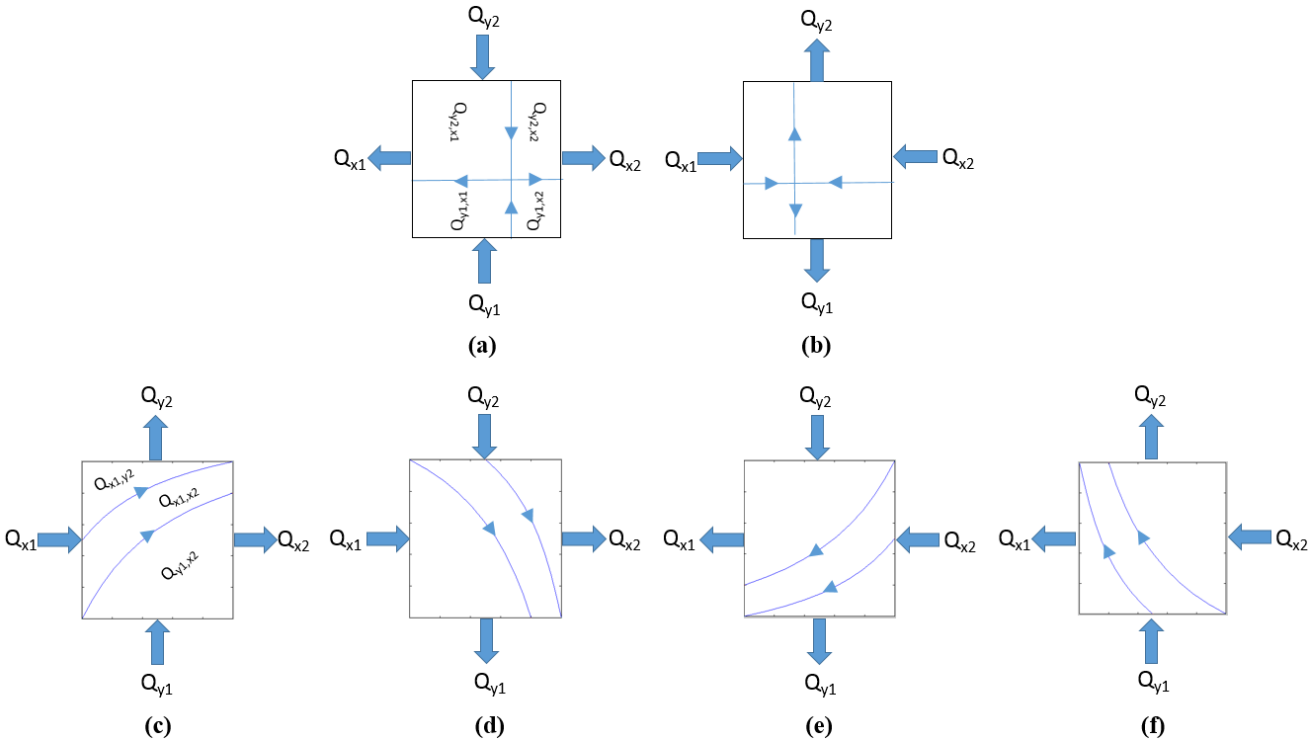

Figure 3.5. Schematics of the two general flow regime types of two inflows-two outflows: (a) and (b) show the two rotations of Type 1, Case 1A and Case 1B; while (c), (d), (e) and (f) are the four rotations of Type 2, Cases 2A, 2B, 2C and 2D. The streamtubes are annotated for Case 1A, in (a), and Case 2A, in (c).

The issue with the fully mixed assumption can be visualized through the schematics shown in Figure 3.5. For example, note in Figure 3.5 (a) that there is no flow from cell face y_1 to cell face y_2. However if the cell is assumed to be fully mixed, then the flows from both cell faces y_1 and x_1 are being assumed to be evenly distributed to cell faces y_2 and x_2.

Type 1 flow regimes have a stagnation point inside the cell since the two outflows are in opposite directions and the two inflows are in opposite directions. The volumetric flow connections for these cases can be determined using the location of the stagnation point. This is illustrated in Figure 3.6 with Case 1A from Figure 3.5.

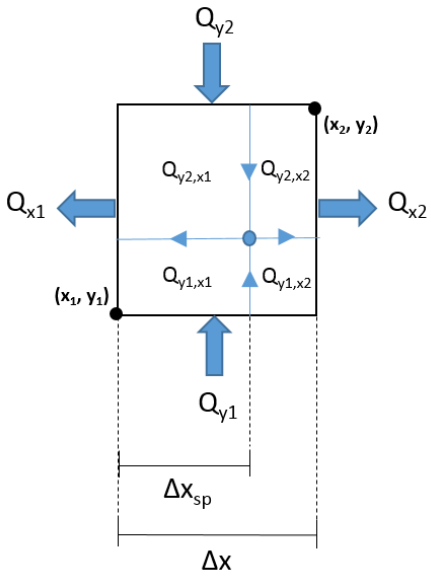

Figure 3.6. Schematic of Case 1A.

In Figure 3.6, Δx_{sp} is the distance of the stagnation point from point (x_1, y_1) along the x-axis and Δx is the total length of the cell along the x-axis. As such, $\frac{\Delta x_{sp}}{\Delta x}$ is the fraction of Q_{y1} routed to cell face x_1, while $1 - \frac{\Delta x_{sp}}{\Delta x}$ is the fraction of Q_{y1} routed to cell face x_2. The same can be said about the fractions of Q_{y2} routed to cell face x_1 and x_2, respectively.

Thus, using the segments delineated by the stagnation point in the cell, all the volumetric flow connections can be expressed as follows:

$$Q_{y1,x1} = \frac{\Delta x_{sp}}{\Delta x} |Q_{y1}| \quad \textbf{(Eq. 3.18)}$$

$$Q_{y1,x2} = \left(1 - \frac{\Delta x_{sp}}{\Delta x}\right) |Q_{y1}| \quad \textbf{(Eq. 3.19)}$$

$$Q_{y2,x1} = \frac{\Delta x_{sp}}{\Delta x} |Q_{y2}| \quad \textbf{(Eq. 3.20)}$$

$$Q_{y2,x2} = \left(1 - \frac{\Delta x_{sp}}{\Delta x}\right) |Q_{y2}| \quad \textbf{(Eq. 3.21)}$$

Note, only the flows from the inflow faces to the outflow faces need to be considered. This is because there is no flow in between the same flow boundaries (i.e., there is no flow between two inflow faces or two outflow faces).

As the location of the stagnation point is not known apriori, Δx_{sp} has to be represented in terms of the cell face flows. A plot of the velocity profile along the x-axis for Case 1A from Figure 3.6 is shown in Figure 3.7.

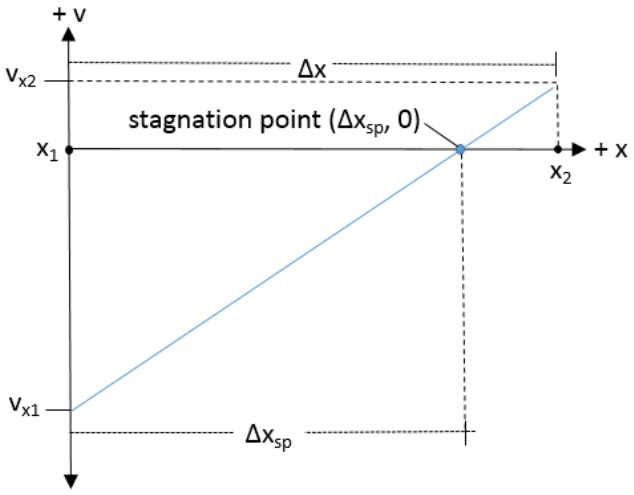

Figure 3.7. Plot of velocity profile along *x*-axis for Case 1A.

The velocities v_{x1} and v_{x2} can be expressed as:

$$v_{x1} = \frac{Q_{x1}}{\Delta y} \quad \textbf{(Eq. 3.22)}$$

$$v_{x2} = \frac{Q_{x2}}{\Delta y} \quad \textbf{(Eq. 3.23)}$$

Since the flow in the x-direction is negative at $x = x_1$ and positive at $x = x_2$, plotting the velocity in the x-direction as a function of distance along the x-axis yields a straight line with a positive gradient, starting at (x_1, v_{x1}), intersecting the x-axis at $(\Delta x_{sp}, 0)$ and stopping at (x_2, v_{x2}), where v_{x1} is negative and v_{x2} is positive. Thus, by virtue of similar triangles and using Eq. 3.22 and Eq. 3.23, Δx_{sp} can be expressed as,

$$\Delta x_{sp} = \Delta x \frac{\left|\frac{Q_{x1}}{\Delta y}\right|}{\left|\frac{Q_{x1}}{\Delta y}\right| + \left|\frac{Q_{x2}}{\Delta y}\right|} = \Delta x \frac{|Q_{x1}|}{|Q_{x1}| + |Q_{x2}|} \quad \textbf{(Eq. 3.24)}$$

or,

$$\Delta x_{sp} = \Delta x \, f_{x,sp} \quad \textbf{(Eq. 3.25)}$$

where, $f_{x,sp} = \frac{|Q_{x1}|}{|Q_{x1}| + |Q_{x2}|}$.

Substituting Eq. 3.25 in Eq. 3.18, Eq. 3.19, Eq. 3.20, and Eq. 3.21 yields:

$$Q_{y1,x1} = f_{x,sp} \, |Q_{y1}| \quad \textbf{(Eq. 3.26)}$$

$$Q_{y1,x2} = (1 - f_{x,sp})|Q_{y1}| \quad \textbf{(Eq. 3.27)}$$

$$Q_{y2,x1} = f_{x,sp}|Q_{y2}| \quad \textbf{(Eq. 3.28)}$$

$$Q_{y2,x2} = (1 - f_{x,sp}) \, |Q_{y2}| \quad \textbf{(Eq. 3.29)}$$

Now consider Case 1B from Figure 3.5 as shown in Figure 3.8.

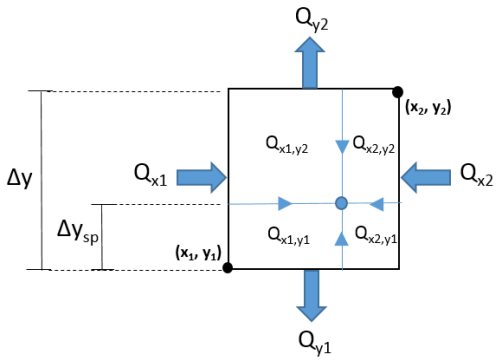

Figure 3.8. Schematic of Case 1B.

In this case, Δy_{sp} is the distance of the stagnation point from point (x_1, y_1) along the y-axis and Δy is the total length of the cell along the y-axis. Thus, all the volumetric flow connections for this case can be expressed as:

$$Q_{x1,y1} = \frac{\Delta y_{sp}}{\Delta y} |Q_{x1}| \quad \textbf{(Eq. 3.30)}$$

$$Q_{x1,y2} = \left(1 - \frac{\Delta y_{sp}}{\Delta y}\right) |Q_{x1}| \quad \textbf{(Eq. 3.31)}$$

$$Q_{x2,y1} = \frac{\Delta y_{sp}}{\Delta y} |Q_{x2}| \quad \textbf{(Eq. 3.32)}$$

$$Q_{x2,y2} = \left(1 - \frac{\Delta y_{sp}}{\Delta y}\right) |Q_{x2}| \quad \textbf{(Eq. 3.33)}$$

Plotting the velocity profile along the y-axis for 2D-Type 1 case (b) from Figure 3.8 allows an expression for Δy_{sp} to be obtained in the same manner as for Δx_{sp}. This is illustrated in Figure 3.9.

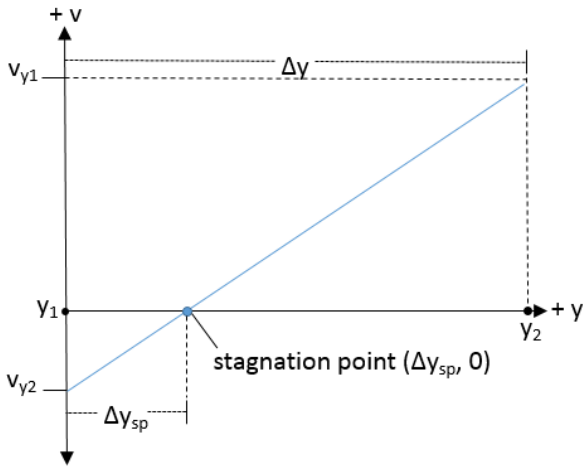

Figure 3.9. Plot of velocity profile along *y*-axis for Case 1B.

Thus, using similar triangles in Figure 3.9 and expressions of the cell face velocities in terms of the cell face flows, Δy_{sp} can be expressed as:

$$\Delta y_{sp} = \Delta y \, \frac{|Q_{y1}|}{|Q_{y1}| + |Q_{y2}|} \qquad \textbf{(Eq. 3.34)}$$

or,

$$\Delta y_{sp} = \Delta y \, f_{y,sp} \qquad \textbf{(Eq. 3.35)}$$

where, $f_{y,sp} = \frac{|Q_{y1}|}{|Q_{y1}| + |Q_{y2}|}$.

Substituting Eq. 3.35 in Eq. 3.30, Eq. 3.31, Eq. 3.32, Eq. 3.33 yields:

$$Q_{x1,y1} = f_{y,sp} \, |Q_{x1}| \qquad \textbf{(Eq. 3.36)}$$

$$Q_{x1,y2} = (1 - f_{y,sp}) |Q_{x1}| \qquad \textbf{(Eq. 3.37)}$$

$$Q_{x2,y1} = f_{y,sp} |Q_{x2}| \qquad \textbf{(Eq. 3.38)}$$

$$Q_{x2,y2} = (1 - f_{y,sp}) \, |Q_{x2}| \qquad \textbf{(Eq. 3.39)}$$

Note that for both cases, all the volumetric flow connections, $Q_{i,j}$, are expressed as the product of a stagnation point coefficient (i.e., $f_{x,sp}$, $1 - f_{x,sp}$, $f_{y,sp}$, or $1 - f_{y,sp}$) and the magnitude of the inflow component, $|Q_i|$. The stagnation point coefficient is related to the outflow component, Q_j, in two ways: the direction of the flow and the cell face at which the flow occurs. So, when the outflows are in the x-direction, the product includes the x-direction stagnation point coefficients ($f_{x,sp}$, and $1 - f_{x,sp}$) and when the outflows are in the y-direction, the product includes the y-direction stagnation point coefficients ($f_{y,sp}$, and $1 - f_{y,sp}$). The cell face of the outflow component, j, determines which of the stagnation point coefficients is used for the given coordinate direction (i.e., f_{sp} or $1 - f_{sp}$). Since the stagnation point locations are defined with respect to (x_1, y_1), f_{sp} always delineates the fraction of flow routed to the outflow face located along (x_1, y_1), while $1 - f_{sp}$ always delineates fraction of flow routed to the outflow face along (x_2, y_2). Thus, the general equation to determine the volumetric flow connections for Type 1 cases (the stagnation point cases), can be expressed as,

$$Q_{i,j} = sp_j \, |Q_i| \qquad \textbf{(Eq. 3.40)}$$

where, sp_j is the stagnation point coefficient ($f_{x,sp}$, $1 - f_{x,sp}$, $f_{y,sp}$ or, $1 - f_{y,sp}$), which is determined by the orientation (coordinate axes that it is perpendicular to) and location along the axis of outflow face, j.

Evaluating volumetric flow connections for the four cases assigned to Type 2 as shown in Figure 3.5 is a bit more challenging, because for each case (Case 2A, 2B, 2C, or 2D), it is possible to have three different flow regimes depending on the magnitudes of the cell face flows, whereby a particle tracked from an inflow corner can exit through one of the two outflow faces or through the outflow corner. Thus, there are 12 cases in total for Type 2. The three potential flow regimes for Case 2A are illustrated in Figure 3.10. Again, the inflow corners and outflow

corners were tracked using Pollock's method to delineate the dividing streamtubes for visualization.

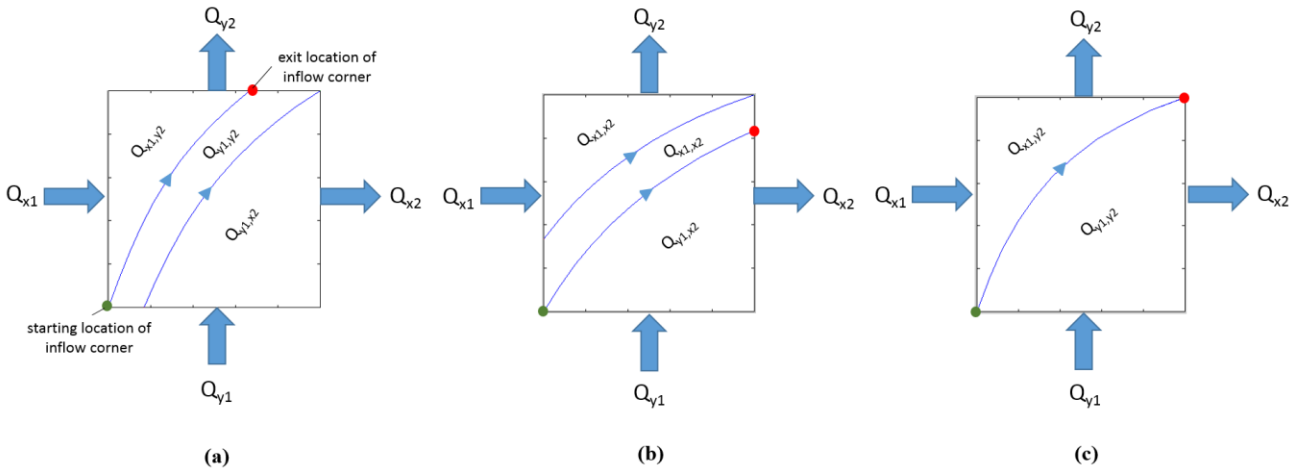

Figure 3.10. Schematics of the three potential flow regimes for Case 2A: flow regime I, particle tracked from inflow corner exits through one outflow face (a); flow regime II, particle tracked from inflow corner exits through the other outflow face (b); and flow regime III, particle tracked from inflow corner exits through the outflow corner (c).

Figure 3.10 shows that for Case 2A, depending on the cell face flow magnitudes, a particle tracked from corner x_1, y_1 can exit through either cell face y_2 (flow regime I), cell face x_2 (flow regime II), or through corner x_2, y_2 (flow regime III). The mass balance equation for all three cases in Figure 3.10 can be written as,

$$|Q_{y1}| + |Q_{x1}| = |Q_{y2}| + |Q_{x2}| \qquad \textbf{(Eq. 3.41)}$$

In the event that the particle exits through cell face y_2 (i.e., flow regime I), the following two statements must be true to ensure conservation of mass:

(1) The magnitude of Q_{y1} must be greater than that of Q_{x2}, i.e., $|Q_{y1}| > |Q_{x2}|$

(2) The magnitude of Q_{x1} must be less than that of Q_{y2}, i.e., $|Q_{x1}| < |Q_{y2}|$

Thus, if $|Q_{y1}| > |Q_{x2}|$ for Case 2A, the relevant volumetric flow connections are as follows:

$$Q_{y1,y2} = |Q_{y1}| - |Q_{y1,x2}| = |Q_{y1}| - |Q_{x2}| \quad \textbf{(Eq. 3.42)}$$

$$Q_{y1,x2} = |Q_{x2}| \quad \textbf{(Eq. 3.43)}$$

$$Q_{x1,y2} = |Q_{x1}| \quad \textbf{(Eq. 3.44)}$$

$$Q_{x1,x2} = 0 \quad \textbf{(Eq. 3.45)}$$

Note, only one of the conditions need to be considered (i.e., $|Q_{y1}| > |Q_{x2}|$), since if statement (1) is true, statement (2) must also be true.

Similarly, in the event that the particle exits through cell face y_2 (i.e., flow regime II), the following two statements must be true to ensure conservation of mass:

(3) The magnitude of Q_{y1} must be less than that of Q_{x2}, i.e., $|Q_{y1}| < |Q_{x2}|$

(4) The magnitude of Q_{x1} must be greater than that of Q_{y2}, i.e., $|Q_{x1}| > |Q_{y2}|$

Thus, if $|Q_{y1}| < |Q_{x2}|$ for Case 2A, the relevant volumetric flow connections are as follows:

$$Q_{y1,y2} = 0 \quad \textbf{(Eq. 3.46)}$$

$$Q_{y1,x2} = |Q_{y1}| \quad \textbf{(Eq. 3.47)}$$

$$Q_{x1,y2} = |Q_{y2}| \quad \textbf{(Eq. 3.48)}$$

$$Q_{x1,x2} = |Q_{x1}| - |Q_{x1,y2}| = |Q_{x1}| - |Q_{y2}| \quad \textbf{(Eq. 3.49)}$$

Finally, in the event that the particle exits through corner x_2, y_2 (i.e., flow regime III), the following two statements must be true to ensure conservation of mass:

(5) The magnitude of Q_{y1} must be equal to that of Q_{x2}, i.e., $|Q_{y1}| = |Q_{x2}|$

(6) The magnitude of Q_{x1} must be equal to that of Q_{y2}, i.e., $|Q_{x1}| = |Q_{y2}|$

Thus, if $|Q_{y1}| = |Q_{x2}|$ for Case 2A, the relevant volumetric flow connections are as follows:

$$Q_{y1,y2} = 0 \quad \textbf{(Eq. 3.50)}$$

$$Q_{y1,x2} = |Q_{x2}| \quad \textbf{(Eq. 3.51)}$$

$$Q_{x1,y2} = |Q_{x1}| \quad \textbf{(Eq. 3.52)}$$

$$Q_{x1,x2} = 0 \quad \textbf{(Eq. 3.53)}$$

Performing this exercise separately for each case is not desirable since it would not be computationally efficient. Thus, it is necessary to develop a common set of equations that would apply to all the Type 2 cases.

To do this, let us first define a 'reference inflow'. The reference inflow, Q_r, is the inflow at the cell face with the lower index, where the indices for the cell face flows increase in clockwise direction as follows: $Q_{x1} = 1$, $Q_{y2} = 2$, $Q_{x2} = 3$, and $Q_{y1} = 4$. Also, the indices are considered to be cyclic (i.e., 1 is lower than 2, 2 is lower than 3, 3 is lower than 4 and 4 is lower than 1).

For Case 2A, Q_{x1} and Q_{y1} are the inflows. This makes Q_{y1} the reference inflow since it has the lower index. Thus, the volumetric flow connections can be expressed in terms of the reference inflow as follows:

$$Q_{y1} = Q_r \quad \textbf{(Eq. 3.54)}$$

$$Q_{x1} = Q_{r+1} \quad \textbf{(Eq. 3.55)}$$

$$Q_{y2} = Q_{r+2} \quad \textbf{(Eq. 3.56)}$$

$$Q_{x2} = Q_{r+3} \quad \textbf{(Eq. 3.57)}$$

It turns out that the general sets of equations that apply to all the Type 2 cases can be derived by substituting Eq. 3.54, Eq. 3.55, Eq. 3.56, and Eq. 3.57 into Eq. 3.41. The substitution yields the general mass balance equation for all Type 2 cases:

$$|Q_r| + |Q_{r+1}| = |Q_{r+2}| + |Q_{r+3}| \quad \textbf{(Eq. 3.58)}$$

It follows that the first condition for flow regime I, which was $|Q_{y1}| > |Q_{x2}|$ for Case 2A, can be expressed as, $|Q_r| > |Q_{r+3}|$. The general equations for the relevant volumetric flow connections of this flow regime can then be expressed as:

$$Q_{r,r+2} = |Q_r| - |Q_{r+3}| \quad \textbf{(Eq. 3.59)}$$

$$Q_{r,r+3} = |Q_{r+3}| \quad \textbf{(Eq. 3.60)}$$

$$Q_{r+1,r+2} = |Q_{r+1}| \quad \textbf{(Eq. 3.61)}$$

$$Q_{r+1,r+3} = 0 \quad \textbf{(Eq. 3.62)}$$

Similarly, the second condition for the flow regime II becomes, $|Q_r| < |Q_{r+3}|$. The general equations for the corresponding relevant volumetric flow connections can be expressed as:

$$Q_{r,r+2} = 0 \quad \textbf{(Eq. 3.63)}$$

$$Q_{r,r+3} = |Q_r| \quad \textbf{(Eq. 3.64)}$$

$$Q_{r+1,r+2} = |Q_{r+2}| \quad \textbf{(Eq. 3.65)}$$

$$Q_{r+1,r+3} = |Q_{r+1}| - |Q_{r+2}| \quad \textbf{(Eq. 3.66)}$$

Finally, the last condition for flow regime III becomes, $|Q_r| = |Q_{r+3}|$. The general equations for the corresponding relevant volumetric flow connections can be expressed as:

$$Q_{r,r+2} = 0 \quad \textbf{(Eq. 3.67)}$$

$$Q_{r,r+3} = |Q_r| \quad \textbf{(Eq. 3.68)}$$

$$Q_{r+1,r+2} = |Q_{r+1}| \quad \textbf{(Eq. 3.69)}$$

$$Q_{r+1,r+3} = 0 \quad \textbf{(Eq. 3.70)}$$

Thus, to determine the volumetric flow connections for the Type 2 cases, one needs only to define the reference inflow, then check for the three conditions for each of the possible flow regimes and apply the appropriate set of equations.

3.3.3 All Other Cases

It turns out that for all the remaining cases, whenever the number of inflows are greater than the number of outflows, there is only one outflow; whenever the number of outflows are greater than the number inflows, there is only one inflow; and lastly, whenever the number of inflows and outflows are equal, there is only one inflow and one outflow (i.e., the only remaining cases with equal number of inflows and outflows are cases where there is one inflow, one outflow, and two no-flows). Thus, all these cases can be grouped into the following categories: (1) single inflow (2) single outflow, and (3) single inflow-single outflow. Three examples from each of the categories are shown in Figure 3.11. In Figure 3.11, the dividing streamtubes were recreated for visualization by forward tracking the inflow corners of the single outflow case, shown in Figure 3.11 (a), and backward tracking the outflow corner of the single inflow case, shown in Figure 3.11 (b).

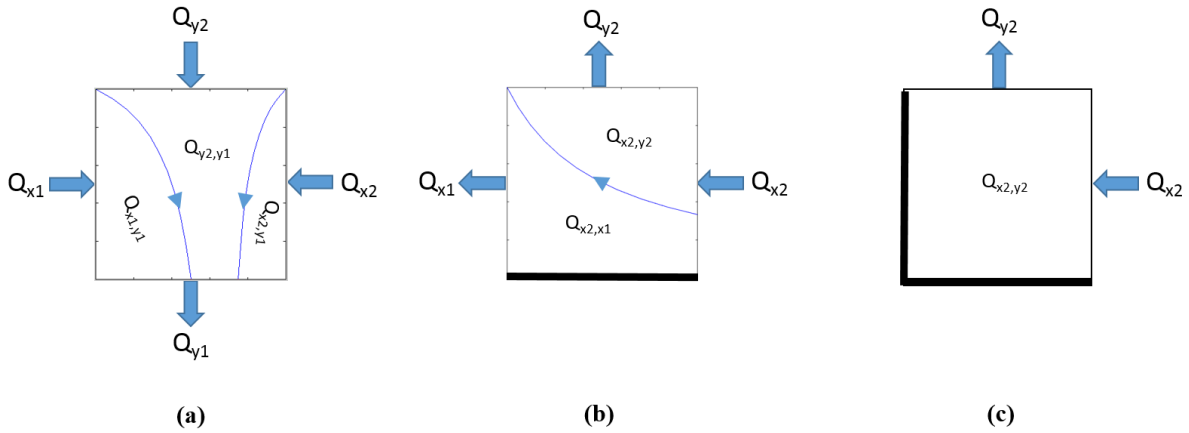

Figure 3.11. Three examples of remaining cases: four non-zero flows with single outflow (a), three non-zero flows with single inflow (b), and two non-zero flows with single inflow and single outflow (c).

Note in Figure 3.11 (a), that all faces are inflow faces except one. This may imply the presence of a "weak" sink inside the cell, whereby it is removing water inside the cell but it is not strong enough to induce inward flow along all the cell faces like a "strong" sink. However recall that the method assumes there is no internal removal of water inside the cell and hence, all the water that enters the cell in Figure 3.11 (a) is assumed to exit through the single outflow face. As such, the method effectively assumes that there are no weak sinks or sources inside the cells.

Now, for any non-trivial case (i.e., at least two cell faces are hydraulically connected), the magnitude of inflow at a given cell face *i* has to be equal to the sum of its components routed to all *n* connected outflow faces. This can be expressed as,

$$|Q_i| = \sum_{k}^{n} Q_{i,k} \qquad \textbf{(Eq. 3.71)}$$

where, $|Q_i|$ is the volumetric inflow at cell face i and $Q_{i,k}$ is the component of Q_i flowing to cell face k.

Similarly, the magnitude of outflow at a given cell face *j* has to be equal to the sum of its components sourced from all *n* connected inflow faces. This can be expressed as,

$$|Q_j| = \sum_{k}^{n} Q_{k,j} \qquad \textbf{(Eq. 3.72)}$$

where, $|Q_j|$ is the volumetric outflow at cell face j and $Q_{k,j}$ is the component of Q_j flowing in from cell face k.

Now, consider the three inflows-single outflow case shown in Figure 3.11(a). Since there is only one outflow, Eq. 3.71 can be expressed as,

$$|Q_i| = Q_{i,j} \qquad \textbf{(Eq. 3.73)}$$

where, j is the index of the outflow face.

That is, the magnitude of inflow at any given cell face i, $|Q_i|$, is simply the amount flowing in from that inflow face to the single outflow face, $Q_{i,j}$. Thus, for all remaining cases where the number of inflows are greater than the number of outflows (i.e., for all non-trivial cases with a single outflow), the volumetric flow connections can be expressed as,

$$Q_{i,j} = |Q_i| \quad \textbf{(Eq. 3.74)}$$

This can also be visually validated from in Figure 3.11(a). Since there is only one outflow, the streamtubes emanating from the each of the inflow faces must end up on the single outflow face.

Similarly, for the single inflow case shown in Figure 3.11(b) Eq. 3.72 becomes,

$$|Q_j| = Q_{i,j} \quad \textbf{(Eq. 3.75)}$$

where, i is the index of the inflow face.

That is, the magnitude of outflow at any given cell face j, is simply the amount flowing to that outflow face from the single inflow face. Thus, for all remaining cases where the number of outflows are greater than the number of inflows (i.e., for all non-trivial cases with a single inflow), the volumetric flow connections can be expressed as,

$$Q_{i,j} = |Q_j| \quad \textbf{(Eq. 3.76)}$$

The only cases that remain are the single inflow-single outflow-two no flow cases. For all these cases the single inflow must be equal to the single outflow to preserve mass balance (i.e., $|Q_i| = |Q_j|$). Thus, the volumetric flow connections for these cases can be calculated with either Eq. 3.74 or Eq. 3.76. The algorithm simply treats these cases same as the cases where the number of inflows are greater than number of outflows (i.e., using Eq. 3.74).

3.3.4 Summary of 2D-Algorithm

The general equations described in the preceding sections can be embedded in a simple algorithm to determine all the flows between each of the faces of a single two-dimensional rectilinear finite-difference cell (the 2D-algorithm). The results of the 2D-algorithm can outputted in the form of a matrix, called the flow connection matrix (FCM). For a two-dimensional rectilinear cell the FCM can be expressed as,

$$FCM = \begin{bmatrix} \mathrm{X} & Q_{x1,y2} & Q_{x1,x2} & Q_{x1,y1} \\ Q_{y2,x1} & \mathrm{X} & Q_{y2,x2} & Q_{y2,y1} \\ Q_{x2,x1} & Q_{x2,y2} & \mathrm{X} & Q_{x2,y1} \\ Q_{y1,x1} & Q_{y1,y2} & Q_{y1,x2} & \mathrm{X} \end{bmatrix} \quad \textbf{(Eq. 3.77)}$$

Note, that the elements along the diagonal of the FCM matrix represent flows from a cell face to itself (i.e., $Q_{x1,x1}$), and as such they are blanks. Also note that volumetric flow connections on either side of the diagonal in the FCM matrix represent the same flows but in opposite directions. For example, if for a particular case there is a flow connection from cell face x_1 (the inflow face) to cell face y_2 (the outflow face), then $Q_{x1,y2}$ is positive. Therefore, $Q_{y2,x1}$ is simply $-Q_{x1,y2}$. This can be generally expressed as,

$$FCM(i,j) = -FCM(j,i) \quad \textbf{(Eq. 3.78)}$$

The first step of the 2D-algorithm is to fill the FCM matrix with zeros. Then the cell face flows for the given cell are obtained from the cell-by-cell flows outputted by a finite-difference flow model like MODFLOW. The cell face flows are used to determine which case to be applied to the cell (i.e., 'trivial', 'two-inflows two-outflows Type 1', 'two-inflows two-outflows Type 2'or 'all other cases'). Once the case has been established, then for each inflow-outflow connection the appropriate equation is applied to evaluate the flow for that connection (i.e., the flow through each dividing streamtube is computed). After the flows for all the connections are evaluated, the remaining elements of the FCM matrix are populated in using Eq. 3.78.

A flow chart outlining the algorithm for computing the distribution of flow in two-dimensional rectilinear cell is presented in Figure 3.12.

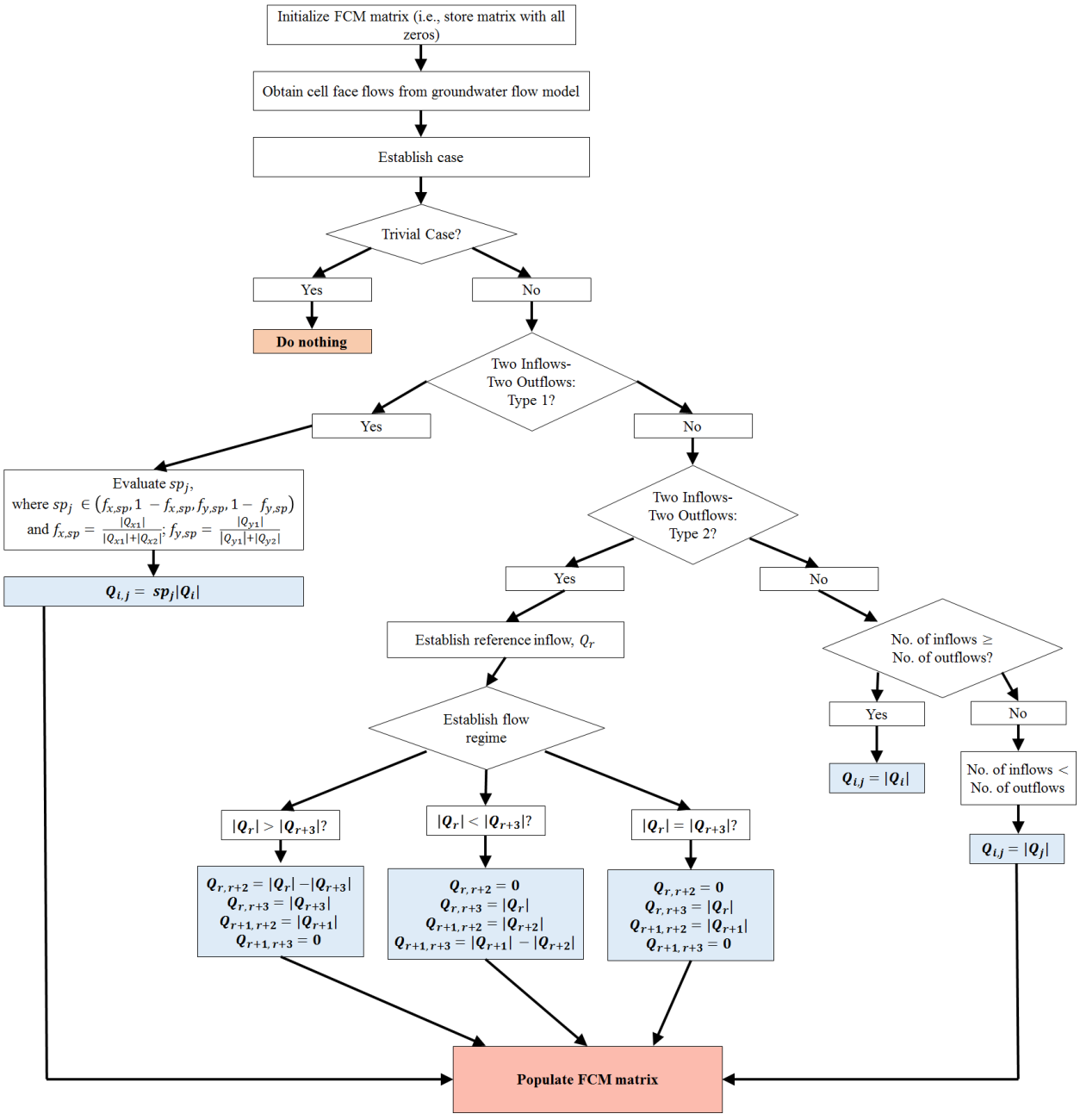

Figure 3.12. Flow chart of algorithm for computing volumetric flow connections in a two-dimensional rectilinear finite-difference cell; the blue boxes indicate the equations used for determining flow connections; the red boxes indicate terminal points in the flow chart.

3.4 Computing Flow Connections in a Three-Dimensional Rectilinear Cell

A three-dimensional rectilinear finite-difference has six cell faces, as illustrated for Pollock's method (Pollock, 1988) in Figure 3.1. Each cell face can either be (1) an inflow face, (2) an outflow or, (3) a no-flow face. This yields 3^6 or 729 potential cell face flow boundary permutations. Again, careful observation revealed that the 729 cases can be reduced to five general types of cases: (1) trivial cases, (2) stagnation point cases, (3) single inflow and/or single outflow cases, (4) cases compatible with 2D-algorithm, and (5) all other cases. For the special cases, numbered (1) to (4), the volumetric flow connections can be evaluated directly by simply applying mass-balance inside the cell similar to the 2D-algorithm. However, in order to evaluate the volumetric flow connections for all the other cases, it is necessary to recreate the streamtube geometry inside the cell using Pollock's method. Though the special cases (e.g., all no-flow cell face boundaries, strong sink/source inside the cell, stagnation point inside the cell, single inflow/single outflow) represent only a small fraction of the type of flow boundaries typically encountered by a cell in a groundwater model, the significant reduction in computation time for these cases as a result of using the mass balance approach warranted differentiating them from the cases that require streamtube geometry recreation inside the cell.

3.4.1 Trivial Cases

The trivial cases in three-dimensions are analogous to the two-dimensional cases. These include all the cases where there is a strong sink or source inside the cell or there is no flow inside the cell. Figure 3.13 illustrates the three-dimensional analogs of the trivial cases illustrated in Figure 3.4. Again, since none of the cell faces are hydraulically connected, all volumetric flow connections are zero for these cases.

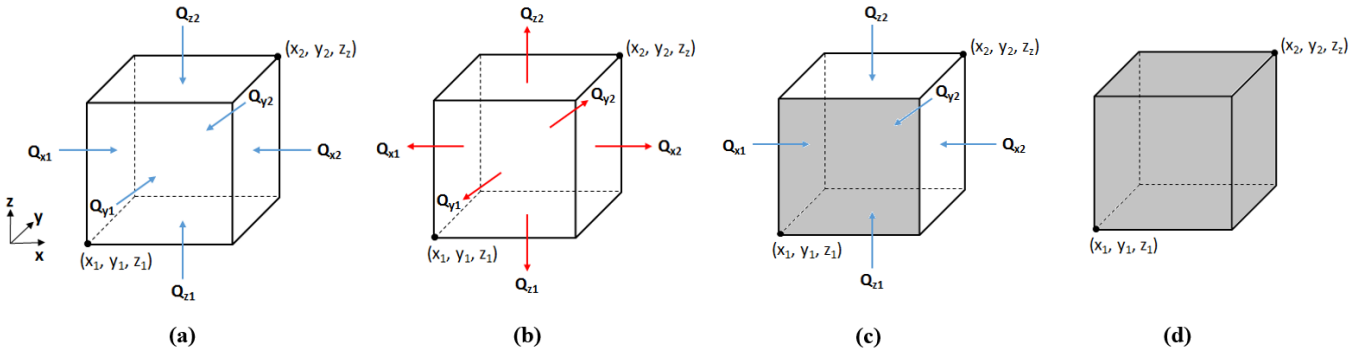

Figure 3.13. Schematics of trivial cases for three-dimensional cell: strong sink (a), strong source (b), strong sink with a no-flow boundary at cell face y_1 (c), all no-flow boundaries (d); inflows are shown with blue arrows and outflows are shown with red arrows.

3.4.2 Single Inflow and/or Single Outflow

The equations developed to handle all single inflow and/or single outflow cases for the 2D-algorithm are also applicable for the three-dimensional cell. This is because the same principle holds. That is, given no internal removal or addition of water inside the cell and a steady-state flow field, all inflows must be equal to the sum of their components routed to all connected outflow faces and all outflows must be equal to the sum of their components sourced from all connected inflow faces. Thus, like the 2D-algorithm, for any non-trivial case, whenever there is a single outflow or a single inflow and single outflow, volumetric flow connections are calculated using Eq. 3.74 and whenever there is a single inflow, volumetric flow connections are calculated using Eq. 3.76. The equations are shown again below:

For single outflows and single outflow-single inflow,

$$Q_{i,j} = |Q_i| \qquad \textbf{(Eq. 3.74)}$$

For single inflows,

$$Q_{i,j} = |Q_j| \qquad \textbf{(Eq. 3.76)}$$

Figure 3.14 illustrates an example of a single outflow case. The streamtube geometry has been recreated in the figure for visualization purposes only. This was done by releasing particles along all the inflow edges (i.e., edges shared by two inflow faces) and then forward tracking them using Pollock's method until they exit the cell. All the particles exit through the single outflow face and the path lines of the particles delineate the stream surfaces of the dividing streamtubes inside the cell.

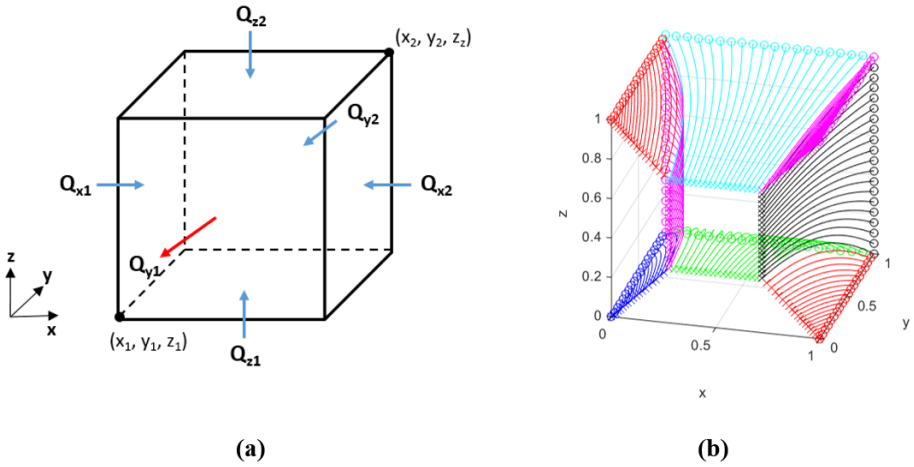

Figure 3.14. Example of a single outflow case for a three-dimensional rectilinear finite-difference cell of unit dimensions: a cell with inflows of equal magnitude along five cell faces and a single outflow along cell face y_1 (a); and recreation of dividing streamtubes by releasing particles along inflow edges and forward tracking them using Pollock's method till they exit through the single outflow face (b).

From Figure 3.14, the use of Eq. 3.74 for handling these cases can be validated visually. In Figure 3.14, since there is only one outflow face, the streamtubes emanating from each of the inflow faces must end up on the single outflow face. Thus, the amount of flow between any given inflow face to the single outflow face is simply the amount flowing in from that inflow face (i.e., $Q_{i,j} = |Q_i|$).

Now consider the single inflow case shown in Figure 3.15, where the flows for the cell shown in Figure 3.14 are simply reversed. For this case, the dividing streamtubes were recreated inside the cell again for visualization. This time though since there are no inflow edges, it was done by backward tracking particles along all the outflow edges (i.e., edges shared by two

outflow faces) using Pollock's method until they exit through the single inflow face. Note, we obtain the same streamtube geometry inside the cell, except that the flows through the streamtubes are simply in the opposite direction.

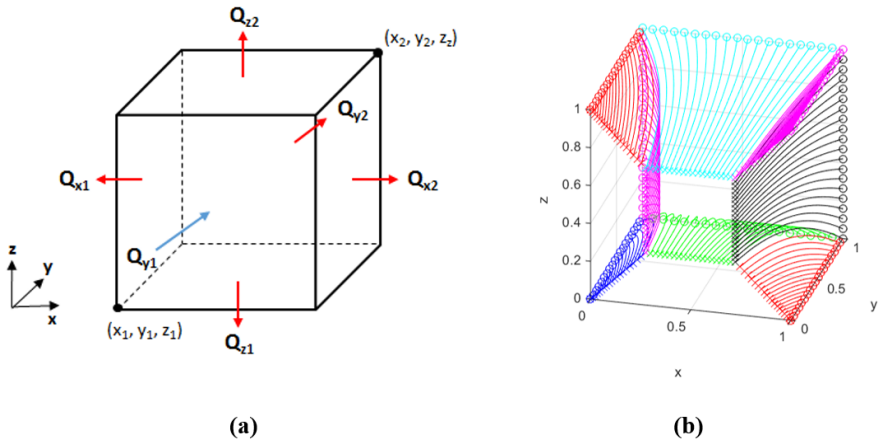

Figure 3.15. Example of a single inflow case for a three-dimensional rectilinear finite-difference cell of unit dimensions: a cell with outflows of equal magnitude along five cell faces and a single inflow along cell face y_1 (a); and recreation of dividing streamtubes by releasing particles along outflow edges and backward tracking them using Pollock's method till they exit through the single inflow face (b).

Again with Figure 3.15, we can visually validate the use of Eq. 3.76 – the amount of flow between the single inflow face and any given outflow face is simply the amount flowing out of that outflow face (i.e., $Q_{i,j} = |Q_j|$).

3.4.3 Stagnation Point Cases

Stagnation points can only arise inside the cell for cases when there are three or more non-zero cell face flows. Some of these cases are illustrated in Figure 3.16. Note from Figure 3.16, that the stagnation point cases with three non-zero flows must have either only one inflow or only one outflow. Thus, they get handled by the 'single inflow and/or single outflow' routine and need not be dealt with here. As such, the stagnation point cases for the three-dimensional cell include only those with four or more non-zero cell face flows.

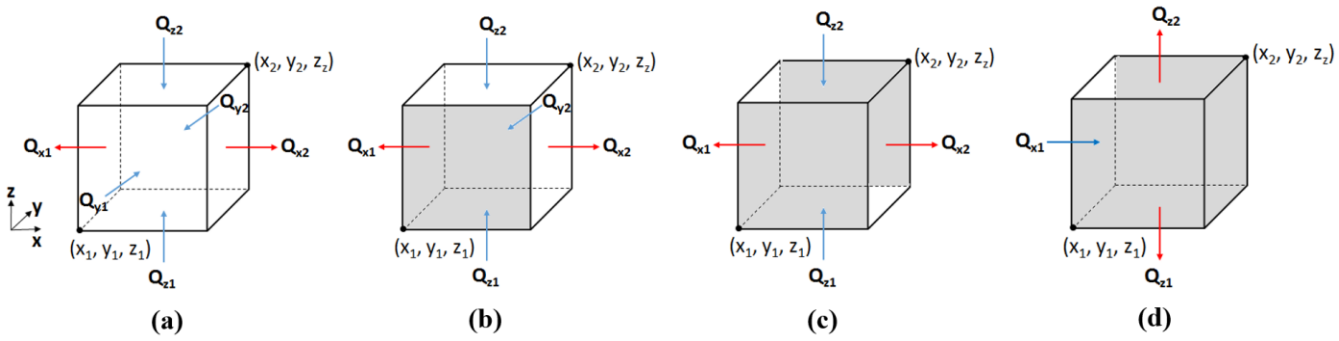

Figure 3.16. Examples of stagnation point cases for a three-dimensional rectilinear finite-difference cell: six non-zero flows (a); five non-zero flows (b); four non-zero flows (c); and three non-zero flows (d).

To illustrate how these cases are handled, consider the case with six non-zero cell face flows shown in Figure 3.17 (a). In this case, Q_{y1}, Q_{y2}, Q_{z1}, and Q_{z2} are all inflows and Q_{x1} and Q_{x2} are both outflows. As the flows along each coordinate direction are in opposite directions, there will be a plane of zero-velocity along each of the coordinate directions, as shown in Figure 3.17 (a). Now, let Δx_{sp}, Δy_{sp}, and Δz_{sp} be the distance from (x_1, y_1, z_1) to the location of the stagnation point along the x-, y-, and z- axes respectively, as shown in Figure 3.17 (b). Δx_{sp}, Δy_{sp}, and Δz_{sp} can be determined directly from the cell face flows as described for the 2D-algorithm. Expressions for Δx_{sp} and Δy_{sp} were already developed for the 2D-algorithm and the same expressions hold for the three-dimensional cell.

For Δz_{sp}, if the velocity profile is plotted along the z-direction, by virtue of similar triangles, it can be expressed as:

$$\Delta z_{sp} = \Delta z \frac{|Q_{z1}|}{|Q_{z1}| + |Q_{z2}|} \qquad \textbf{(Eq. 3.79)}$$

or,

$$\Delta z_{sp} = \Delta z \, f_{z_{sp}} \qquad \textbf{(Eq. 3.80)}$$

where, $f_{z_{sp}} = \frac{|Q_{z1}|}{|Q_{z1}| + |Q_{z2}|}$.

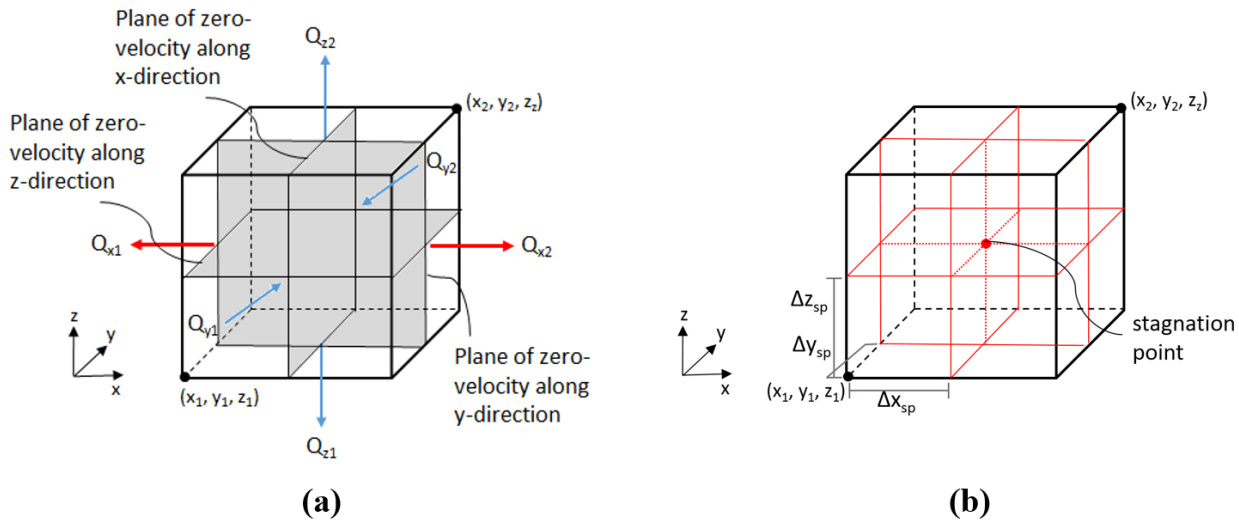

Figure 3.17. Three-dimensional stagnation point case with six non-zero flows: flows in opposite directions induce planes of zero-velocity inside the cell along each of the coordinate directions (a); a stagnation point exists at the intersection of the zero-velocity planes at $(\Delta x_{sp}, \Delta y_{sp}, \Delta z_{sp})$ (b).

Now consider Q_{y1}. Figure 3.17 (a) shows that the zero-velocity plane along the x-direction delineates the dividing boundary between the two streamtubes flowing out of cell face y_1. One of the streamtubes flow into cell face x_1 and the other flows into cell face x_2. By Eq. 3.71, which was developed in Section 3.3.3 and shown again below, the magnitude of flow at any inflow face is given by the sum of all the its components routed to each connected outflow face,

$$|Q_i| = \sum_{k}^{n} Q_{i,k} \qquad \textbf{(Eq. 3.71)}$$

Thus, the magnitude of Q_{y1} can be expressed as,

$$|Q_{y1}| = \sum_{k}^{2} |Q_{y1,k}| = |Q_{y1,x1}| + |Q_{y1,x2}| \qquad \textbf{(Eq. 3.81)}$$

Since the cell face flow velocities are evenly distributed over the entire area of the cell face, Eq. 3.81 can be re-written as,

$$|Q_{y1}| = |v_{y1}|A_{y1,x1} + |v_{y1}|A_{y1,x2} \quad \textbf{(Eq. 3.82)}$$

where, v_{y1} is the flow velocity at cell face y_1; $A_{y1,x1}$ is the area delineated on cell face y_1 by the streamtube routing flow from cell face y_1 to cell face x_1; and $A_{y1,x2}$ is the area delineated on cell face y_1 by the streamtube routing flow from cell face y_2 to cell face x_2.

Now, the flow velocity at cell face y_1, v_{y1}, is equal to the volumetric flow through cell face y_1, Q_{y1}, divided by the area of cell face y_1, A_{y1}. Using this definition of v_{y1}, Eq. 3.82 becomes,

$$|Q_{y1}| = \frac{|Q_{y1}|}{A_{y1}}A_{y1,x1} + \frac{|Q_{y1}|}{A_{y1}}A_{y1,x2} = \frac{A_{y1,x1}}{A_{y1}}|Q_{y1}| + \frac{A_{y1,x2}}{A_{y1}}|Q_{y1}| \quad \textbf{(Eq. 3.83)}$$

Thus, the volumetric flow connections $Q_{y1,x1}$ and $Q_{y1,x2}$ can be expressed as:

$$Q_{y1,x1} = \frac{A_{y1,x1}}{A_{y1}}|Q_{y1}| = \frac{\Delta x_{sp}\Delta z}{\Delta x \Delta z}|Q_{y1}| = \frac{\Delta x_{sp}}{\Delta x}|Q_{y1}| = f_{x,sp}|Q_{y1}| \quad \textbf{(Eq. 3.84)}$$

$$Q_{y1,x2} = \frac{A_{y1,x2}}{A_{y1}}|Q_{y1}| = \frac{(\Delta x - \Delta x_{sp})\Delta z}{\Delta x \Delta z}|Q_{y1}| = \left(1 - \frac{\Delta x_{sp}}{\Delta x}\right)|Q_{y1}| = \left(1 - f_{x,sp}\right)|Q_{y1}| \quad \textbf{(Eq. 3.85)}$$

Carrying out the same exercise for the remaining volumetric flow connections yields:

$$Q_{y2,x1} = f_{x,sp}|Q_{y2}| \quad \textbf{(Eq. 3.86)}$$

$$Q_{y2,x2} = \left(1 - f_{x,sp}\right)|Q_{y2}| \quad \textbf{(Eq. 3.87)}$$

$$Q_{z1,x1} = f_{x,sp}|Q_{z1}| \quad \textbf{(Eq. 3.88)}$$

$$Q_{z1,x2} = \left(1 - f_{x,sp}\right)|Q_{z1}| \quad \textbf{(Eq. 3.89)}$$

$$Q_{z2,x1} = f_{x,sp}|Q_{z2}| \quad \textbf{(Eq. 3.90)}$$

$$Q_{z2,x2} = \left(1 - f_{x,sp}\right)|Q_{z2}| \quad \textbf{(Eq. 3.91)}$$

Note, we would arrive at the same expressions for all the volumetric flow connections had we used the general equation, Eq. 3.40, developed to handle stagnation point cases for the 2D-algorithm (i.e., using $Q_{i,j} = sp_j\,|Q_i|$). Thus, Eq. 3.40 is also applicable for a three-dimensional cell. However, an additional stagnation point coefficient term has to be defined in the z-direction.

3.4.4 Cases compatible with 2D-Algorithm

Careful observation revealed that the volumetric flow connections for cases where there are four non-zero cell face flows and all the flows lie on the same plane (i.e., the flows are only in any two coordinate directions: x-y, x-z, or y-z) can be determined by directly applying the 2D-algorithm described in Section 3.3.4. Some of these cases are illustrated in Figure 3.18.

To determine the volumetric flow connections in three-dimensions, the flows are first projected onto a two-dimensional plane, such that they can be assigned to Q_{x1}, Q_{y2}, Q_{x2}, and Q_{y1} as per the definition of the cell face flows in the 2D-algorithm. After this step, the 2D-algortihm can be applied as is, whereby the reference inflow is determined first and then the volumetric flow connections are calculated using the correct set of equations from Eq. 3.59 to Eq. 3.70 depending on which of the three conditions exist.

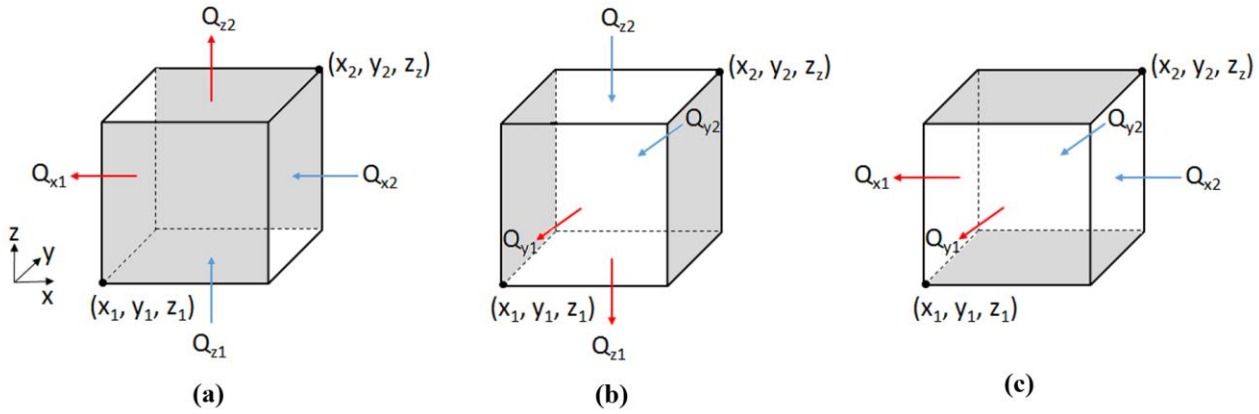

Figure 3.18. Examples of three-dimensional cases that are compatible with the 2D-algorithm: two no-flow boundaries along the y-axis (a), two no-flow boundaries along the x-axis (b), and two no-flow boundaries along the z-axis (c).

Note, the routine for ‘all other cases’ of the 2D-algorithm gets handled by the ‘single-inflow and/or single-outflow’ routine for the three-dimensional cell, while the ‘Type 1’ routine of the 2D-alogirhtm gets handle by the ‘stagnation point’ routine of the three-dimensional cell. Thus, those routines from the 2D-algorithm need not be applied for the three-dimensional cell.

3.4.5 All Other Cases (Streamtube Recreation Cases)

All cases with three or less non-zero flows and four non-zero flows with planar flow (i.e., the two no-flow boundaries are oriented in the same direction) get handled by the routines described in the preceding sub-sections. Hence, the cases that remain all have four or more non-zero cell face flows. For all these cases the volumetric flow connections have to be determined by recreating the streamtube geometry inside the cell using particle tracking, which can be done numerically or analytically. In most groundwater flow models these cases (especially those with six non-zero flows) will be the overwhelming majority and as such are the most important to optimize. Thus, an analytical approach was preferred since it represents a significant computational advantage over numerical particle tracking and also avoids any issues related to insufficient number of particles.

To illustrate how these cases are handled, consider the case with three inflows and three outflows shown in Figure 3.19 (a). Again, to recreate the streamtube geometry inside the cell, we need to forward track a set of particles along all the inflow edges using Pollock’s method as shown in Figure 3.19 (b).

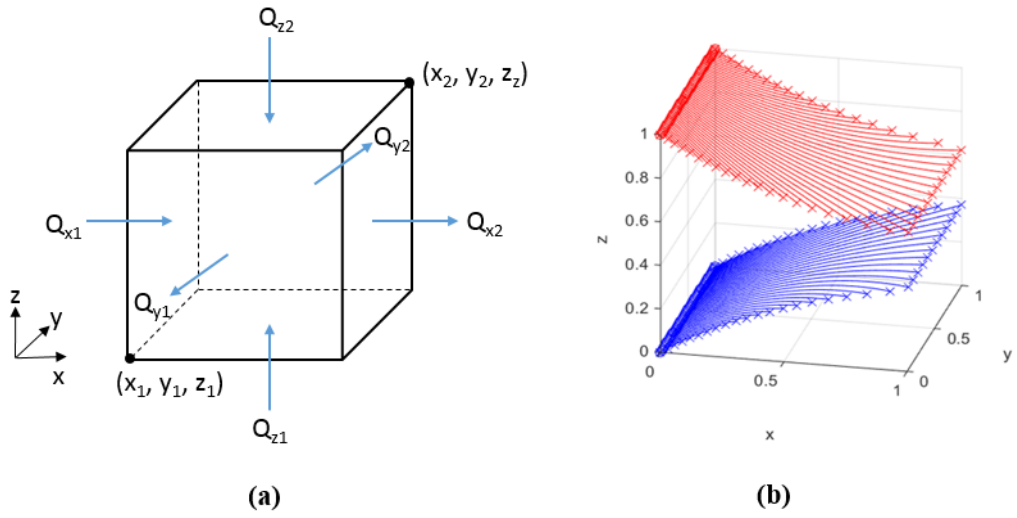

Figure 3.19. An example of a case for which the internal streamtube geometry has to be recreated to determine volumetric flow connections (a); 50 particles forward tracked using Pollock's method from each inflow edge, one along the y-axis at $z = 0$ and the other along the y-axis at $z = 1$ (b).

Of course, in the limit that an infinite number of particles are tracked we approach full recreation of the stream surfaces. The resulting curves delineated on the outflow faces by the exit locations of the released particles represent the boundaries of the dividing streamtubes inside the cell. Figure 3.20 shows one of the outflow faces from the cell shown in Figure 3.19, assuming an infinite number of particles are tracked.

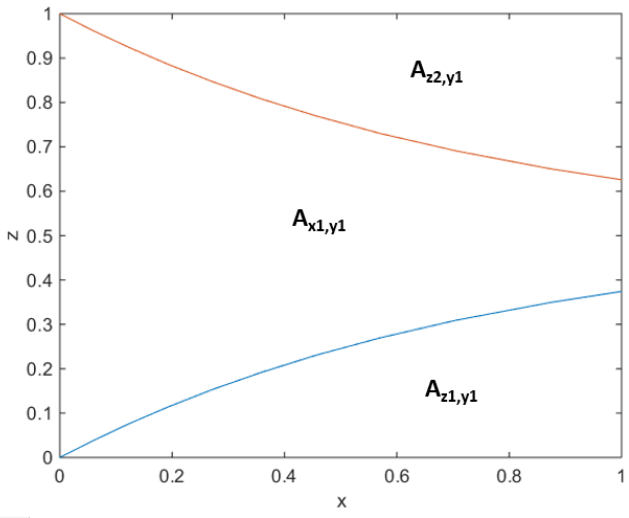

Figure 3.20. Cell face y_1 (x-z face at $y = 0$) from the cell in Figure 3.19; $A_{z2,y1}$, $A_{x1,y1}$, and $A_{z1,y1}$ are the areas delineated on this outflow face by the streamtubes emanating from cell faces z_2, x_1, and z_1 respectively.

The flow velocity at this cell face, v_j, is given by the total flow out of the cell face, Q_j, divided by the product of the total area of the cell face, A_j, and the cell porosity, n,

$$v_j = \frac{Q_j}{nA_j} \quad \textbf{(Eq. 3.92)}$$

where, the subscript, j, refers to the index of the outflow face.

Now, let $A_{i,j}$ be the area on outflow face j bounded by the particles released from inflow face i as shown in Eq. 3.93. Thus, the volumetric flow from inflow face i to outflow face j can be expressed as,

$$Q_{i,j} = v_j n A_{i,j} \quad \textbf{(Eq. 3.93)}$$

Substituting Eq. 3.92 in equation Eq. 3.93 for v_j, gives,

$$\boldsymbol{Q_{i,j} = \frac{A_{i,j}}{A_j} Q_j} \quad \textbf{(Eq. 3.94)}$$

Eq. 3.94 is the general equation to calculate the volumetric flow from an arbitrary inflow face to an arbitrary outflow face. Both A_j and Q_j are known apriori because the first is an input to the flow model and the latter is an output of running the flow model. Thus, the only unknown in Eq. 3.94 is $A_{i,j}$.

To evaluate $A_{i,j}$, or the flow connection areas, they can be sorted into two groups: throughflow areas and non-throughflow areas. For throughflow areas, the outflow boundary occurs along the same coordinate axis as the inflow, while for non-throughflow areas the outflow and inflow boundaries occur along different coordinate axes as shown in Figure 3.21. It turns out that whenever there is no throughflow along an outflow face for a given connection, i, j, the flow connection area, $A_{i,j}$, is always the area under the curve(s) delineated by the exit locations of the particles from inflow face i; and when there is throughflow, the flow connection area, $A_{thruflo}$,

is always the difference between the total area of outflow face j, A_j, and the sum of all the flow connection areas associated with no throughflows, $A_{non-thruflo}$. The latter can be expressed as,

$$A_{thruflo} = A_j - \sum_{k=1}^{n} A_{non-thruflo_k} \quad \textbf{(Eq. 3.95)}$$

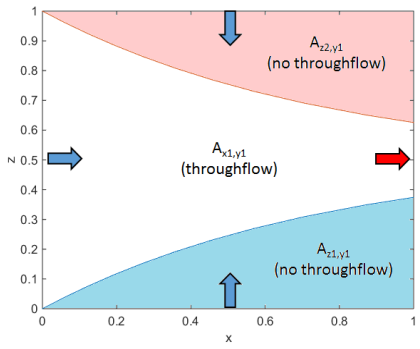

Figure 3.21. Throughflow and non-throughflow areas on cell face y_1 (x-z face at $y = 0$) from the cell in Figure 3.19. $A_{z2,y1}$ and $A_{z1,y1}$ have no throughflow and thus are calculated as the areas under the curves (the shaded areas). $A_{x1,y1}$ has throughflow and is calculated as the difference between the total area of this outflow face and the sum of $A_{z2,y1}$ and $A_{z1,y1}$.

In Figure 3.21, since $A_{z2,y1}$and $A_{z1,y1}$ have no throughflow, they are calculated as the areas under the curves. $A_{x1,y1}$ has throughflow and thus can be calculated as,

$$A_{x1,y1} = A_{y1} - (A_{z2,y1} + A_{z1,y1}) \quad \textbf{(Eq. 3.96)}$$

To determine the non-throughflow connection areas, we first develop expressions for the curves directly by manipulating the equations used for particle tracking in Pollock's method. It turns out that a direct by-product of Pollock's method is that all edges tracked to adjacent faces are curved and all edges tracked to a non-adjacent face are straight lines parallel to the edge. The result of this phenomenon is that the curves are either linear or simple polynomials and hence analytically integrable. Note, an adjacent face to an edge is defined as cell face that shares a one corner with that edge.

To illustrate how the expressions are developed, consider again the case from Figure 3.19. Figure 3.22 (a) shows a recreation of the dividing streamtubes inside the cell through particle

tracking. Figure 3.22 (b) shows outflow face y_1 again, where there are two curves. Since cell face y_1 is adjacent to the tracked inflow edges shown in Figure 3.22 (a), we will call the curves $C1_{adj}$ and $C2_{adj}$. $C1_{adj}$ is the curve delineating area $A_{z1,y1}$ and represents the boundary of the streamtube emanating from inflow face z_1 and $C2_{adj}$ is the curve delineating area $A_{z2,y1}$ and represents the boundary of the streamtube emanating from inflow face z_2.

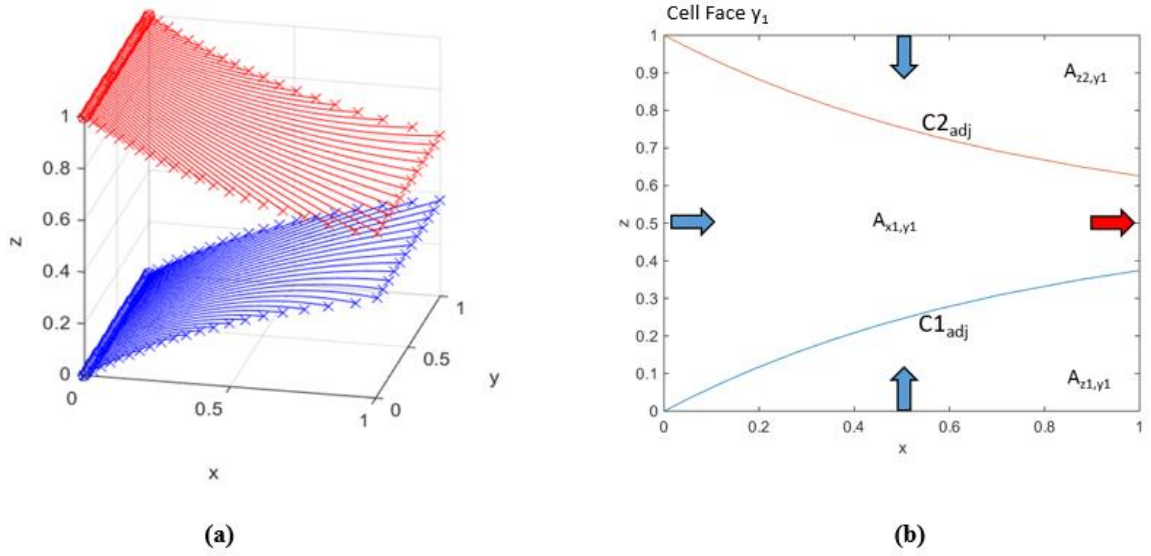

Figure 3.22. Developing analytically integrable expression for adjacent curves: particles forward tracked using Pollock's method from inflow edges for a three inflow-three outflow case (a); and boundaries of dividing stream surfaces (curves) on an adjacent face (b).

To develop an expression for $C1_{adj}$ and $C2_{adj}$, we must first determine the directions of the ordinate axes by which they will be defined. The ordinate direction for the curves is always taken to be the direction of the inflow that generated the curve. For example, Figure 3.22 (b), $C1_{adj}$ is generated by the streamtube emanating from cell face z_1, which has inflow direction in the positive z-direction, thus the ordinate direction for $C1_{adj}$ is also in the positive z-direction. However, $C2_{adj}$ in Figure 3.22 (b), is generated by the streamtube emanating from cell face z_2, which has inflow direction in the negative z-direction and consequently the ordinate direction for $C2_{adj}$ is in the negative z-direction. It was found that choosing the ordinate directions in this

manner allows for the simple rule of determining the flow connection areas described earlier, whereby, the flow connection area for non-throughflow areas is always the area under the curve bounding it and for throughflow areas, it is always the difference between the total area of the outflow face and the sum of the non-throughflow areas.

Now we can proceed to develop an expression for $C1_{adj}$. Since the curve lies on the x-z plane and its ordinate is along the z-axis (by the rule described above), the abscissa has to be the x-axis. Thus, we need to develop an expression for curve $C1_{adj}$ where z is a function of x (i.e., $z(x)$).

From Pollock's method we know that the z-coordinate of a point on curve $C1_{adj}$ is given by,

$$z_e = z_1 + \left(\frac{1}{A_z}\right)[v_{zp}(t_1)\exp(A_z\Delta t_e) - v_{z1}] \quad \textbf{(Eq. 3.97)}$$

where, $v_{zp}(t_1)$ is velocity component of the particle along the z-direction at its starting location; z_e is the z-coordinate of the particle at its exit location; and Δt_e is the particle's exit time, which corresponds to the direction of the particle's shortest travel time.

The starting locations of the particles delineating curve $C1_{adj}$ are along the y-axis at $x = x_1$ and $z = z_1$. Thus, the initial velocity component of the particles in the z-direction, $v_{zp}(t_1)$, is simply v_{z1}. Thus, the expression for z_e can be re-written as,

$$z_e = z_1 + \left(\frac{1}{A_z}\right)[v_{z1}\exp(A_z\Delta t_e) - v_{z1}] \quad \textbf{(Eq. 3.98)}$$

Now, since all the particles for curve $C1_{adj}$ exit through cell face y_1, we know that Δt_e is Δt_{y1}. Thus, Δt_e can be expressed as,

$$\Delta t_e = \Delta t_{y1} = \frac{1}{A_y} \ln\left(\frac{v_{yp}(\Delta t_e)}{v_{yp}(t_1)}\right) \quad \textbf{(Eq. 3.99)}$$

where, A_y is the constant velocity gradient in the y-direction, $v_{yp}(t_e)$ is the component of the particle velocity along the y-direction at its exit location; and $v_{yp}(t_1)$ is velocity component of the particle along the y-direction at its starting location.

Again, since the exit face of the particles is known to be cell face y_1, the velocity component in the y-direction at the exit time, $v_{yp}(\Delta t_e)$, is simply v_{y1}. Thus, Δt_{y1} can be re-written as,

$$\Delta t_{y1} = \frac{1}{A_y} \ln\left(\frac{v_{y1}}{v_{yp}(t_1)}\right) \quad \textbf{(Eq. 3.100)}$$

The starting locations of the particles are constant in the x- and z-directions but variable in the y-direction. Thus, the initial velocity component of the particle in the y-direction, $v_{yp}(t_1)$, is also variable and given by,

$$v_{yp}(t_1) = A_y(y_s - y_1) + v_{y1} \quad \textbf{(Eq. 3.101)}$$

where, y_s is the y-coordinate of the particle starting locations.

Substituting Eq. 3.100 and Eq. 3.101 in Eq. 3.98 yields,

$$z_e = z_1 + \left(\frac{1}{A_z}\right)\left(v_{z1} \exp\left(A_z \frac{1}{A_y} \ln\left(\frac{v_{y1}}{A_y(y_s - y_1) + v_{y1}}\right)\right) - v_{z1}\right) \quad \textbf{(Eq. 3.102)}$$

Eq. 3.102 can now be rearranged to yield an expression for the z-coordinate of the particle exit location, z_e, as a function of the y-coordinate of the particle starting location, y_s, as follows,

$$z_e(y_s) = \left(z_1 - \frac{v_{z1}}{A_z}\right) + \left(\frac{v_{z1}}{A_z}\right)\left(\frac{\frac{v_{y1}}{A_y}}{y_s - \left(y_1 - \frac{v_{y1}}{A_y}\right)}\right)^{\frac{A_z}{A_y}} \quad \textbf{(Eq. 3.103)}$$

To simplify, z_e can be re-written as,

$$z_e(y_s) = a_z + b_z\left(\frac{b_y}{y_s - a_y}\right)^{c_{z,y}} \quad \textbf{(Eq. 3.104)}$$

where, $a_z = z_1 - \frac{v_{z1}}{A_z}$; $b_z = \frac{v_{z1}}{A_z}$; $a_y = y_1 - \frac{v_{y1}}{A_y}$; $b_y = \frac{v_{y1}}{A_y}$; and $c_{z,y} = \frac{A_z}{A_y}$

Repeating the same exercise for the x-coordinate of a point on curve $C1_{adj}$, x_e, yields the following expression for it as a function y_s,

$$x_e(y_s) = a_x + b_x\left(\frac{b_y}{y_s - a_y}\right)^{c_{x,y}} \quad \textbf{(Eq. 3.105)}$$

where, $a_x = x_1 - \frac{v_{x1}}{A_x}$; $b_x = \frac{v_{x1}}{A_x}$; and $c_{x,y} = \frac{A_x}{A_y}$

Now both z_e and x_e, are expressed explicitly as functions of y_s. However, we want z_e to be expressed explicitly as a function of x_e. To do this, we start by expressing y_s as a function of x_e in Eq. 3.105. This yields,

$$y_s(x_e) = a_y + \frac{b_y}{\left(\frac{x_e - a_x}{b_x}\right)^{\frac{1}{c_{x,y}}}} \quad \textbf{(Eq. 3.106)}$$

Substituting Eq. 3.106 in Eq. 3.104 gives,

$$z_e(x_e) = a_z + b_z\left(\frac{x_e - a_x}{b_x}\right)^{c_{zx}} \quad \textbf{(Eq. 3.107)}$$

where, $c = \frac{A_z}{A_x}$

Thus, Eq. 3.107 describes curve $C1_{adj}$ where z_e is explicitly a function of x_e.

If the process is repeated for $C2_{adj}$, it yields,

$$z_e(x_e) = a_z + b_z\left(\frac{x_e - a_x}{b_x}\right)^{c_{zx}} \quad \textbf{(Eq. 3.108)}$$

where, $a_z = z_1 - \frac{v_{z1}}{A_z}$; $b_z = \frac{v_{z2}}{A_z}$; $a_x = x_1 - \frac{v_{x1}}{A_x}$; $b_x = \frac{v_{x1}}{A_x}$; and $c_{zx} = \frac{A_z}{A_x}$

Note, the only difference between the equations describing $C1_{adj}$ and $C2_{adj}$ is in the constant b_z, where for the $C1_{adj}$, $b_z = \frac{v_{z1}}{A_z}$ and for $C2_{adj}$, $b_z = \frac{v_{z2}}{A_z}$.

Now consider outflow face x_2, shown in Figure 3.23(Eq. 3.23. There are also two curves on this outflow face, and since cell face x_2 is an opposite face, we will call the curves $C1_{opp}$ and $C2_{opp}$. Like before, $C1_{opp}$ is the curve representing the boundary of the streamtube emanating from inflow face z_1. It follows, that the ordinate for curve $C1_{opp}$ would be the z-axis and the abscissa would be the y-axis. Thus, this time we need to develop an expression for curve $C1_{opp}$ where z is a function of y (i.e., $z(y)$).

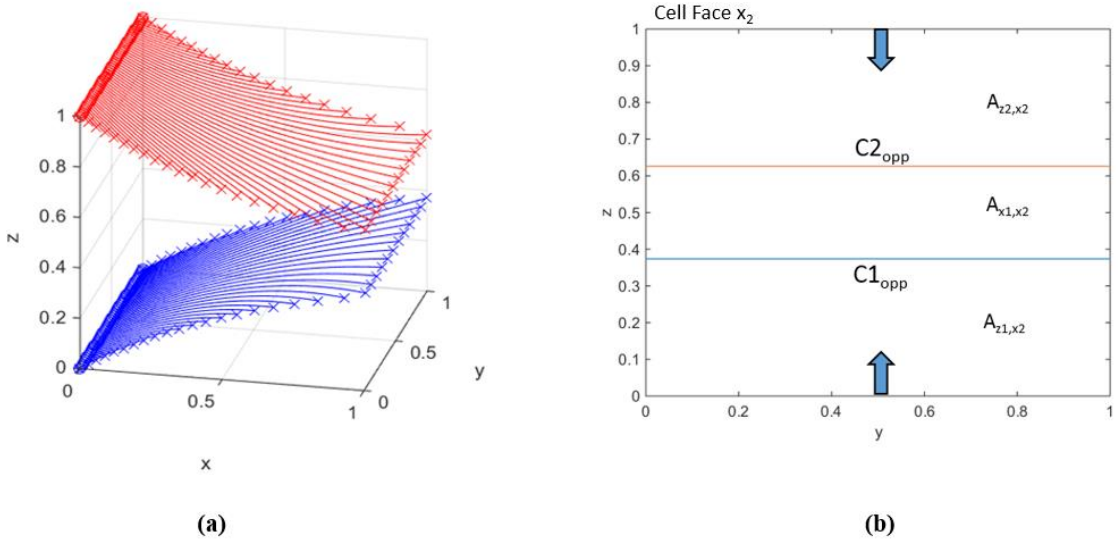

(a) (b)

Figure 3.23 Developing analytically integrable expression for opposite curves: particles forward tracked using Pollock's method from inflow edges for a three inflow-three outflow case (a); and boundaries of dividing stream surfaces (curves) on opposite face (b).

Again, from Pollock's method, we know that the z-coordinate of a point on curve $C1_{opp}$, z_e, is given by,

$$z_e = z_1 + \left(\frac{1}{A_z}\right)[v_{z1}\exp(A_z\Delta t_e) - v_{z1}] \quad \textbf{(Eq. 3.109)}$$

Note, $v_{zp}(t_1)$ is v_{z1} in Eq. 3.109 because the starting locations of the particles delineating curve $C1_{opp}$ are along the y-axis at $x = x_1$ and z = z_1.

For $C1_{opp}$, all the particles exit through cell face x_2. Thus, we know that the shortest Δt_e is Δt_{x2} and consequently the velocity component in the x-direction at its exit time is, $v_{xp}(\Delta t_e)$, is v_{x2}. In addition, since the starting locations of the particles are constant in the x-direction, the initial velocity component of all the particles in the x-direction, $v_{xp}(t_1)$, is simply v_{x1}. Thus, Δt_e can be expressed as,

$$\Delta t_e = \Delta t_{x2} = \frac{1}{A_x}\ln\left(\frac{v_{x2}}{v_{x1}}\right) \quad \textbf{(Eq. 3.110)}$$

Substituting Eq. 3.110 in Eq. 3.109 yields,

$$z_e = z_1 + \left(\frac{1}{A_z}\right)\left[v_{z1}\exp\left(A_z\frac{1}{A_x}\ln\left(\frac{v_{x2}}{v_{x1}}\right)\right) - v_{z1}\right] \quad \textbf{(Eq. 3.111)}$$

Since Eq. 3.111 is completely defined, we can stop here. Eq. 3.111 can now be rearranged to yield an expression for z_e as a function of the y-coordinate of a point on curve $C1_{opp}$, z_e, as follows,

$$z_e(y_e) = \left(z_1 - \frac{v_{z1}}{A_z}\right) + \left(\frac{v_{z1}}{A_z}\right)\left(\frac{v_{x2}}{v_{x1}}\right)^{\frac{A_z}{A_x}} \quad \textbf{(Eq. 3.112)}$$

If the process is repeated for $C1_{opp}$, it yields,

$$z_e(y_e) = \left(z_1 - \frac{v_{z1}}{A_z}\right) + \left(\frac{v_{z2}}{A_z}\right)\left(\frac{v_{x2}}{v_{x1}}\right)^{\frac{A_z}{A_x}} \quad \textbf{(Eq. 3.113)}$$

Note that the curves on the adjacent face, $C1_{adj}$ and $C2_{adj}$, are simple polynomials and the curves on the opposite face, $C1_{opp}$ and $C2_{opp}$, are linear functions with zero-gradients. It turns out that this rule holds for all cases. That is, whenever an edge is tracked to an adjacent cell face, it delineates a curve that is a simple polynomial and whenever an edge is tracked to a non-adjacent cell face (i.e., an opposite face), it delineates a straight line parallel to the edge.

Thus, the general expression for a curve on an adjacent face, $F(X')_{adj}$ is,

$$F(X')_{adj} = a_F + b_F \left(\frac{X' - a_{X'}}{b_{X'}} \right)^{c_{F,X'}} \quad \textbf{(Eq. 3.114)}$$

where, $a_F = F_1 - \frac{v_{F1}}{A_F}$, $b_F = \frac{v_{Fp}(t_1)}{A_F}$, $a_{X'} = {X'}_1 - \frac{v_{X'1}}{A_{X'}}$, $b_{X'} = \frac{v_{X',p}(t_1)}{A_{X'}}$ and, $c_{F,X'} = \frac{A_F}{A_{X'}}$; while the general expression for a curve on an opposite face, $F(X')_{opp}$ is,

$$F(X')_{opp} = \left(F_1 - \frac{v_{F1}}{A_F} \right) + \left(\frac{v_{Fp}(t_1)}{A_F} \right) \left(\frac{v_{X'p}(\Delta t_e)}{v_{X'p}(t_1)} \right)^{\frac{A_F}{A_{X'}}} \quad \textbf{(Eq. 3.115)}$$

In the expressions above, $F(X')$ is the ordinate value, F, for a given location along the abscissa, X' (i.e., if the ordinate for the curve is the z-axis and the abscissa is the z-axis, then $F(X')$ would indicate the z-value at a given x-coordinate or $z(x)$). F_1 indicates coordinate value at the start of the axis in the ordinate direction (i.e., if the ordinate for the curve is the z-axis, F_1 would be $z = z_1$). Similarly, v_{F1} indicates the cell flow velocity component at the start of the axis in the ordinate direction (i.e., if the ordinate for the curve is the z-axis, v_{F1} would be v_{z1}) and A_F indicates the velocity gradient component in the ordinate direction (i.e., if the ordinate for the curve is the z-axis, A_F would be A_z). $v_{F_p}(t_1)$ indicates the velocity component of the particle in the ordinate direction at its starting location (i.e., if the ordinate for the curve is the z-axis, $v_{F_p}(t_1)$ would be $v_{z_p}(t_1)$).

Analogous definitions hold for the terms associated with the abscissa direction. That is, X'_1 indicates coordinate value at the start of the axis in the abscissa direction, $v_{X'1}$ indicates the flow velocity component at the start of the axis in the abscissa direction, $A_{X'}$ indicates the velocity gradient component in the abscissa direction, $v_{X'_p}(t_1)$ indicates the velocity component of the particle in the abscissa direction at its starting location, and $v_{X'_p}(\Delta t_e)$ indicates the velocity component of the particle in abscissa direction at its exit location.

Now that the expressions for the curves have been obtained, the next step is to define the limits of each curve. The limits of the curve, $X'_{lim,1}$ and $X'_{lim,2}$, are the coordinates along the X' axis of the exit locations of the particles bounding $F(X')$.

To illustrate how the limits of a curve are determined, consider again curve $C1_{adj}$ shown in Figure 3.22. Eq. 3.105 allows for the x-coordinate of a point on curve $C1_{adj}$, x_e, to be determined for a given y-coordinate of the particle starting location, y_s. In generic terms, this can be expressed as,

$$X'(s) = a_{X'} + b_{X'}\left(\frac{b_e}{s - a_e}\right)^{c_{X',e}} \quad \textbf{(Eq. 3.116)}$$

where, $a_{X'} = X'_1 - \frac{v_{X'1}}{A_{X'}}$; $b_{X'} = \frac{v_{X'p(t_1)}}{A_{X'}}$; $a_e = s_1 - \frac{v_{e,1}}{A_e}$; $b_e = \frac{v_{e,p}(\Delta t_e)}{A_e}$ and; $c_{X',e} = \frac{A_{X'}}{A_e}$.

In the expressions above, X'_1, $v_{X'1}$, $v_{X'_p}(t_1)$, and $A_{X'}$ retain the same definitions as before. s indicates the location of the particle along the release edge (i.e., if the edge is between $y = y_1$ and $y = y_2$, then s is the y-coordinate of the particle starting location, whereas if the edge is between $x = x_1$ and $x = x_2$, then s is the x-coordinate of the particle starting location). $v_{e_p}(\Delta t_e)$ indicates the particle velocity component in the exit direction at its exit location (i.e., if the particle exits through cell face y_1, then $v_{e_p}(\Delta t_e)$, would be $v_{y_p}(\Delta t_e)$, whereas if it exits

through cell face x_2, $v_{e_p}(\Delta t_e)$ would be $v_{x_p}(\Delta t_e)$). Similarly, A_e indicates the velocity gradient component in the particle exit direction (i.e., if the particle exits through cell face y_1 or y_2, then A_e would be A_y) and $v_{e,1}$ indicates the cell flow velocity component at the start of the axis in the exit direction (i.e., if the particle exits through cell face y_1 or y_2, then $v_{e,1}$ would be v_{y1}, whereas if it exits through cell face x_1 or x_2, $v_{e,1}$ would be v_{x1}). Lastly, s_1 indicates the coordinate value at the start of the axis along the release edge (i.e., if the edge is between $y = y_1$ and $y = y_2$, then s_1 would by y_1, whereas if the edge is between $x = x_1$ and $x = x_2$, then s_1 would be x_1). Note, the direction of the changing variable of the release edge (i.e., the s-direction) and the exit direction of the particle will always be the same for adjacent curves.

Now, let us repeat the process for curve $C1_{opp}$ shown in Figure 3.23. Since opposite curves are linear functions with zero-gradients, we were able to derive an explicit expression for z_e as a function of y_e without needing to first derive an expression for y_e as a function of y_s. If we were to do this now, then applying all the necessary substitutions, it would yield,

$$y_e(y_s) = \left(y_1 - \frac{v_{y1}}{A_y}\right) + \left(y_s - \left(y_1 - \frac{v_{y1}}{A_y}\right)\right)\left(\frac{v_{x2}}{v_{x1}}\right)^{\frac{A_y}{A_x}} \quad \textbf{(Eq. 3.117)}$$

In generic terms, this can be expressed as,

$$X'(s) = a_{X\prime} + (s - a_{X\prime})a_e{}^{b_{X',e}} \quad \textbf{(Eq. 3.118)}$$

where, $a_{X\prime} = X'_1 - \frac{v_{X\prime 1}}{A_{X\prime}}$; $a_e = \frac{v_{e,p}(\Delta t_e)}{v_{e,p}(t_1)}$ and; $b_{X',e} = \frac{A_{X'}}{A_e}$

Again, in the expressions above, X'_1, $v_{X\prime 1}$, $A_{X\prime}$, $v_{e_p}(\Delta t_e)$, and A_e all retain their previous definitions. $v_{e_p}(t_1)$ indicates the particle velocity component in the exit direction at its starting location (i.e., if the particle exits through cell face y_1 or y_2, then $v_{e_p}(t_1)$, would be $v_{y_p}(t_1)$, whereas if it exits through cell face x_2 or x_2, then $v_{e_p}(t_1)$, would be $v_{x_p}(t_1)$).

Thus, provided that the release locations of the bounding particles are known, Eq. 3.116 and Eq. 3.118 can be used to determine the limits of any curves on an adjacent face and opposite face respectively. Careful observation revealed that there are three conditions that can arise with regards to the release locations of the bounding particles: (1) both bounding particles are corners, (2) one bounding particle is a corner, and, (3) no bounding particles are corners. To illustrate, consider the case shown in Figure 3.24.

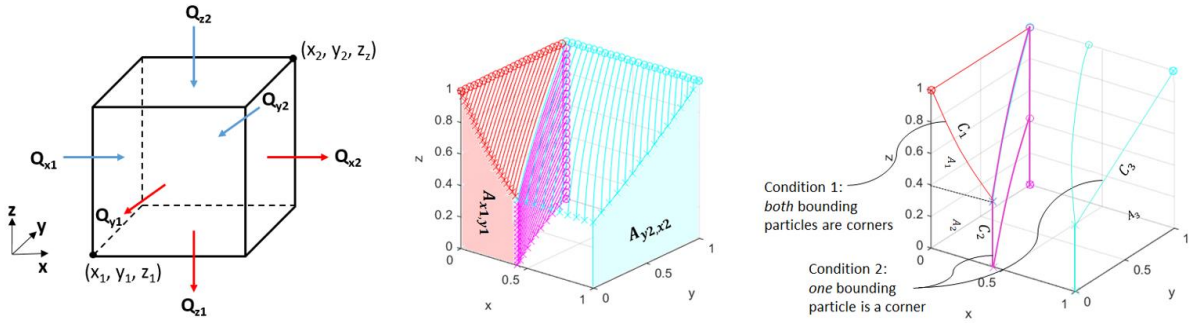

Figure 3.24. Determining limits of flow connection area curves as per conditions 1 and 2: schematic of cell face flow configuration (a); $A_{x1,y1}$ is the flow connection area delineated on cell face y_1 by the streamtube emanating from cell face x_1 and $A_{y2,x2}$ is the flow connection area delineated on cell face x_2 by the streamtube emanating from cell face y_2 (b); A_1, A_2, and A_3 are the areas under curves C_1, C_2, and C_3 respectively; curve C_1 is bounded by the exit locations of the corners of the inflow edge along y-axis at $z = 1$ and as such, both its limits are easily determined from the locations of the corners; curves C_2 and C_3 both have one bounding particle that is a corner and the corresponding limit can be directly obtained from the location of the corner, however to obtain the other limit (that is not a corner) additional steps are required (c).

The streamtube geometry has been recreated by forward tracking particles from the inflow edges for visualization in Figure 3.24 (b). $A_{x1,y1}$ is the flow connection area delineated on cell face y_1 by the streamtube emanating from cell face x_1 and $A_{y2,x2}$ is the flow connection area delineated on cell face x_2 by the streamtube emanating from cell face y_2. Note $A_{x1,y1}$ is delineated by an adjacent curve, C_1 (i.e., by exit locations of inflow edge along the y-axis at $z = 1$) and an opposite curve, C_2 (i.e., by exit locations of inflow edge along the z-axis at $y = 1$), while $A_{y2,x2}$ by a single adjacent curve, C_3 (i.e., by exit locations of inflow edge along the x-axis

at $z = 1$). Thus, $A_{x1,y1}$ is the sum of the areas under curves C_1 and C_2 (i.e., the sum of A_1 and A_2) and $A_{y2,x2}$ is simply the area under C_3 (i.e., it is equal to A_3).

For C_1, note in Figure 3.24 (c) that both the bounding particles are the corners of the tracked edge (i.e., condition 1). Since the locations of all the corners are known apriori, whenever this condition exists, the relevant coordinates of the corners can be inputted into either of Eq. 3.116 or Eq. 3.118 to yield the appropriate limits of the curve. For C_2, note in Figure 3.24 (c) that one of the corners of the tracked edge is a bounding particle of the curve (i.e., condition 2) but the other corner is not. Let us define the first bounding particle as the 'bounding corner', and the latter as the 'non-bounding corner'. Now, the limit associated with the bounding corner can be determined directly as described by the procedure for the condition when both bounding particles are corners (i.e., condition 1). The procedure to determine the limit associated with the non-bounding corner depends on whether the limit is on an opposite or an adjacent curve. Since opposite curves are parallel to the tracked edge, the limits of the curve are parallel to the corners. Thus, if the non-bounding corner is at start of the axis, then the associated limit will also be at the start of the axis, whereas if the non-bounding corner is at the end of the axis, so will be the limit. It turns out that adjacent curves which have only one bounding particle as a corner always extend to the edges of the outflow face as shown by C_3 in Figure 3.24 (c). The bounding corner always defines one limit, which is at one edge of the outflow face, and thus the limit associated with the non-bounding corner has to be at the other edge.

Lastly, to illustrate the third condition, consider again the case shown in Figure 3.25. Like before, the streamtube geometry has been recreated for visualization Figure 3.25 (b) and the flow connection area delineated on cell face x_1 by the streamtube emanating from cell face x_2, $A_{x2,x1}$, is shown. Figure 3.25 (c) shows that $A_{x2,x1}$ is delineated by two opposite curves, none of which

have any bounding particles that are corners. Note that both curves extend to the edges of the outflow face.

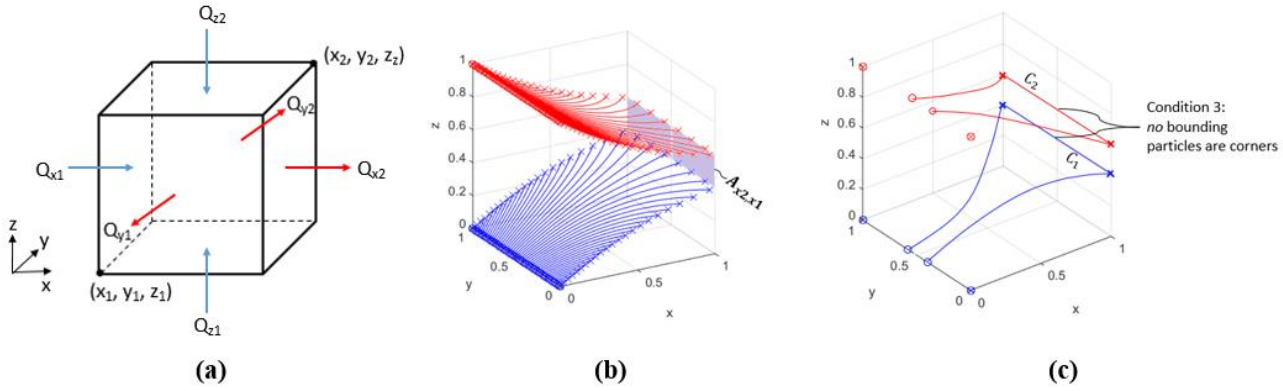

Figure 3.25. Determining limits of flow connection area curves as per condition 3: schematic of cell face flow configuration (a); $A_{x2,x1}$ is the flow connection area delineated on cell face x_1 by the streamtube emanating from cell face x_2 (b); none of the bounding particles of curves C_1 and C_2 are bounded by corners; when this condition exists, the curve always extends to the edges of the outflow face and thus the limits are determined as the edges of the outflow face that the curve lies on (c).

It turns out that whenever the third condition exists, the curve always extends to the edges of the outflow face. Thus for these curves, the release locations of the bounding particles need not be known and the limits are simply assigned to be at start and end of the X' axis (i.e., if the X' axis is the x-axis then the limits will be at $x = x_1$ and $x = x_2$).

Now it is possible to express Eq. 3.114 (i.e., adjacent curve function) and Eq. 3.115 (i.e., opposite curve function) as definite integrals with limits ${X'}_{lim,1}$ and ${X'}_{lim,2}$ and analytically evaluate those integrals to yield expressions for the flow connection areas.

Thus, the flow connection areas under a curve on an adjacent face, A_{adj}, and under a curve on an opposite face, A_{opp}, can be evaluated as,

$$A_{adj} = a_F(X'_{lim,2} - X'_{lim,1}) + \frac{b_F b_{X'}}{c_{F,X'} + 1}\left(\left(\frac{X'_{lim,2} - a_{X'}}{b_{X'}}\right)^{c_{F,X'}+1} - \left(\frac{X'_{lim,1} - a_{X'}}{b_{X'}}\right)^{c_{F,X'}+1}\right) \quad \textbf{(Eq. 3.119)}$$

$$A_{opp} = \left(\left(F_1 - \frac{v_{F1}}{A_F}\right) + \left(\frac{v_{Fp}(t_1)}{A_F}\right)\left(\frac{v_{X'p}(t_e)}{v_{X'p}(t_1)}\right)^{\frac{A_F}{A_{X'}}}\right)(X'_{lim,2} - X'_{lim,1}) \quad \textbf{(Eq. 3.120)}$$

where, $X'_{lim,1}$ and $X'_{lim,2}$ are the limits calculated using Eq. 3.116 and Eq. 3.118 depending on the limit conditions that exist (i.e., both bounding particles are corners, one bounding particle is a corner, or no bounding particles are corners) and whether the curve is an on an adjacent or an opposite face.

An important point to add is that in developing the general expressions for the areas under curves on adjacent and opposite faces, we made the implicit assumption of non-zero velocity gradients. However, that may not always be the case. So, if a zero-velocity gradient does exist in any of the principal directions, it must be converted into a non-zero velocity gradient to permit the use of Eq. 3.119 and Eq. 3.120 as is. Thus, before any areas are evaluated, it is necessary to first check for zero-velocity gradients. If a zero-velocity gradient is found to exist in a particular direction, a low magnitude flow is routed through that direction to convert it into a negligible non-zero velocity gradient. Eq. 3.119 and Eq. 3.120 can then be used as is to determine the flow connection areas. The magnitude of flow correction should not be so large so as to induce errors in the flow calculations but at the same time it must be large enough (i.e., not approaching the limit of zero) to permit the use of the equations.

3.4.6 Summary of Algorithm

The routines for determining volumetric flow connections in a three-dimensional cell can be embedded in an algorithm similar to the 2D-algorithm. The first few steps are exactly the

same – first the FCM matrix is initialized and then the cell face flows have to be obtained from a flow model. Next the algorithm checks for each of the special conditions in the following order: (1) trivial case, (2) single inflow and/or single outflow, (3) stagnation point inside cell, and (4) compatible with 2D-algorithm and applies the appropriate mass balance based routines if any of those conditions exist. If a case does not get flagged by any of the special conditions, the volumetric flow connections have to be determined by analytically recreating the internal streamtube geometry. Finally, once the volumetric flow connections through all the hydraulically connected faces have been determined, the remaining elements of the FCM matrix are populated. A flowchart of the general algorithm is presented in Figure 3.26.

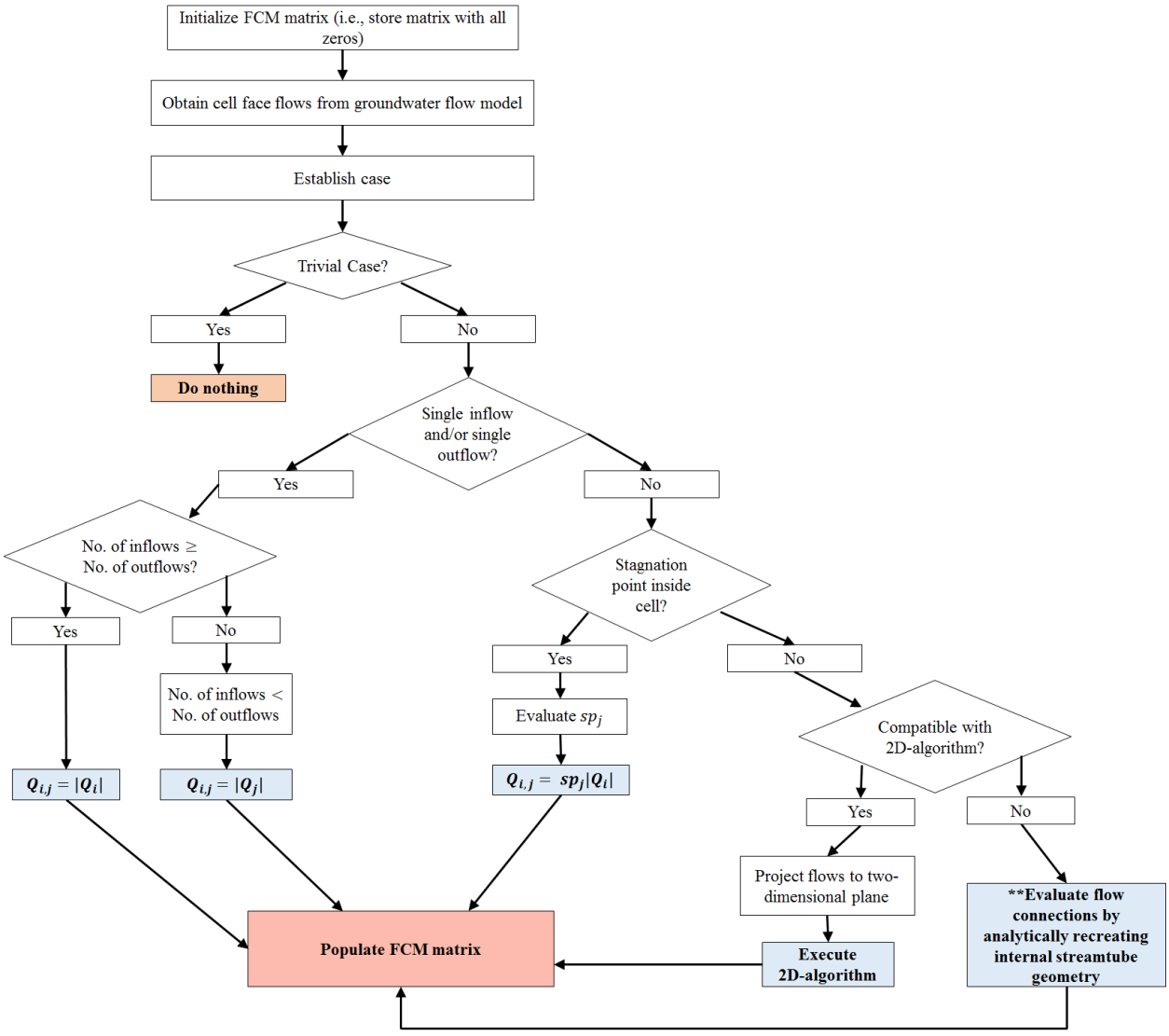

Figure 3.26. Flow chart of algorithm for computing volumetric flow connections in a three-dimensional rectilinear finite-difference cell; the blue boxes indicate the equations used for determining flow connections; the red boxes indicate terminal points in the flow chart.

Since determining volumetric flow connections for all non-special cases (i.e., streamtube recreation cases) in a three-dimensional cell is quite involved, a flowchart of the algorithm pertaining exclusively to that routine is presented in Figure 3.27.

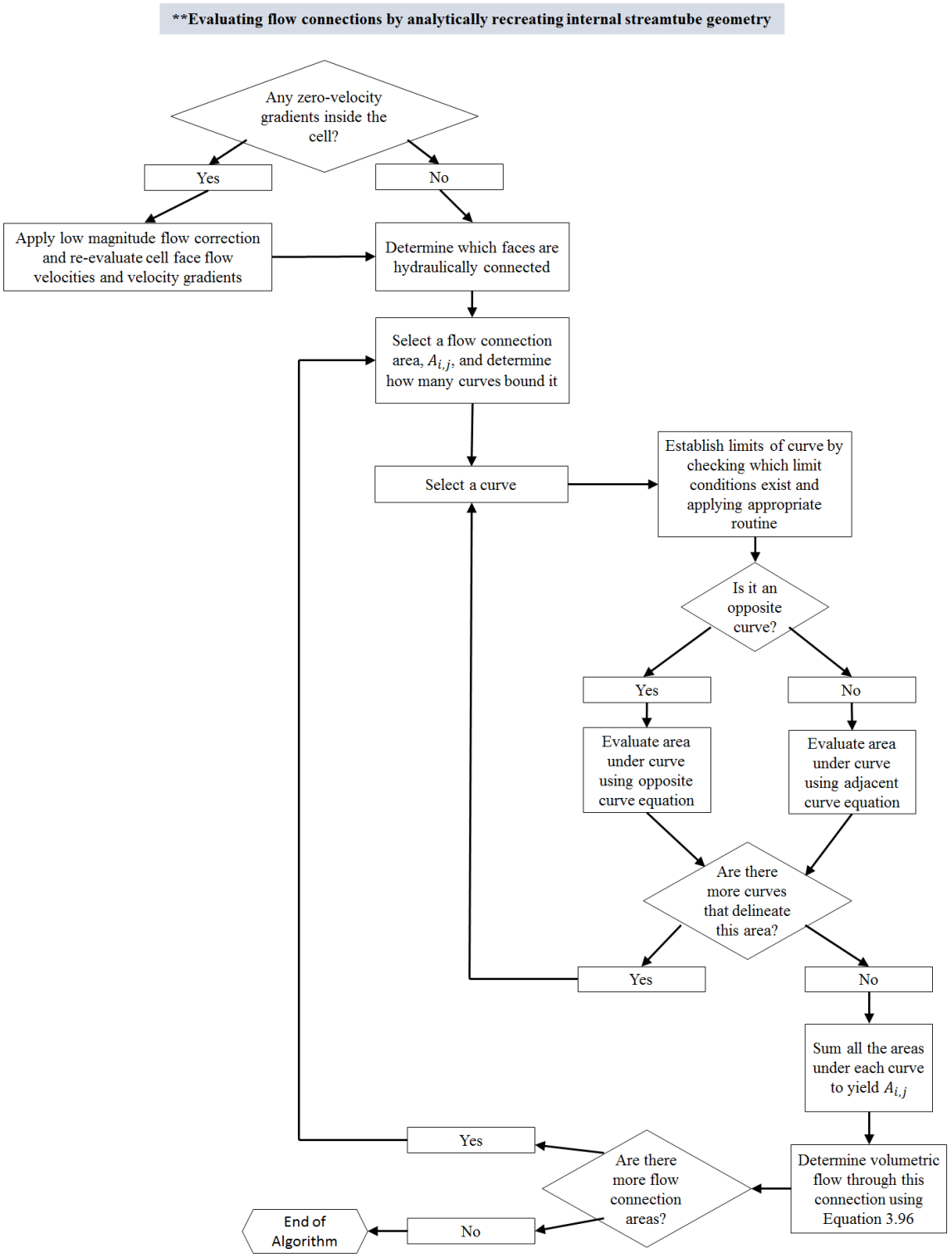

Figure 3.27. Flowchart of algorithm for determining volumetric flow connections by analytically recreating internal streamtube geometry.

The algorithm described in Figure 3.26 would be implemented in FlowSource (Black and Foley, 2013) on a cell-by-cell basis as a preceding step to its volumetric flow calculations. So, for each cell, the flow configuration (i.e., the cell face flows) would be first read from the cell-by-cell flows outputted by the flow model. Next, the corresponding flow connections inside the cell would be established using the algorithm. The connections would then be fed into FlowSource for its volumetric flow calculations. Since, numerical dispersion in FlowSource is primarily an issue when using coarse grids, the algorithm should perhaps be incorporated as an "on/off" switch. This would enable FlowSource to retain its computational efficiency by having the option to revert back to the fully mixed assumption when using finer grids and only use the algorithm when its calculations show signs of significant numerical dispersion. Note, the actual incorporation of the algorithm into FlowSource is beyond the scope of this thesis.

3.4.7 Sources of Errors

Since the algorithm is based on Pollock's semi-analytical particle tracking method, it is subject to the same sources of errors present in Pollock's method, and particle tracking methods in general. Some of these were highlighted in Section 2.2.3. Though addressing sources of errors inherent in particle tracking methods is beyond the scope of this thesis, an important one to note particularly with regards to this algorithm is the potential presence of a weak well inside a cell (i.e., a well not strong enough to induce all cell face flows inwards). Generally, the problem with particle tracking methods that use the simple linear velocity interpolation scheme like in Pollock's method is that they fail to capture the fact that the velocities should increase as it gets closer to the well (Zheng, 1994). For strong wells this is not a problem, since for those cases there are no volumetric flow connections to be calculated (i.e., it is a trivial case). However, for weak wells the problem is more than just inaccurately representing the velocity field inside the

cell. The algorithm breaks down because it assumes that there is no internal removal of water inside the cell. The same holds for when there is a weak source inside the cell (i.e., a source not strong enough to induce all cell face flows outwards), since the assumption is that there is no internal addition of water either. In these cases, it is suggested that the algorithm not be used and the fully mixed assumption is re-invoked.

The only source of error introduced by the algorithm itself is in its requirement of non-zero velocity gradients inside the cell. For cases where there are zero-velocity gradients inside the cell, the magnitude of the flow correction can affect the accuracy of the calculations. The non-zero velocity gradient assumption is used for the cases that require the recreation of their internal streamtube geometry. These include the majority of cases with five or more non-zero cell face flows and all cases with four non-zero flows that have non-planar flow. For these cases, it is possible to have zero-velocity gradients either in all three directions or in only one direction. The latter is due to the assumption of no internal addition or removal of water. Some of these cases are illustrated in Figure 3.28. The error in the calculations can be obtained from the flow connection matrix (FCM). The FCM matrix is a six-by-six square matrix containing all the volumetric flow connections. Each element in the FCM matrix represents the flow from cell face i to cell face j and the sum of each row represents the cell face flows as computed from the volumetric flow connections obtained from the algorithm. Hence, the total percentage error in the calculation of the algorithm for a single run can be obtained by,

$$total\ \%\ error = \sum_{k=1}^{6} \frac{\left|Q_{k,a} - Q_{k,FCM}\right|}{\left|Q_{k,a}\right|} \cdot 100 \qquad \textbf{(Eq. 3.121)}$$

where, Q_k is the flow through cell face k; $Q_{k,a}$ is the assigned flow through cell face k; and $Q_{k,FCM}$ is the flow through cell face k as calculated from the FCM matrix.

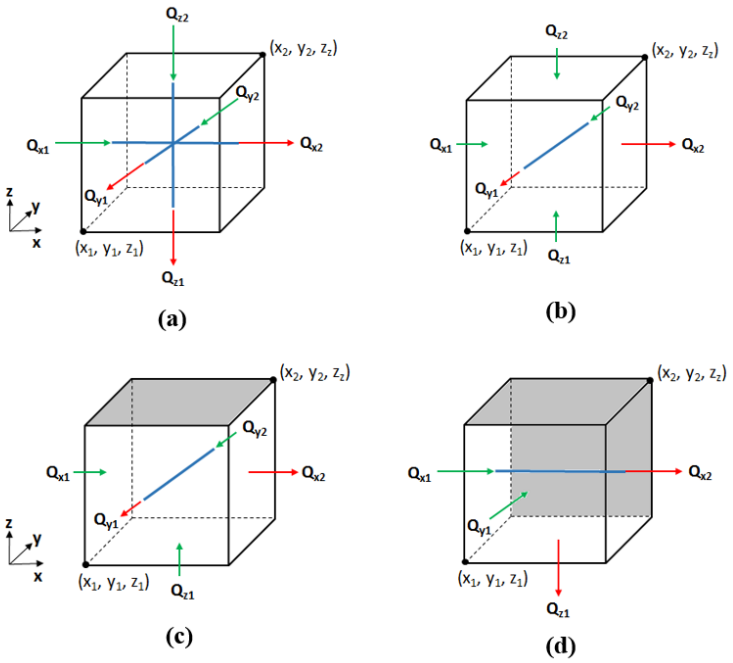

Figure 3.28. Examples of cases with zero-velocity gradients inside cell: six non-zero flow case with zero-velocity gradients in all three directions ($Q_{x1} = Q_{x2}$, $Q_{y1} = Q_{y2}$, and $Q_{z1} = Q_{z2}$) (a); six non-zero flow case with zero-velocity gradient in y-direction ($Q_{x1} \neq Q_{x2}$, $Q_{y1} = Q_{y2}$, and $Q_{z1} = -Q_{z2}$) (b); five non-zero flow case with zero-velocity gradient in y-direction ($Q_{x1} \neq Q_{x2}$, $Q_{y1} = Q_{y2}$, and $Q_{z1} \neq Q_{z2}$) (c); and four non-zero flow case with zero-velocity gradient in x-direction ($Q_{x1} = Q_{x2}$, $Q_{y1} \neq Q_{y2}$, and $Q_{z1} \neq Q_{z2}$) (d).

A graph illustrating the sensitivity of flow calculations to the magnitude of flow correction is shown in Figure 3.29 for the three zero-velocity gradient case from Figure 3.28 (a) and one zero-velocity gradient case from Figure 3.28 (b). The graph shows that there is a range for the magnitude of flow correction within which the algorithm can produce accurate results for the three zero-velocity gradient case (i.e., between 0.1% and 0.01%). Obviously, if the flow correction magnitude is too large (i.e., 10%) then it induces significant errors in the flow calculations (i.e., 40%), whereas if it is too small (i.e., less than 0.01%) then it also produces erroneous results. The latter is due to the fact that as the magnitude of the flow correction approaches zero the rounding errors in MATLAB become more significant (i.e., it is actually a problem with not being able to store fractional numbers exactly using a finite number of digits as opposed to a problem with the method itself). However, as illustrated in the graph, for the cases

with a zero-velocity gradient in only one direction, as the magnitude of the flow correction approaches zero, so does the error in the calculations. It was found that using a flow correction magnitude of 0.009% yields stable results for all the zero-velocity gradient cases.

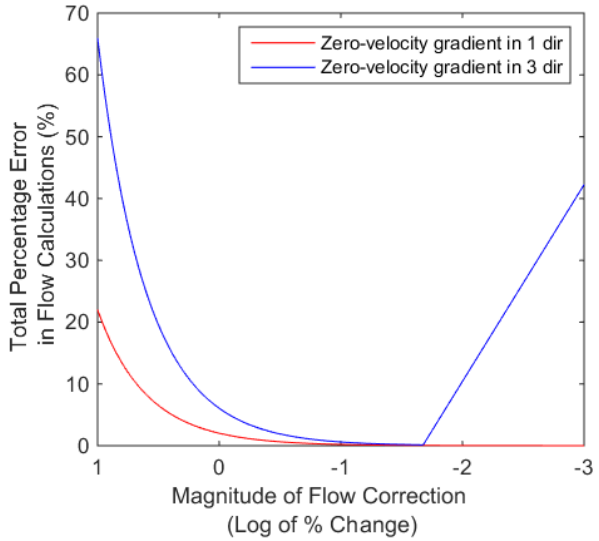

Figure 3.29. Graph illustrating the sensitivity in the accuracy of flow calculations to the magnitude of flow correction for the cases shown in Figure 3.28 (a) and (b). The *x*-axis is the log of the percentage the assigned flows were changed by to induce a non-zero velocity gradient. The graph shows that the algorithm can produce erroneous results if the magnitude of flow correction is too large or too small for cases when there are zero-velocity gradients in all three coordinate directions.

3.5 Determining connectivity of wells and surface-water features

A tool was developed which can be used to determine the volume of water in a groundwater withdrawal well that is sourced from model cells that make up a surface-water feature (or any other feature of interest on the land surface) and map how the location of a well affects the volume of water captured from these cells. The maps can be used to demonstrate how pumping parameters (i.e., pumping rates and pumping time), changes in areal recharge, and/or addition of new wells can affect a well's volumetric capture from the cells that make up the feature of interest. The tool is based on FlowSource (Black and Foley, 2013) and the mapping utility of the tool employs a principle similar to that of the LRD method (Leake et al., 2010), which was presented in Section 2.3.2. The tool was developed in MATLAB.

3.5.1 Determining Volumetric Contribution from Features of Interest

The first utility of the tool is essentially a simple application of FlowSource to issues of groundwater surface-water interactions. FlowSource can determine the volume of water that passed through or originated in a model cell that is ultimately captured at a user-defined 'destination' cell. A MATLAB computer program was developed that takes the location of wells and feature(s) of interest as inputs and outputs the volumetric contribution of the feature(s) of interest to the wells using FlowSource.

In the input file of the computer program, the model cells that contain the well(s) ('destination' cells) and the model cells that make up the feature(s) of interest ('source' cells) are specified. Though multiple features of interest can be specified, all the features have to be contained entirely within the same layer (i.e., they cannot span multiple layers). Since the intention is to determine the volume of water sourced from surface-water features, which typically lie in the top model layer, this is not a requirement that would significantly compromise the utility of the tool. Also note, that when multiple destination cells are specified in FlowSource, it treats them all as one collective 'destination' (i.e., it computes the volume of water that is ultimately extracted at all the destination cells). However, for the purposes of this thesis, the goal is to examine the volume of water each well sources from a user-specified feature(s) interest. As such, unique FlowSource runs are required for each well.

Thus, the computer program reads the locations of the wells and feature(s) of interest from the input file. Next, it writes the location of the first well to the FlowSource input file as the sole destination cell and runs FlowSource for the desired metrics (i.e., volume-through, fraction-through, volume-from, and fraction-from). Then, for each feature of interest, it computes the sum of the metrics from all the model cells that make up that feature of interest. For each metric, this

represents the total contribution from the feature of interest to the specified well. These steps are repeated until the desired metrics have been obtained for each individual well.

3.5.2 Incorporation of Mapping Capabilities

The computer program described in Section 3.5.1 was augmented further to incorporate mapping capabilities. The steps involved in generating the maps are quite simple. As in the LRD method, first a MODFLOW (Harbaugh et al., 2000) model is run without any added withdrawals to establish the 'pre-development', or baseline head distribution. Next, the MODFLOW model is re-run, the only differences being that a withdrawal well is added in one model cell and the baseline head distribution is used as the initial head distribution for the run with the well. Then the relevant MODFLOW output files (i.e., the cell-by-cell budget or CBB file, the head distribution or HDS file, and the discretization or DIS file) from this run are used as inputs for FlowSource. FlowSource is run to establish the desired FlowSource metrics for the simulation with the added well. Then, like in Section 3.5.1, the metrics from all the model cells that make up the specified feature of interest are summed to get the total contribution from that feature of interest to the well and this value is assigned to the cell containing the well. This process is repeated for as many model cells until the desired resolution is reached. Thus, a contour map may be generated for each feature of interest, where each point, or model cell, represents the volume of water a well with the user-specified parameters would source from that feature of interest at the specified time if the well were located at that point or model cell. Figure 3.30 illustrates the steps involved in generating the maps.

Two other capabilities were added to examine the impact of pumping on existing wells and the flows at the interface of surface-water and groundwater, i.e., the hyporheic zone (Boulton et al., 1998). The two added utilities are essentially making use of the versatility of FlowSource. In

the first case, the base MODFLOW model is run as before and but then the output files from the base simulation are used to run FlowSource where an existing well in the model is specified as the destination cell. The total contribution from the feature(s) of interest to that existing well is then calculated and stored. Next, a new well is added in one model cell and the MODFLOW model is re-run using the head distribution from the base simulation as the initial head distribution. Then, FlowSource is run and the total contribution from the feature(s) of interest to the existing well is calculated again. The difference between the base contribution and the contribution from the simulation with the added well is computed and assigned to the location of the added well. This shows the change in the volume of water sourced from the feature(s) of interest in the existing well as a result of the addition of the new well. Again, this is done for as many cells until desired resolution is reached, which then allows a contour map to be generated showing the spatial distribution of the impact on the volumetric composition of existing wells as a result of adding a new well with the user-specified parameters.

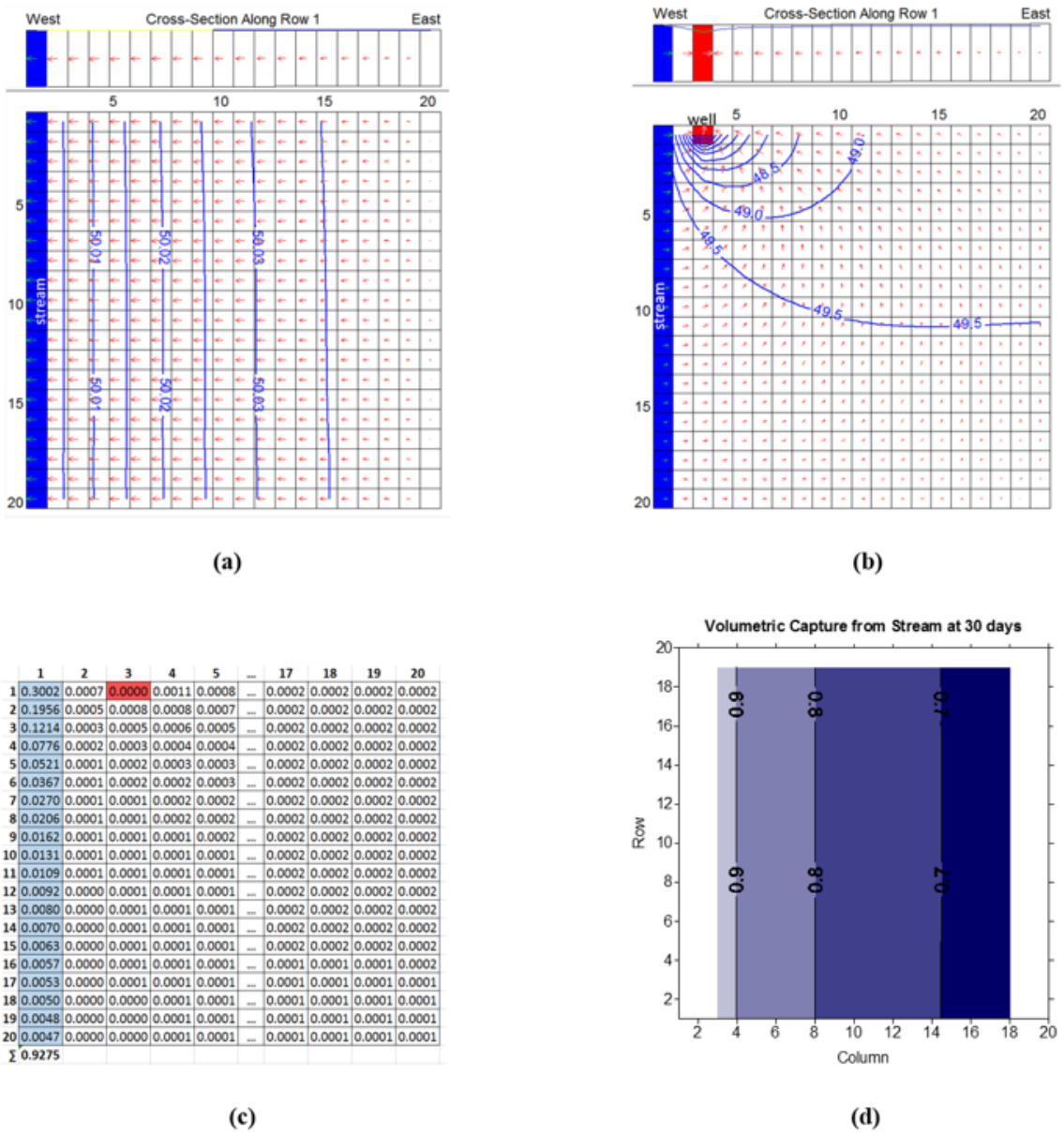

	1	2	3	4	5	...	17	18	19	20
1	0.3002	0.0007	0.0000	0.0011	0.0008	...	0.0002	0.0002	0.0002	0.0002
2	0.1956	0.0005	0.0008	0.0008	0.0007	...	0.0002	0.0002	0.0002	0.0002
3	0.1214	0.0003	0.0005	0.0006	0.0005	...	0.0002	0.0002	0.0002	0.0002
4	0.0776	0.0002	0.0003	0.0004	0.0004	...	0.0002	0.0002	0.0002	0.0002
5	0.0521	0.0001	0.0002	0.0003	0.0003	...	0.0002	0.0002	0.0002	0.0002
6	0.0367	0.0001	0.0002	0.0002	0.0003	...	0.0002	0.0002	0.0002	0.0002
7	0.0270	0.0001	0.0001	0.0002	0.0002	...	0.0002	0.0002	0.0002	0.0002
8	0.0206	0.0001	0.0001	0.0002	0.0002	...	0.0002	0.0002	0.0002	0.0002
9	0.0162	0.0001	0.0001	0.0001	0.0002	...	0.0002	0.0002	0.0002	0.0002
10	0.0131	0.0001	0.0001	0.0001	0.0001	...	0.0002	0.0002	0.0002	0.0002
11	0.0109	0.0001	0.0001	0.0001	0.0001	...	0.0002	0.0002	0.0002	0.0002
12	0.0092	0.0000	0.0001	0.0001	0.0001	...	0.0002	0.0002	0.0002	0.0002
13	0.0080	0.0000	0.0001	0.0001	0.0001	...	0.0002	0.0002	0.0002	0.0002
14	0.0070	0.0000	0.0001	0.0001	0.0001	...	0.0002	0.0002	0.0002	0.0002
15	0.0063	0.0000	0.0001	0.0001	0.0001	...	0.0002	0.0002	0.0002	0.0002
16	0.0057	0.0000	0.0001	0.0001	0.0001	...	0.0001	0.0001	0.0001	0.0002
17	0.0053	0.0000	0.0001	0.0001	0.0001	...	0.0001	0.0001	0.0001	0.0001
18	0.0050	0.0000	0.0000	0.0001	0.0001	...	0.0001	0.0001	0.0001	0.0001
19	0.0048	0.0000	0.0000	0.0001	0.0001	...	0.0001	0.0001	0.0001	0.0001
20	0.0047	0.0000	0.0000	0.0001	0.0001	...	0.0001	0.0001	0.0001	0.0001
Σ	0.9275									

Figure 3.30. Steps to generate a contour map: a 30 row x 30 col x 1 layer MODFLOW base model with a stream on the west end is run (a); the MODFLOW model is re-run for 30 days using the final head distribution from the base run as the initial head distribution and with a pump added in cell (1, 1, 3) (b); FlowSource fraction-from values are then calculated for the model with the well; the destination cell is set as the location of the added well highlighted in red and the fraction-from values are summed for the stream, which is the feature of interest (c); steps in (b) and (c) are repeated with well locations considered in every second row and second column and then a contour map is generated showing the 'volumetric capture' from the stream at 30 days (d).

Note for this routine, the destination cell in FlowSource always remains the same (i.e., it is the location of the existing well being examined), while in the previous routine the destination cell is moving with location of the added wells. This same concept applied for the second added

mapping capability. This time, instead of specifying an existing well as a destination cell, a group of destination cells are specified and the change in the desired FlowSource metrics from the feature(s) of interest to those destination cell is computed in each run (i.e., a well is added to a model cell and MODFLOW is re-run and the change in FlowSource metrics is computed after running FlowSource and this is repeated until the desired resolution is reached). Again, a contour map can be generated but this time it depicts the spatial distribution of the impact of flow between features of interest as a result of adding a new well with the user-specified parameters.

While the mechanics of the computer program are quite simple and easily explained as a series of steps, the development of the program to include the mapping capabilities required considerable effort. This is mainly because to generate the maps, the MODFLOW input files have to be re-written, some for every run and some only once, and it was attempted to keep the re-writing procedure reasonably generic. Thus, the computer program can handle several relevant changes made to the base MODFLOW model. For example, the areal recharge and evapotranspiration of the base model can be modified as desired (i.e., added, removed, or changed) and it is possible to add wells with time-varying pumping rates (i.e., specify multiple stress periods). Aquifer parameters (i.e., storage, porosity, and hydraulic conductivity zones) can also be changed if desired. Furthermore, the base MODFLOW model can be steady-state or transient model. Note, the FlowSource input file also has to be re-written for every run, however it was not nearly as involved as developing the program to be able to re-write the MODFLOW input files.

Chapter 4

Results and Discussion

4.1 Application of Algorithm to Compute Volumetric Flow Connections in a Three-Dimensional Rectilinear Cell

The application of each of the different routines in the algorithm is shown for single cell test cases. At the time of writing this thesis, the algorithm had not yet been incorporated into FlowSource (Black and Foley, 2013) and as such, the potential reduction in numerical dispersion from incorporation of the algorithm is shown for a hypothetical case.

4.1.1 Single Cell Test Cases

The algorithm has a separate routine to handle each of the four types of non-trivial cases, which include: ‘single inflow and/or single outflow’, ‘stagnation point inside the cell’, ‘compatible with 2D-algorithm’, and all other cases (or general cases). Note, the trivial cases are not mentioned because for those cases volumetric flow connections need not be calculated. The first three routines are for the special cases and they simply apply mass balance inside the cell. As a result, those routines are quicker than the one required for the general cases, which analytically recreates the internal streamtube geometry. Moreover, since the volumetric flow connections for special cases are calculated using mass balance, those routines yield exact results, assuming of course that there is no internal removal or addition of water. Exact results can also be obtained for nearly all the general cases. The only problem arises with general cases with zero-velocity gradients inside the cell, since a low magnitude flow correction has to be applied for them. Even then, near exact answers can be obtained provided the magnitude of the flow correction is chosen appropriately.

Note, all results were generated with an unoptimized code on a Microsoft® Windows 7 computer with an Intel® Core ™ i7 2.7 GHz processor. Also, the internal streamtube geometry has been recreated by numerical particle tracking for each case for visualization.

Table 4.1 shows the results for a single inflow case, a stagnation point case, and a 2D-algorithm compatible case. The calculations for these cases are exact and they typically take less than 0.01 seconds to complete. The table shows the maximum time taken from a 1000 runs to provide a conservative estimate. However, the average run time from a 1000 runs for each of the special cases was less than 0.001 seconds.

Table 4.2 shows the results for three general cases (streamtube recreation cases), which are all handled by the same routine. These cases represent the vast majority of cells typically encountered in a groundwater flow model. Since for the cases shown, there are no zero-velocity gradients inside the cells, the calculations are exact. The maximum time taken to complete from a 1000 runs for these cases is typically less than 0.15 seconds. Again, this is a conservative estimate. The average time take taken to complete from a 1000 runs for each of the cases shown was 0.0030, 0.0026, and 0.0025 respectively, which is on the same order of magnitude with the mass balance cases.

Table 4.3 shows the results for two zero-velocity gradient cases, one where the velocity gradient is zero in all three directions and the other where it is zero in only one direction. The total percentage errors were calculated using Eq. 3.121. A flow correction of 0.009% was used for both cases, which yielded total percentage errors of 0.05 and 0.02 respectively. Note however, for the second example it is possible to obtain a near exact answer by using a much smaller flow correction since there is a zero-velocity gradient in only one direction. In any case,

the percentage errors obtained from using the recommended flow correction of 0.009% are minute. The run times for the zero-velocity gradient cases are comparable to the other streamtube recreation cases.

Depending on the size of the model and the length of the simulation (i.e., number of stress periods and number of time steps in each stress period), a single MODFLOW run is on the order of hundredth of a second or more. Hence, the time take to obtain these results can be said to be approximately on the order of or less than a single MODFLOW run.

Table 4.1. Results for three special cases (cell dimensions are 1 unit x 1 unit x 1 unit and cell face flows are in [L^3/T]; maximum time to complete represents maximum from 1000 runs).

Visualization of Cell Face Flows	Recreation of Internal Streamtube Geometry (for visualization)	FCM Matrix (first shaded column indicates inflow face and top shaded row indicates outflow face)	Maximum time to complete (seconds)

1. Single inflow and/or single outflow

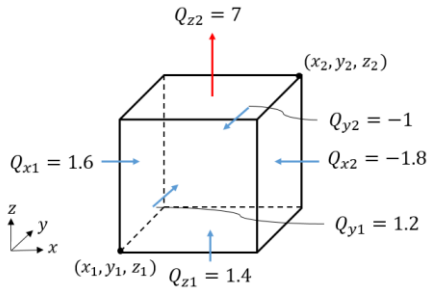

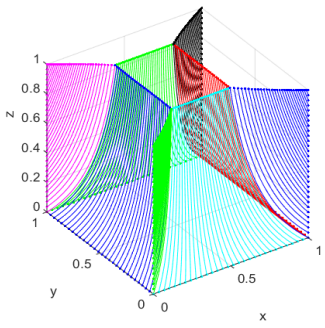

	z_1	x_1	y_2	x_2	y_1	z_2
z_1	X	0.0	0.0	0.0	0.0	1.4
x_1	0.0	X	0.0	0.0	0.0	1.6
y_2	0.0	0.0	X	0.0	0.0	1.0
x_2	0.0	0.0	0.0	X	0.0	1.8
y_1	0.0	0.0	0.0	0.0	X	1.2
z_2	-1.4	-1.6	-1.0	-1.8	-1.2	X

0.007

2. Stagnation point

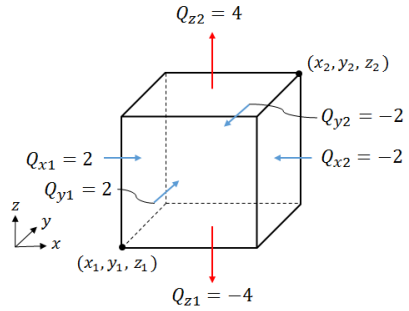

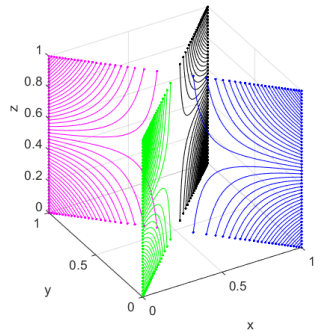

	z_1	x_1	y_2	x_2	y_1	z_2
z_1	X	0.0	0.0	0.0	0.0	0.0
x_1	0.0	X	-1.0	0.0	0.0	0.0
y_2	0.0	1.0	X	2.0	1.0	2.0
x_2	0.0	0.0	-2.0	X	0.0	0.0
y_1	0.0	0.0	-1.0	0.0	X	0.0
z_2	0.0	0.0	-2.0	0.0	0.0	X

0.008

3. Compatible with 2D-algorithm

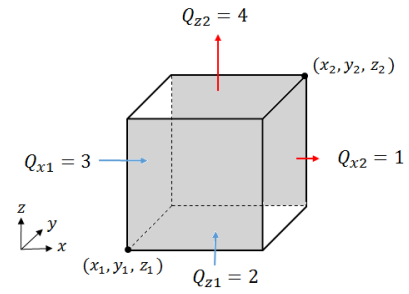

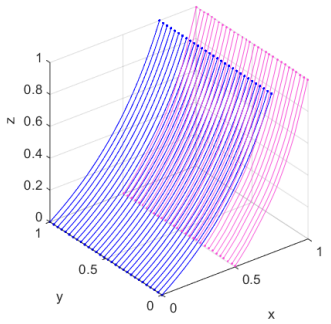

	z_1	x_1	y_2	x_2	y_1	z_2
z_1	X	0.0	0.0	1.0	0.0	1.0
x_1	0.0	X	0.0	0.0	0.0	3.0
y_2	0.0	0.0	X	0.0	0.0	0.0
x_2	-1.0	0.0	0.0	X	0.0	0.0
y_1	0.0	0.0	0.0	0.0	X	0.0
z_2	-1.0	-3.0	0.0	0.0	0.0	X

0.010

Table 4.2. Results for three general cases (cell dimensions are 1 unit x 1 unit x 1 unit and cell face flows are in [L^3/T]; maximum time to complete represents maximum from 1000 runs).

Visualization of Cell Face Flows	Recreation of Internal Streamtube Geometry (for visualization)	FCM Matrix (first shaded column indicates inflow face and top shaded row indicates outflow face)	Maximum time to complete (seconds)
1. Three inflows – three outflows, with inflows in all three coordinate directions 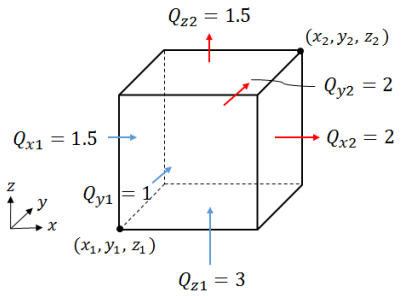	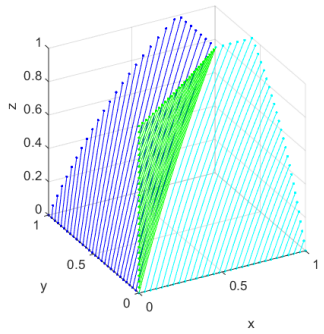	z_1 | X | 0.0000 | 1.3393 x_1 | 0.0000 | X | 0.6607 y_2 | -1.3393 | -0.6607 | X x_2 | -1.5244 | 0.0000 | 0.0000 y_1 | 0.0000 | 0.0000 | 0.0000 z_2 | -0.1363 | 0.0000 | 0.0000 x_2 | y_1 | z_2 z_1 | 1.5244 | 0.0000 | 0.1363 x_1 | 0.0000 | 0.0000 | 0.8393 y_2 | 0.0000 | 0.0000 | 0.0000 x_2 | X | -0.4756 | 0.0000 y_1 | 0.4756 | X | 0.5244 z_2 | 0.0000 | 0.0000 | X	0.144
2. Three inflows – three outflows, with inflow in two coordinate directions 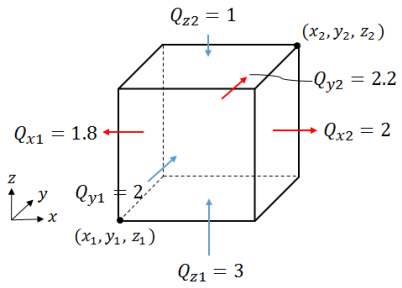	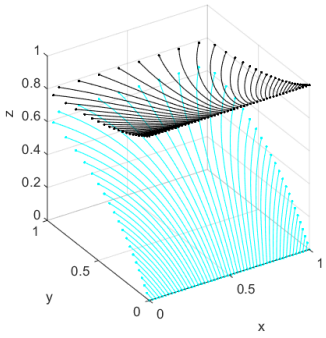	z_1 | X | 0.7557 | 1.4047 x_1 | -0.7557 | X | 0.0000 y_2 | -1.4047 | 0.0000 | X x_2 | -0.8396 | 0.0000 | 0.0000 y_1 | 0.0000 | 0.7925 | 0.3270 z_2 | 0.0000 | 0.2519 | 0.4682 x_2 | y_1 | z_2 z_1 | 0.8396 | 0.0000 | 0.0000 x_1 | 0.0000 | -0.7925 | -0.2519 y_2 | 0.0000 | -0.3270 | -0.4682 x_2 | X | -0.8805 | -0.2799 y_1 | 0.8805 | X | 0.0000 z_2 | 0.2799 | 0.0000 | X	0.127
3. Four inflows – two outflows 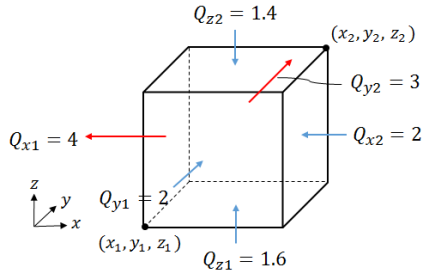	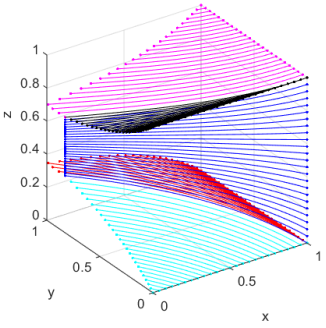	z_1 | X | 0.9373 | 0.6627 x_1 | -0.9373 | X | 0.0000 y_2 | -0.6627 | 0.0000 | X x_2 | 0.0000 | 0.2426 | 1.7574 y_1 | 0.0000 | 2.0000 | 0.0000 z_2 | 0.0000 | 0.8201 | 0.5799 x_2 | y_1 | z_2 z_1 | 0.0000 | 0.0000 | 0.0000 x_1 | -0.2426 | -2.0000 | -0.8201 y_2 | -1.7574 | 0.0000 | -0.5799 x_2 | X | 0.0000 | 0.0000 y_1 | 0.0000 | X | 0.0000 z_2 | 0.0000 | 0.0000 | X	0.134

Table 4.3. Results for two zero-velocity gradient cases (cell dimensions are 1 unit x 1 unit x 1 unit and cell face flows are in [L^3/T]; maximum time to complete represents maximum from 1000 runs; total percentage errors were calculated using (Eq. 3.121).

<table>
<tr><th>Visualization of Cell Face Flows</th><th>Recreation of Internal Streamtube Geometry (for visualization)</th><th>FCM Matrix (first shaded column indicates inflow face and top shaded row indicates outflow face)</th><th>Maximum time to complete (seconds)</th></tr>
<tr><td>1. Velocity gradients zero in all three coordinate directions
 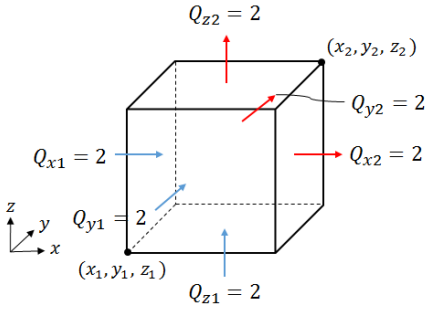
</td><td> 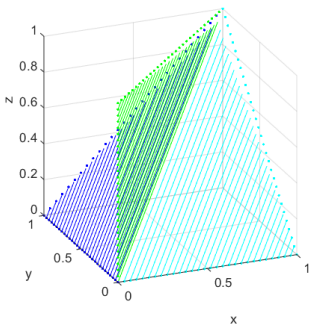 </td><td>Magnitude of Flow Correction = 0.009%
<table><tr><th></th><th>z_1</th><th>x_1</th><th>y_2</th></tr><tr><td>z_1</td><td>X</td><td>0.0000</td><td>1.0000</td></tr><tr><td>x_1</td><td>0.0000</td><td>X</td><td>1.0004</td></tr><tr><td>y_2</td><td>-1.0000</td><td>-1.0004</td><td>X</td></tr><tr><td>x_2</td><td>-0.9999</td><td>0.0000</td><td>0.0000</td></tr><tr><td>y_1</td><td>0.0000</td><td>0.0000</td><td>-0.0001</td></tr><tr><td>z_2</td><td>0.0000</td><td>-1.0002</td><td>0.0000</td></tr></table><table><tr><th></th><th>x_2</th><th>y_1</th><th>z_2</th></tr><tr><td>z_1</td><td>0.9999</td><td>0.0000</td><td>0.0000</td></tr><tr><td>x_1</td><td>0.0000</td><td>0.0000</td><td>1.00002</td></tr><tr><td>y_2</td><td>0.0000</td><td>0.0001</td><td>0.0000</td></tr><tr><td>x_2</td><td>X</td><td>-1.0003</td><td>0.0000</td></tr><tr><td>y_1</td><td>1.0003</td><td>X</td><td>0.9998</td></tr><tr><td>z_2</td><td>0.0000</td><td>-0.9998</td><td>X</td></tr></table></td><td>0.143
Total error in calculations (%)
0.05</td></tr>
<tr><td>2. Velocity gradients zero in one coordinate direction
 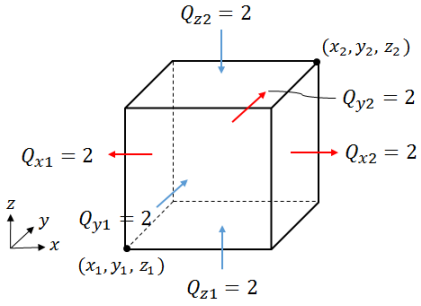
</td><td> 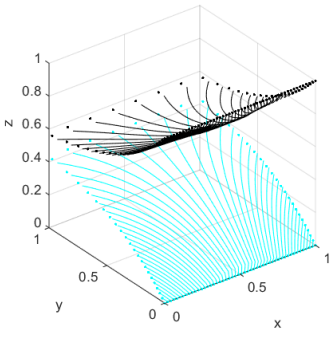 </td><td>Magnitude of Flow Correction = 0.009%
<table><tr><th></th><th>z_1</th><th>x_1</th><th>y_2</th></tr><tr><td>z_1</td><td>X</td><td>0.5677</td><td>0.8647</td></tr><tr><td>x_1</td><td>-0.5677</td><td>X</td><td>0.0000</td></tr><tr><td>y_2</td><td>-0.8647</td><td>0.0000</td><td>X</td></tr><tr><td>x_2</td><td>-0.5677</td><td>0.0000</td><td>0.0000</td></tr><tr><td>y_1</td><td>0.0000</td><td>0.8648</td><td>0.2707</td></tr><tr><td>z_2</td><td>0.0000</td><td>0.5677</td><td>0.8647</td></tr></table><table><tr><th></th><th>x_2</th><th>y_1</th><th>z_2</th></tr><tr><td>z_1</td><td>0.5676</td><td>0.0000</td><td>0.0000</td></tr><tr><td>x_1</td><td>0.0000</td><td>-0.8648</td><td>-0.5677</td></tr><tr><td>y_2</td><td>0.0000</td><td>-0.2707</td><td>-0.8647</td></tr><tr><td>x_2</td><td>X</td><td>-0.8647</td><td>-0.5676</td></tr><tr><td>y_1</td><td>0.8647</td><td>X</td><td>0.0000</td></tr><tr><td>z_2</td><td>0.5676</td><td>0.0000</td><td>X</td></tr></table></td><td>Maximum time to complete (seconds)
0.142
Total error in calculations (%)
0.02</td></tr>
</table>

The results presented in the preceding tables demonstrate that the algorithm developed here to compute the volumetric flow connections in a three-dimensional rectilinear cell is accurate and computationally inexpensive. Thus, it is a suitable solution to address the numerical dispersion issues inherent in FlowSource from its assumption of fully mixed cells.

4.1.2 Reduction of Numerical Dispersion in FlowSource

At the time of writing this thesis, the algorithm was still in the process of being incorporated into FlowSource. Hence, the actual reduction in numerical dispersion in FlowSource calculations as a result of implementing the algorithm cannot be demonstrated. Instead, the reduction in numerical dispersion that would be achieved for a hypothetical case is presented here.

The cell-by-cell flows for the hypothetical case is shown in Figure 4.1. The grid is three rows by three columns and has a planar flow field with a Southeast-Northwest gradient (i.e., equal cell face flows along the whole model domain). Cell G is the chosen 'destination cell'.

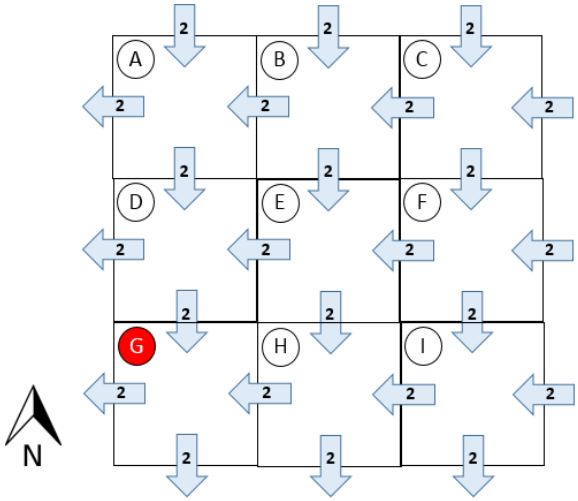

Figure 4.1. Cell-by-cell flows from a planar flow field with a SE-NW downward gradient.

Running this hypothetical case through the existing FlowSource would yield the directed acyclic graph shown in Figure 4.2.

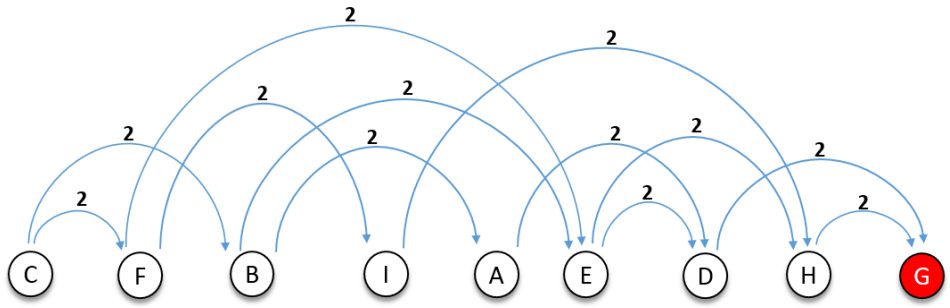

Figure 4.2. Directed acyclic graph for the cell-by-cell flows shown in Figure 4.1.

The corresponding FlowSource output for the fraction-through metric is shown in Figure 4.3.

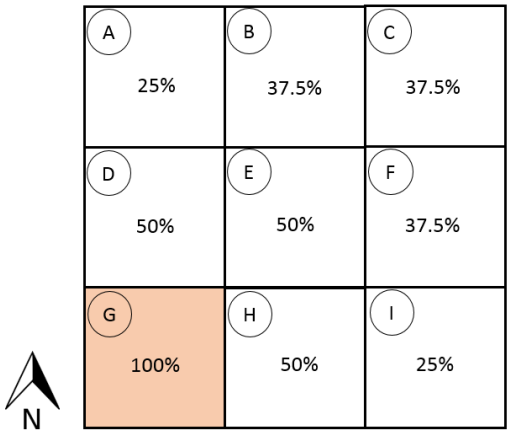

Figure 4.3. FlowSource cell-by-cell fraction-through values for a three row-three column grid with planar flow under fully-mixed assumption.

The flow field topology obtained from FlowSource as shown in Figure 4.2 show that all the cells are connected to the destination cell (i.e., cell G) and the corresponding FlowSource output in Figure 4.3 show that all the cells have some flow passing through it that eventually reaches cell G. However, if we revoke the assumption of fully mixed cells and recreate the dividing streamtubes inside each cell by forward tracking all the inflow corners using Pollock's method, it would yield a more accurate image of the flow field topology as shown in Figure 4.4.

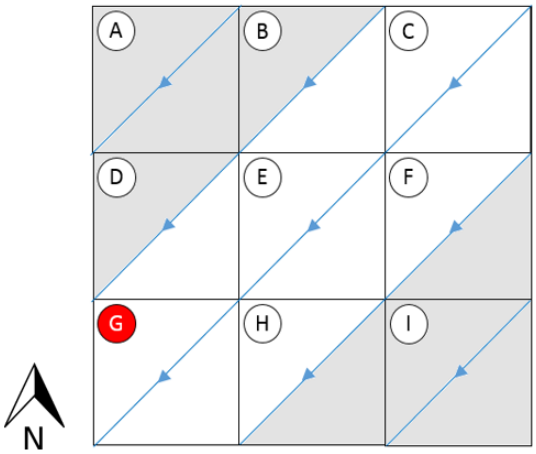

Figure 4.4. Internal streamtubes recreated by forward tracking inflow corners inside each cell using Pollock's method; areas that are not hydraulically connected to the destination cell (cell G) are shaded grey.

Note in Figure 4.4 that cells A and I do not convey any flow to the cell G and as such should not be included in the calculations at all. On the other hand, the FlowSource output underestimates the amount of flow conveyed through cells E, C, B, and F. Figure 4.4 shows that in actuality 100% of the flow passing through cells E and C reach cell G, while 50% of the flows through cells B and F reach cell G.

Now let us recreate the directed acyclic graph for the flow field topology shown in Figure 4.4. Since we are not assuming the cells to be fully mixed, then each flow should be represented as the sum of all its 'un-mixed' components, given by,

$$Q_{i,j} = \sum_{k=1}^{n} f_k Q_k \qquad \textbf{(Eq. 4.1)}$$

where, $Q_{i,j}$ is the flow from cell i to cell j; n is the total number of inflows, Q_k, into cell i; and f_k is the fraction of Q_k that flows into cell j from cell i.

Also, if a flow enters a cell k from outside the model domain and it is on the East-West axis, then we will define it as, $Q_{od-x,k}$. Similarly, if an out of domain flow enters the cell and it is on the North-South axis, then we will define it as, $Q_{od-y,k}$.

Figure 4.5 shows the directed acyclic graph for the planar flow field again but this time the flows have been represented in the form $Q_{i,j}$.

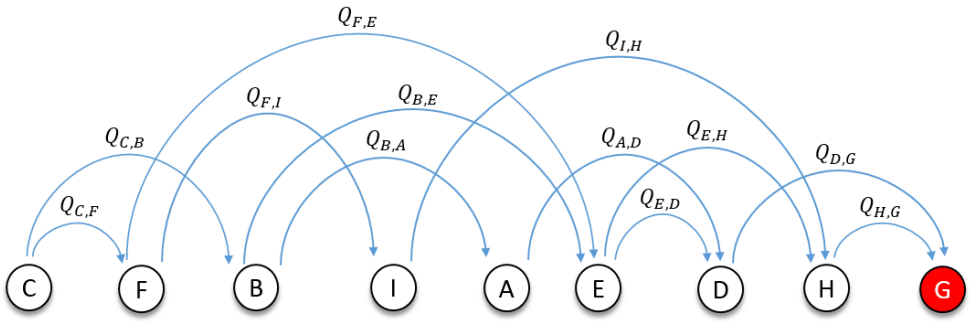

Figure 4.5. Directed acyclic graph with flows represented as inter-cell flows.

Now each of the inter-cell flows can be expressed as the sum of their components using Eq. 4.1. The expressions are presented in Table 4.4 starting from the destination cell and sequentially going upstream.

Table 4.4. Inter-cell flows from hypothetical case expressed as constituent flows.

Inter-Cell Flow	Constituent Flows
$Q_{H,G}$	$= 0(Q_{I,H}) + 1(Q_{E,H}) = 2$
$Q_{D,G}$	$= 0(Q_{A,D}) + 1(Q_{E,D}) = 2$
$Q_{E,H}$	$= 1(Q_{F,E}) + 0(Q_{B,E}) = 2$
$Q_{E,D}$	$= 0(Q_{F,E}) + 1(Q_{B,E}) = 2$
$Q_{A,D}$	$= 1(Q_{B,A}) + 0(Q_{od-y,A}) = 2$
$Q_{I,H}$	$= 1(Q_{F,I}) + 0(Q_{od-x,I}) = 2$
$Q_{B,E}$	$= 1(Q_{C,B}) + 0(Q_{od-y,B}) = 2$
$Q_{B,A}$	$= 0(Q_{C,B}) + 1(Q_{od-y,B}) = 2$
$Q_{F,E}$	$= 1(Q_{C,F}) + 0(Q_{od-x,F}) = 2$
$Q_{F,I}$	$= 0(Q_{C,F}) + 1(Q_{od-x,F}) = 2$
$Q_{C,B}$	$= 0(Q_{od-x,C}) + 1(Q_{od-y,C}) = 2$
$Q_{C,F}$	$= 1(Q_{od-x,C}) + 0(Q_{od-y,C}) = 2$

Using the expressions in Table 4.4, it is now possible to conduct the FlowSource calculations. Cell G is the destination cell, thus it is assigned to have 100% flow through. Cell H

has 4 units flowing in, out of which 2 units flow into Cell G. Thus, Cell H has a fraction-through of 50%. Similarly, Cell D has 4 units flowing in and 2 units flow out to cell G. So, it too has a fraction-through of 50%. Cell E has 4 units flowing in, 2 units flowing out to cell H and 2 units flowing out to cell D. Note from Table 4.4, that all of the 2 units that cell H conveys to cell G comes from cell E (i.e., $1 * Q_{E,H}$). Similarly, all of the 2 units that cell D conveys to cell G comes from cell E (i.e., $1 * Q_{E,D}$). Thus, cell E has a fraction-through of 100%. Sequentially traversing upstream through all the cells in this manner by using the expressions outlined in Table 4.4, yields the cell-by-cell fraction-through values shown in Figure 4.6. Note that these values can be visually validated from the dividing streamtubes shown in Figure 4.4.

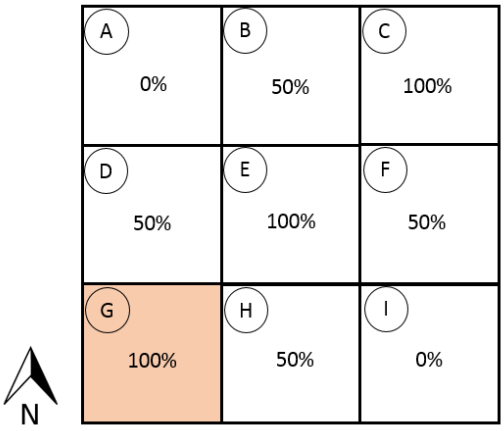

Figure 4.6. FlowSource cell-by-cell fraction-through values for a three-row three-column grid with planar flow after revoking fully-mixed assumption.

Thus, if the algorithm that has been developed for this thesis to compute volumetric flow connections in rectilinear finite-difference cells is incorporated into FlowSource, it can effectively reduce the numerical dispersion in FlowSource calculations as demonstrated with the hypothetical case. It should also be noted that the algorithm is not necessarily restricted for use in FlowSource. It can also be used for MODALL (Potter et al. 2008). MODALL is volumetric capture delineation tool that uses cell-by-cell flows from MODFLOW models and applies the fully mixed assumption as well. Consequently, its calculations also show numerical dispersion

when using coarse grids (McLane and Cecan, 2009). Incorporation of the algorithm into MODALL would actually be an easier task because MODALL uses a simpler calculation scheme than FlowSource (i.e., it does not use directed acyclic graphs). However, a more elaborate discussion on the topic is outside the scope of this thesis. In any case, the algorithm can be used with any volumetric capture delineation tool that uses cell-by-cell flows from a finite-difference flow model with rectilinear grids to reduce numerical dispersion in calculations resulting from the assumption of fully mixed cells.

4.2 Comparison with the LRD Method

The tool developed for this thesis to map well connectivity to surface-water features is based on the LRD method (Leake et al., 2010). The mechanics of the tool are essentially the same as the LRD method, except instead of evaluating the difference in the flows to and out of the aquifer between a base model and the same model with a single added withdrawal, it applies FlowSource (Black and Foley, 2013) for the model with the added withdrawal. Thus, it is necessary to compare the results produced by the two methods to demonstrate that the tool developed here provides different information. Two synthetic steady-state cases are used to compare the output of the modeling tool and the LRD method. Since both methods are MODFLOW (Harbaugh et al., 2000) based, the models were developed in MODFLOW-2000. Also, for the comparison it is necessary to re-examine the term ‘capture’. In the literature, capture is defined as any pumping induced changes in flows to or out of the aquifer (Leake et al., 2010). In the discussions following, this will be referred to as ‘LRD-capture’ in order to distinguish it from the values obtained from FlowSource, which will be referred to as ‘volumetric-capture’. When referring to the fractional equivalents of these two metrics, the terms ‘LRD-capture fraction’ and ‘volumetric-capture fraction’ will be applied.

4.2.1 Single Stream Case

The first test is a homogenous unconfined aquifer with a single linear stream. The model has one layer, 31 rows, and 10 columns, with equal horizontal and vertical grid spacing. There is uniform areal recharge across the top layer of the model. The details of the model are outlined in Table 4.5.

Table 4.5. Model details for single stream case.

Parameter	Value
Simulation Type	Steady-state
Model Dimensions	31 rows x 10 columns x 1 layer
Cell Dimensions	100 m x 100 m
Elevation of top layer (single layer)	100 m
Uniform areal recharge	5e-04 m/d
Hydraulic Conductivity	$K_x = K_y = 3$ m/d; $K_z = 0.3$ m/d
Storage, S_s	2e-04 [-]
Specific Yield, S_y	0.2 [-]
Porosity, η	0.3 [-]
Boundary Conditions	Initial heads set as 100 m in all cells for steady-state simulation; all stream cells set with constant head of 100 m

Figure 4.7 (a) shows the head distribution from running a steady-state simulation without any wells. Note, that the stream is a gaining stream. Figure 4.7 (b) shows the corresponding LRD-capture fraction contour map after one year of pumping at a constant rate of 5,000 m^3/d. The contour map was generated using the LRD method described in Section 2.3.2. Pumping locations were considered in every row and every column, requiring 300 MODFLOW runs. Note, all the runs with the added wells were transient simulations, since otherwise there would be no change in storage and LRD-capture fraction would be 1 across the model domain (i.e., all the pumped water would be supplied by LRD-capture).

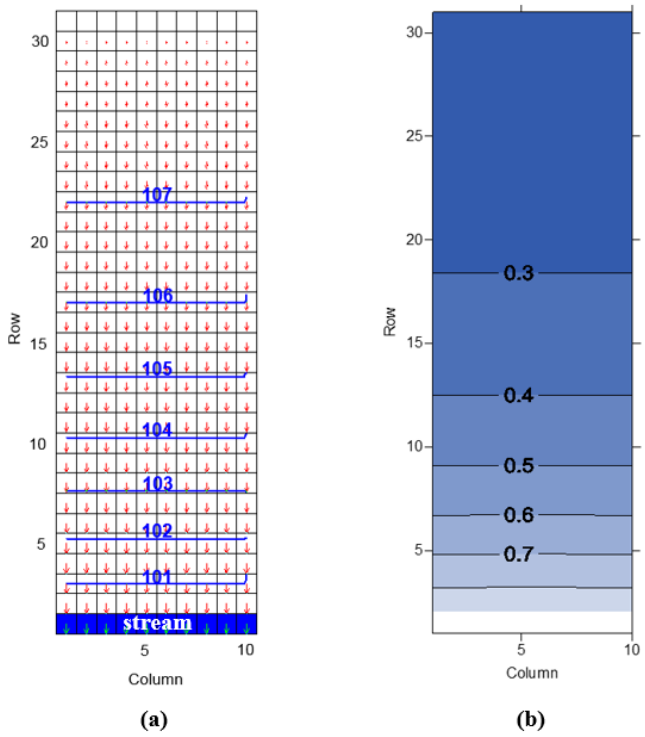

Figure 4.7. Steady-state head distribution without any pumping wells for single stream case; velocity vectors shown in red (a) and corresponding LRD capture-fraction contour map after one year of constant pumping at 5000 m^3/d (b).

Figure 4.7 (b) shows, as expected, that LRD-capture is highest closest to the stream and gradually decreases as the well location moves away from the stream. Also, since the stream is linear, so are the capture contours. Figure 4.8 illustrates the head distributions from three specific well runs along column 5: (1) well immediately adjacent to the stream (i.e., row 2), (2) well midway along the model domain (i.e., row 15), (3) well at the edge opposite the stream (i.e., row 31). Note that in all three cases pumping reverses the hydrologic condition of the stream from being a groundwater discharge feature, as shown in Figure 4.7 (a), to a groundwater recharge feature. Thus, pumping anywhere along the model domain at a constant rate of 5,000 m^3/d for one year will induce the stream to become a losing stream.

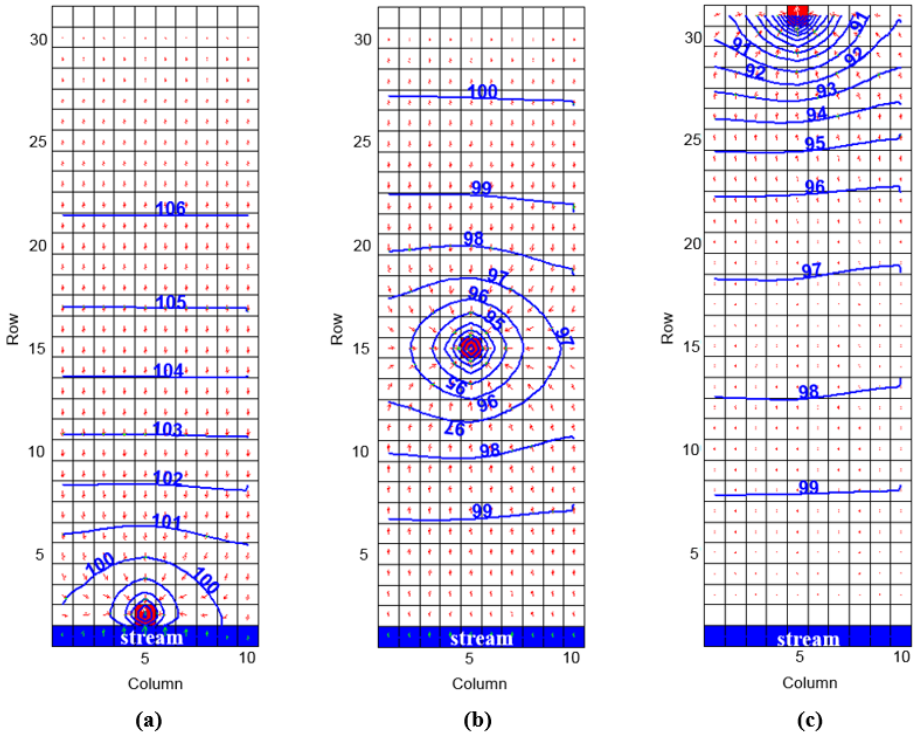

Figure 4.8. Head distributions of single stream case after one year for pumping at 5000 m^3/d immediately adjacent to the stream (a), midway along the model domain (b), and furthest away from the stream (c); wells are indicated by the shaded red square in each figure. In all three cases the steady-state hydrologic condition of the stream is reversed from being a groundwater discharge feature to a groundwater recharge feature.

Note, for this case there is no evapotranspiration, and the areal recharge is kept constant for all the runs. Thus, the only components of LRD-capture are the reduction in baseflow to the stream (outflow from aquifer) and increased stream-leakage (inflow to aquifer). To understand how the individual capture components influence the overall LRD-capture, we can examine them along a single column since the LRD-capture fraction profile only changes vertically. Figure 4.9 illustrates a graph of the LRD-capture, increased stream-leakage, and reduced baseflow fractions along column 5 of the model. Note, that when pumping is furthest from the stream, it only induces a reduced base-flow. The reduction in base-flow increases gradually as the location of pumping approaches closer to the stream and then after row 17, it begins to induce stream leakage. After that point, the reduction in base-flow plateaus and further increases in capture is entirely generated by increases in induced stream leakage.

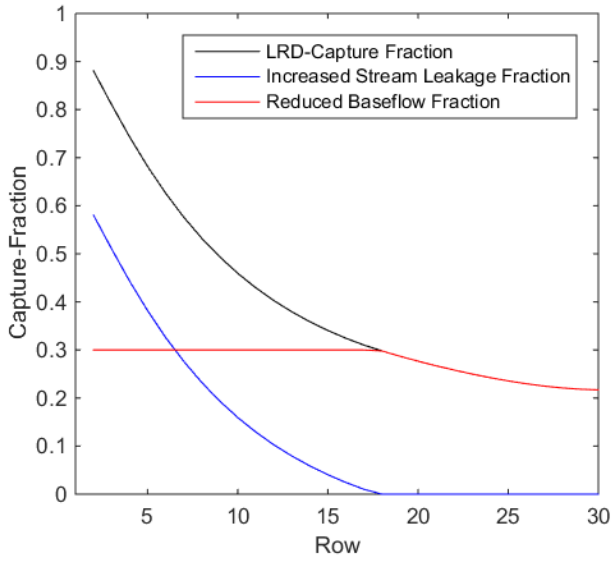

Figure 4.9. Graph of LRD-capture, increased stream leakage, and reduced baseflow fractions along column 5 of the single stream case model.

For the purposes of this thesis, we are concerned about the amount of well water that is sourced from surface-water. Thus, we are specifically concerned about the stream-leakage component of LRD-capture. Figure 4.10 shows a comparison of the increased stream-leakage fraction contour map and the volumetric-capture contour map generated using the modeling tool developed for this thesis. Note that the volumetric-capture fraction contour map and the induced stream leakage contour map appear to be the same.

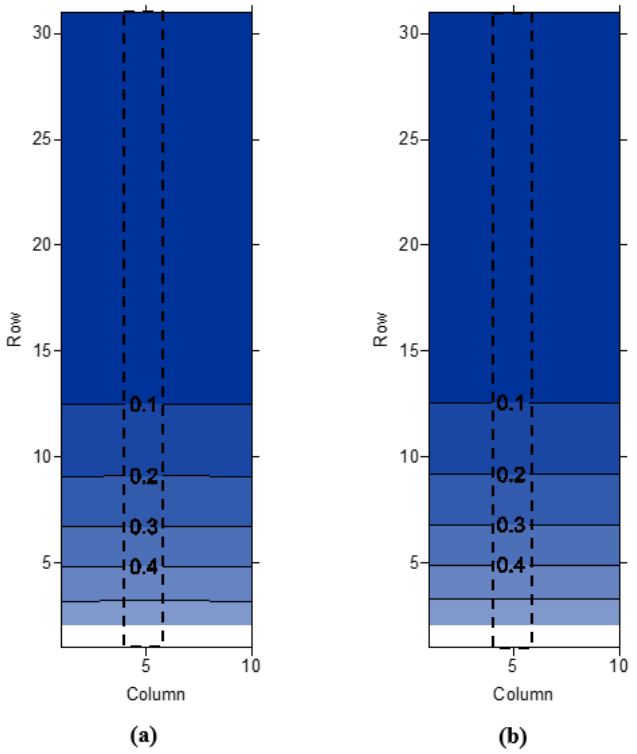

Figure 4.10. Contour maps of increased stream leakage component of LRD-capture fraction (a), and volumetric-capture fraction (b) for single stream case; column 5 is delineated with black dashed lines in both maps.

Comparing the two metrics along a vertical cross-section of the domain (i.e., column 5) as shown in the graph in Figure 4.11 reveals that for this case, the two are in fact identical. Therefore, for this simple single stream case, the modeling tool does not seem to offer any information that cannot be obtained from implementing the LRD-method.

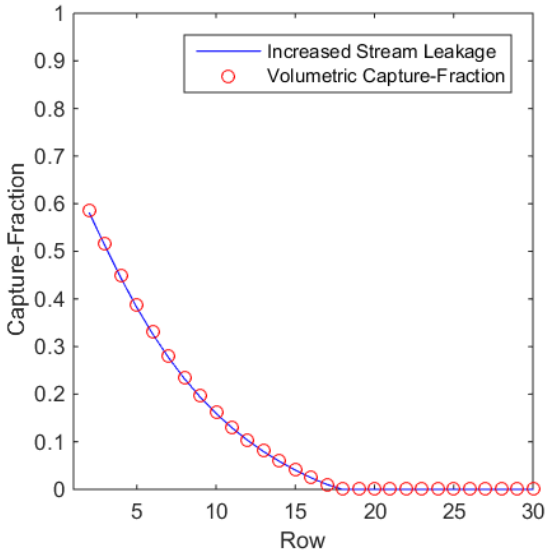

Figure 4.11. Graph of increased stream leakage component of LRD-capture fraction and volumetric-capture fraction along column 5 of the single stream case model.

4.2.2 Two Stream Case

Now, consider a similar case but where there are two linear streams at either end of the model domain. The details of the model are outlined in Table 4.6.

Table 4.6. Model details for two stream case.

Parameter	Value
Simulation Type	Steady-state
Model Dimensions	32 rows x 10 columns x 1 layer
Cell Dimensions	100 m x 100 m
Elevation of top layer (single layer)	200 m
Uniform areal recharge	5e-04 m/d
Hydraulic Conductivity	$K_x = K_y = 3$ m/d; $K_z = 0.3$ m/d
Storage, S_s	2e-04 [-]
Specific Yield, S_y	0.2 [-]
Porosity, η	0.3 [-]
Boundary Conditions	Initial heads set as 200 m in all cells for steady-state simulation; stream cells along row 1 set with constant head of 200 m and along row 32 set with constant head of 150 m

Figure 4.12 shows the head distribution from running a steady-state simulation without any wells. Note that for this case, the stream along row 1, stream A, is a losing stream, while the stream along row 32, stream B, is a gaining stream.

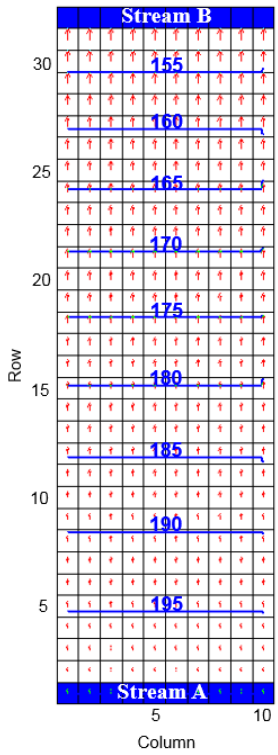

Figure 4.12. Steady-state head distribution without any pumping wells for two stream case; velocity vectors shown in red

The contour maps were generated for a well with a constant pumping rate of 20,000 m^3/d for one year. As for the single stream case, Figure 4.13 illustrates the head distributions from three specific well runs along column 5: (1) well immediately adjacent to stream A (i.e., row 2), (2) well approximately midway along the model domain (i.e., row 19), (3) well immediately adjacent to stream B (i.e., row 31). Figure 4.13 shows that the hydrologic condition of the losing stream remains unchanged for pumping anywhere along the model domain but for the gaining stream, it reverses once the pumping well is sufficiently close.

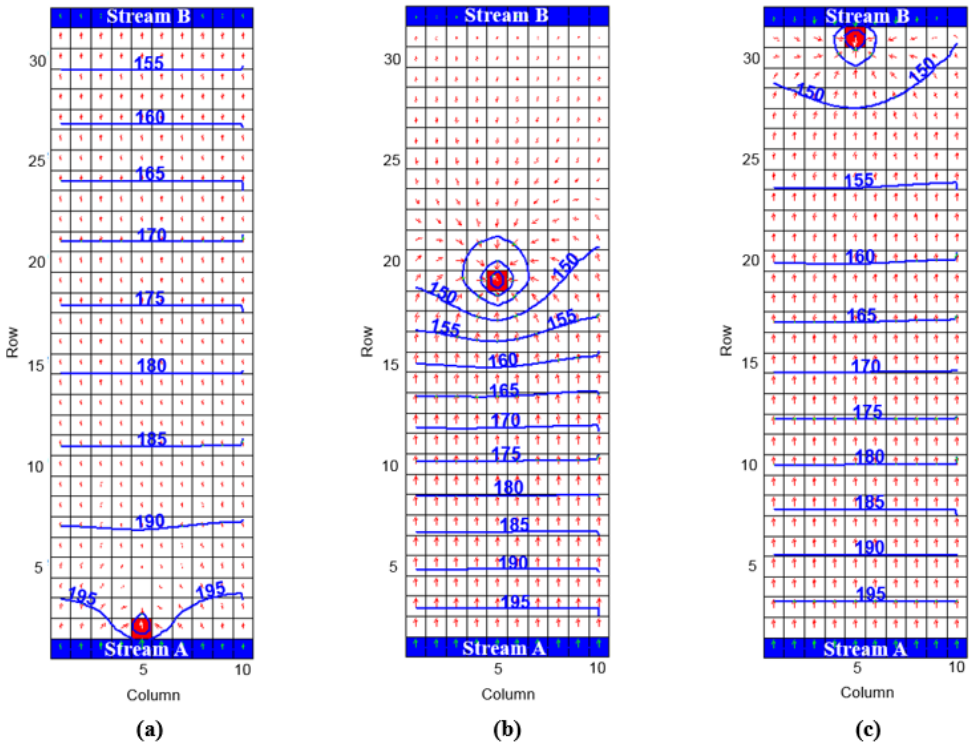

Figure 4.13. Head distributions of two stream case after one year for pumping at -20,000 m^3/d at row 2 (a), row 15 (b), and row 31 (c); wells are indicated by the shaded red square in each figure. For all three cases the steady-state hydrologic condition of the losing stream remains unchanged but for the gaining stream, it is reverses once the pumping well is sufficiently close.

Figure 4.14 shows a comparison of the contour maps of LRD-capture fraction, increased stream leakage and reduced baseflow components of LRD-capture fraction, and the volumetric-capture fraction for the two streams. Figure 4.14 shows that the volumetric-capture fraction and the increased stream leakage fraction contour maps for the two stream case are not the same, which is unlike the single stream case.

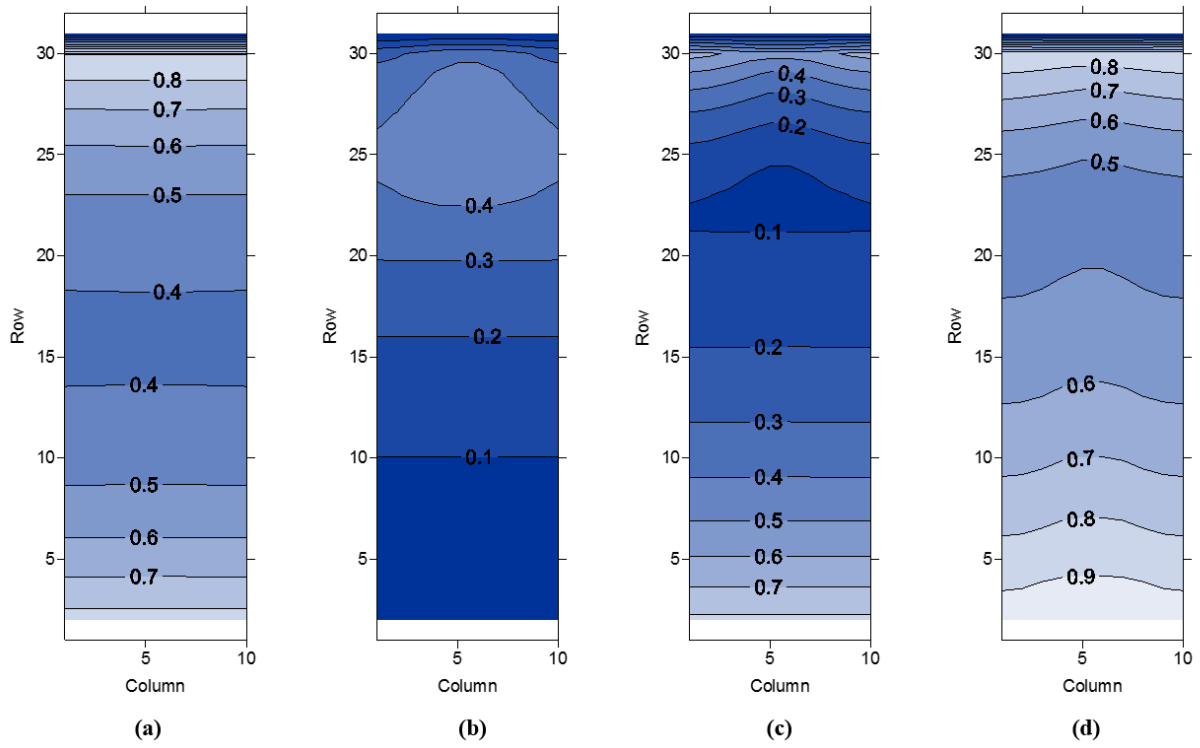

Figure 4.14. Contour maps of LRD-capture fraction (a), reduced baseflow fraction (b), increased stream leakage fraction (c), and volumetric-capture fraction (d) for two stream case.

Again, for a closer assessment, we can compare all the metrics along a vertical cross-section of the model domain (i.e., column 5) as shown in the graph in Figure 4.15.

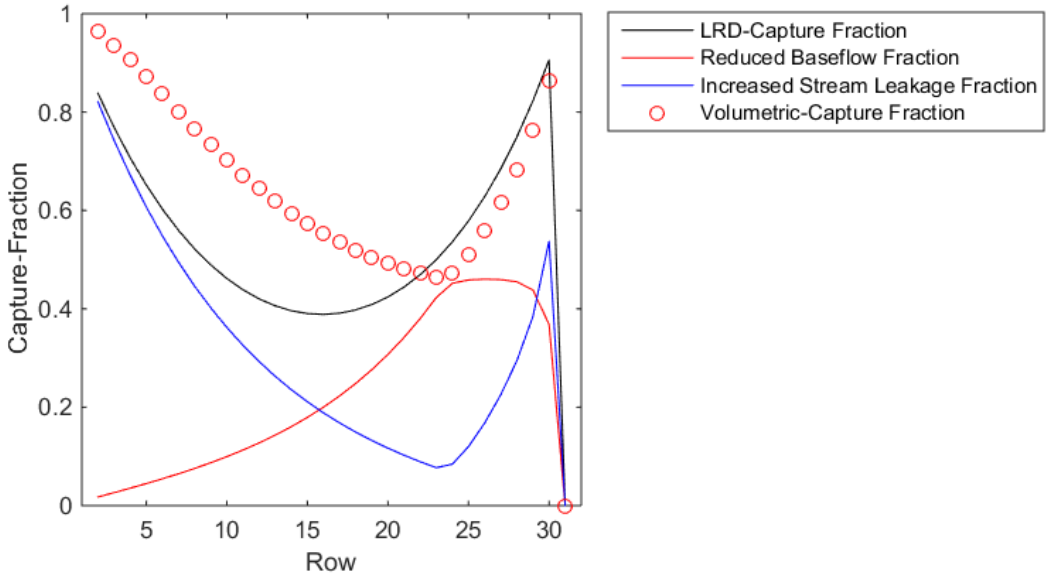

Figure 4.15. Graph of increased stream leakage component of LRD-capture fraction and volumetric-capture fraction along column 5 of the two stream case model.

Figure 4.15 shows that while the volumetric-capture fraction and increased stream leakage fraction follow similar trajectories for the two stream case, FlowSource estimates a much greater capture from the streams. To get a better understanding of the reasoning behind the difference in the estimates of capture from the streams between the two methods, we can examine the streams one at a time. Figure 4.16 shows a comparison of the increased stream leakage fraction and volumetric-capture fraction for stream A (i.e., the losing stream) and Figure 4.17 shows the corresponding comparison graph along the same vertical cross-section.

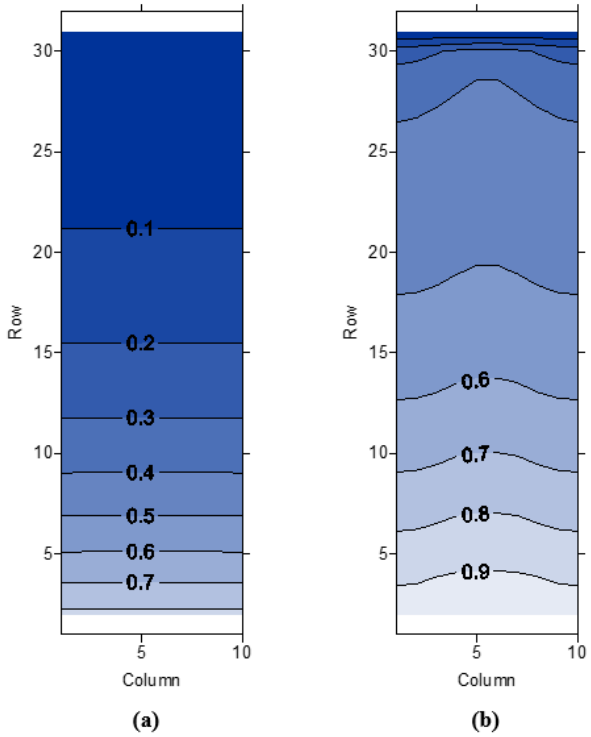

Figure 4.16. Contour maps of increased stream leakage component of LRD-capture fraction (a) and volumetric-capture fraction (b) for stream A (the losing stream).

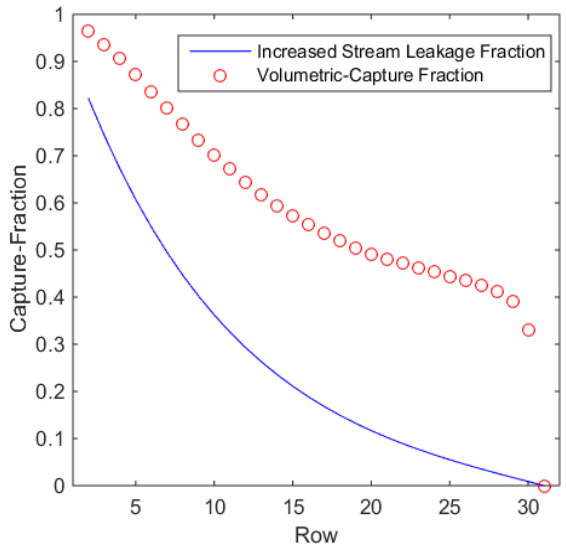

Figure 4.17. Graph of increased stream leakage component of LRD-capture fraction and volumetric-capture fraction along column 5 for stream A (the losing stream).

Note again, that FlowSource estimates a much greater capture from the losing stream than that estimated by the stream leakage component of LRD-capture. Now we follow the same procedure for stream B (i.e., the gaining stream). Figure 4.18 shows the comparison of the contour maps obtained from the two methods and Figure 4.19 shows the corresponding comparison graph. It turns out that for the gaining stream, like with the single stream case, the volumetric-capture fraction values computed by FlowSource exactly match the increased stream leakage fraction values computed using the LRD method.

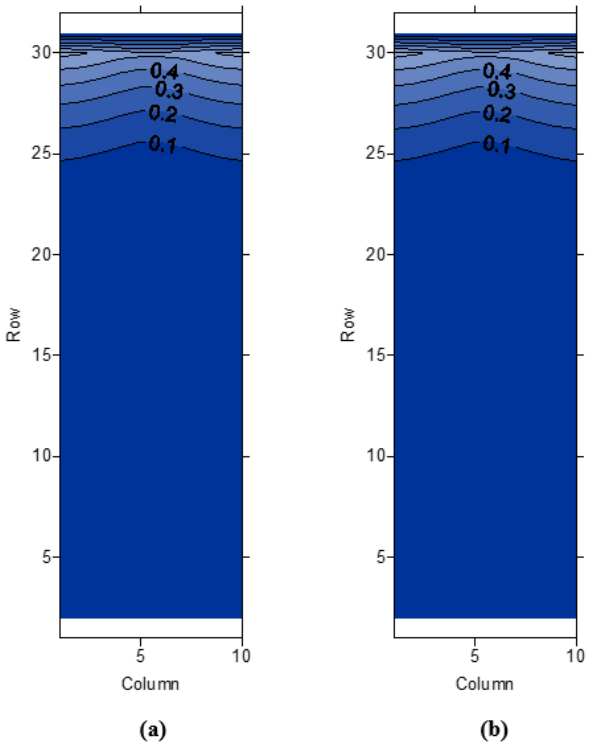

Figure 4.18. Contour maps of increased stream leakage component of LRD-capture fraction (a) and volumetric-capture fraction (b) for stream B (the gaining stream).

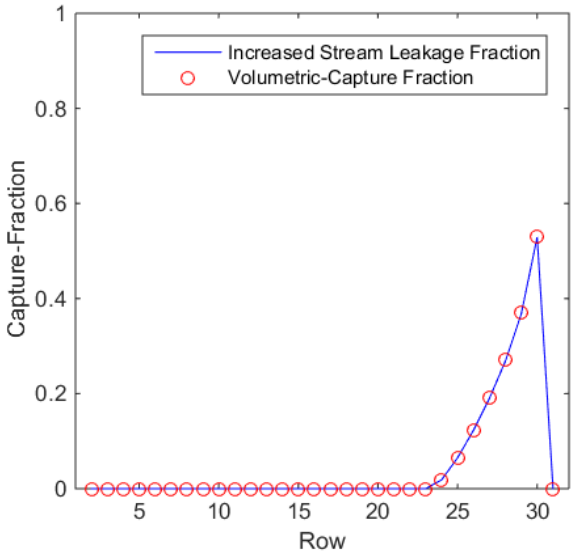

Figure 4.19. Graph of increased stream leakage component of LRD-capture fraction and volumetric-capture fraction along column 5 for stream B (the gaining stream).

Recall, that the stream leakage contour map generated using the LRD method shows the fraction of pumping that is supplied from increases in stream leakage as a result of pumping,

while the contour map generated using the modeling tool (i.e., using FlowSource) shows the fraction of pumping that is sourced from the stream (i.e., the fractional volume of water that originated in the stream cells and was extracted at the pumping cell). For the cases shown with the gaining streams, there is no stream leakage before any pumping begins and it is only induced after the wells are introduced. Thus, the total volume of water sourced from the stream is the induced stream leakage. However, for the losing stream, stream leakage is occurring even before pumping begins and the introduction of pumping increases that leakage. The LRD method only shows the amount that the stream leakage increased by as a result of the pumping, while the volumetric capture maps produced by the modeling tool shows the total stream leakage that is occurring at the time of pumping. This is why the combined capture from the two streams and the capture from the losing stream was estimated to be greater by FlowSource than by the LRD method. So, even if pumping induces no hydrological changes in the stream, there can still be water flowing from the stream to the well and it is in quantifying these flows that the two methods differ.

The LRD method was developed to assess the hydrological impacts of pumping on surface-water and it adequately serves that function. However, from the perspective of estimating well vulnerability, it is necessary to be able to determine the absolute amount of well water that is sourced from surface-water (as opposed to the relative amount) and this is what FlowSource can provide. The FlowSource output also implicitly provides an insight into the hydrological impacts of pumping on surface-water, since we know the total volume of water that is being removed from the surface-water feature.

4.3 Applications for Screening Existing Wells

A synthetic case is presented to demonstrate the applications of the tool developed here in determining the degree of connectivity of an existing well field to adjacent surface-water and agricultural lands. As noted before, this is essentially a novel application of FlowSource (Black and Foley, 2013). While FlowSource has been used to delineate volumetric capture areas for various purposes (i.e., well head protection and pump and treat optimization), it has not been used specifically to determine the volumetric connections of groundwater wells and surface-water features (Black and Foley, 2013).

4.3.1 Assessing Connectivity to Surface-Water

A steady-state MODFLOW-2000 (Harbaugh et al., 2000) model was used for the demonstration. The model has two layers, 50 rows, and 50 columns, with an equal horizontal and vertical grid spacing of 100 metres (m). The top layer is unconfined and 15 m deep, while the bottom layer is confined and 35 m deep. The confining layer is not simulated with a separate model layer. There is uniform areal recharge across the top layer of the model. Both aquifers have the same parameters and are homogenous. There is a Northeast – Southwest planar gradient along both layers and a stream in the top layer that flows from the Northeast corner to the Southwest corner of the model. The details of the model are summarized in Table 4.7.

Table 4.7. Model details of synthetic well field case.

Parameter	Value
Simulation Type	Steady-state
Model Dimensions	2 layers x 50 rows x 50 columns
Cell Dimensions	100 m x 100 m
Elevation of bottom layer	0 – 35 m (confined)
Elevation of top layer	35 – 50 m (unconfined)
Layer gradient	NE-SW gradient of 0.001 for both layers (i.e., NE corner is the highest elevation, SW corner is the lowest elevation, and the NW and SE corners are the same elevation, but lower than the NE corner and higher than the SE corner)
Uniform Areal Recharge	1e-03 m/d
Hydraulic Conductivity	$K_x = K_y = 30$ m/d; $K_z = 3$ m/d
Storage, S_s	1e-05 [-]
Specific Yield, S_y	0.01 [-]
Porosity, η	0.015 [-]
Boundary Conditions	Initial heads set as 50 m in all cells for steady-state simulation; all stream cells set as constant head cells, where the head is the top of the cell

The existing well field consists of seven wells, all pumping from the confined layer. The details of the wells are outlined in Table 4.8.

Table 4.8. Well locations and pumping rates of synthetic well field case

Well Identifier	Well Location (layer, row, column)	Constant Pumping Rate (m^3/d)
Well A	(2, 48, 12)	4,000
Well B	(2, 32, 42)	6,000
Well C	(2, 39, 17)	8,000
Well D	(2, 3, 47)	8,000
Well E	(2, 40, 29)	10,000
Well F	(2, 9, 17)	12,000
Well G	(2, 13, 33)	14,000

The head distributions obtained for the model from running a steady-state simulation in MODFLOW-2000 is shown in Figure 4.20.

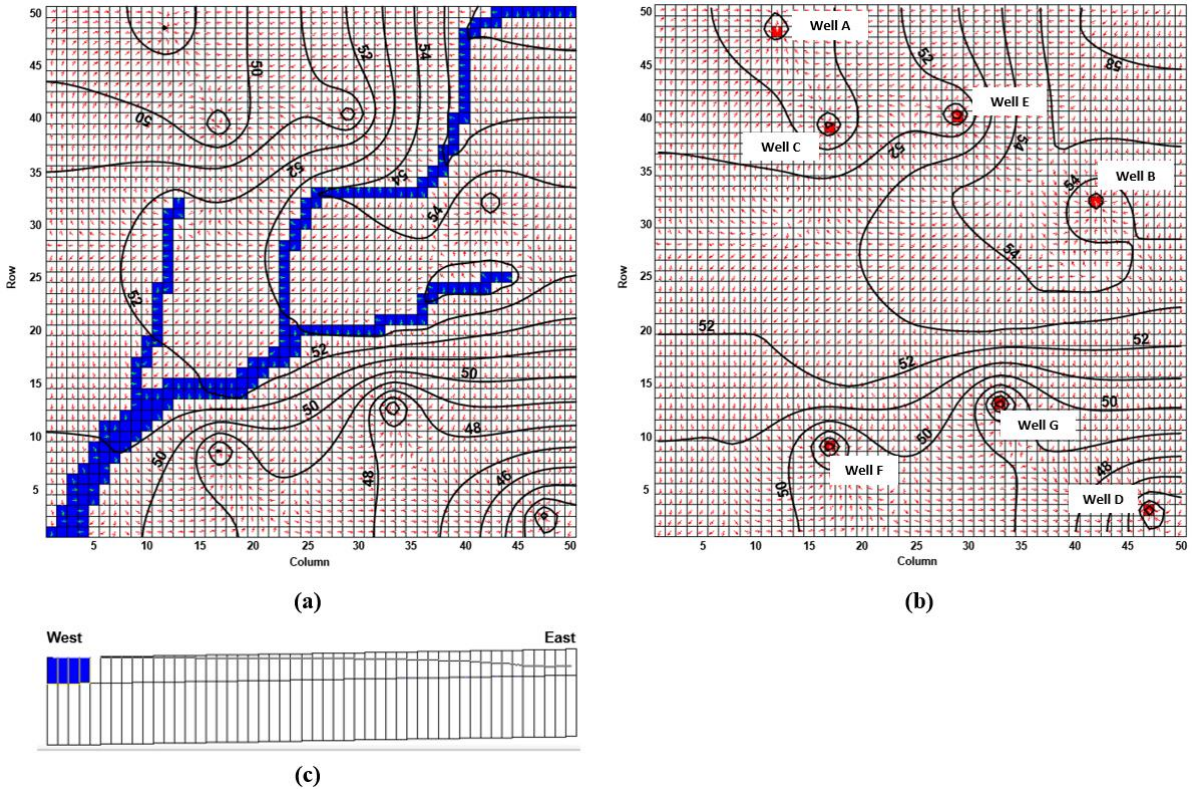

Figure 4.20. MODFLOW-2000 model of synthetic well field case: steady-state head distributions shown for layer 1 (a), layer 2 (b) and the cross-section along row 1 (c); head contours are shown with dark black lines, stream cells are shaded blue (shown in layer 1 and the cross-sectional view), wells are shaded red (shown in layer 2), and velocity vectors are shown with red arrows.

Now, we can simply assign all the stream cells as the 'feature of interest' in the tool, and run FlowSource for each well to estimate the volume of pumpage supplied by the stream. Since we are interested in computing the volume of water each well derives from the stream, the 'volume-from' and 'fraction-from' metrics were used from FlowSource (as opposed to the 'volume-through' and 'fraction-through' metrics). The results for the wells are provided in Table 4.9.

Table 4.9. FlowSource results for synthetic well field case

Well Identifier	Constant Pumping Rate (m^3/d)	Volumetric Capture from the stream (m^3/d)	Fraction of pumpage derived from the stream (%)
Well A	4,000	764	19
Well B	6,000	3851	64
Well C	8,000	5142	64
Well D	8,000	3745	47
Well E	10,000	8090	81
Well F	12,000	8958	75
Well G	14,000	10939	78

Figure 4.21 shows a map that was created using the estimates from Table 4.9 to visually portray the degree of connectivity of each well with the stream. Note, since this is a steady-state model, there is no change in storage and all the pumped water is provided by capture from the stream and/or areal recharge. The map contains pie-charts illustrating the breakdown of the volumetric fractions each well sources from the stream and areal recharge and the pies are scaled based on the amount sourced from the stream.

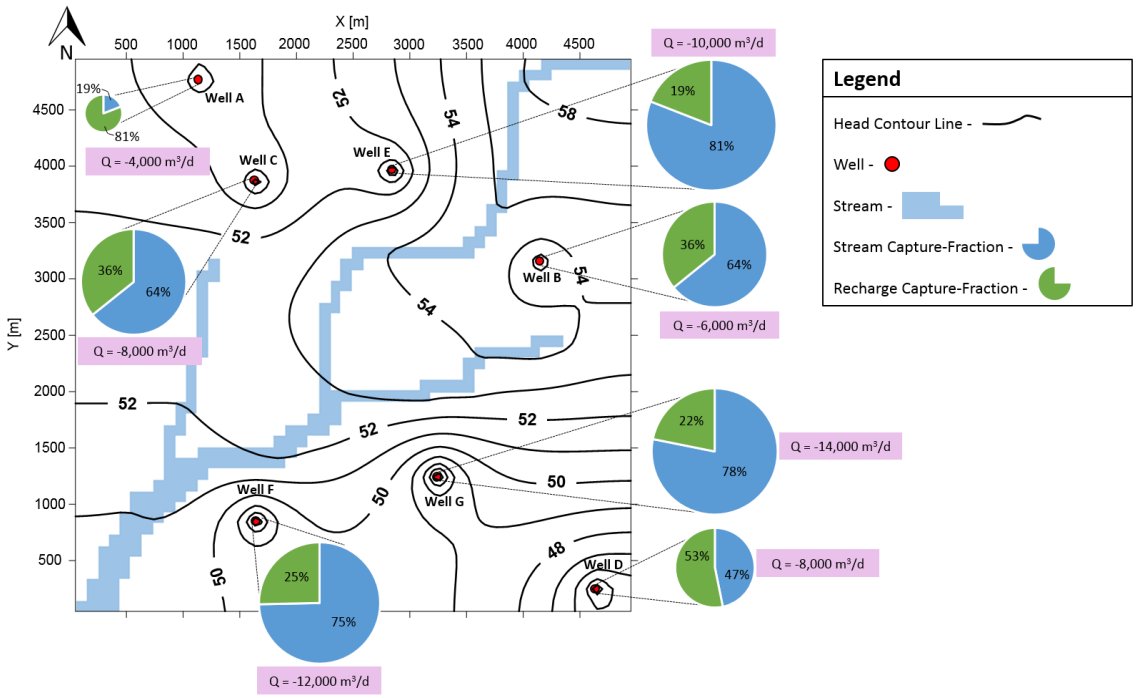

Figure 4.21. Map illustrating the connectivity of wells and the steam for the synthetic well field model; the locations of the wells are shown with the red circles and their volumetric capture-fractions from the stream and areal recharge are shown with scaled pies (i.e., larger pies indicate greater capture from the stream); pumping rates are shown next to the pies; the stream and the steady-state head distribution for layer 2 have also been overlaid the map.

From Figure 4.21, we see that only the wells located furthest from the streams, Well A and Well D, are not surface-water dominated (i.e., have well water compositions that are less than 50% surface-water). The remaining wells, especially Well E, Well G, and Well F, may all be deemed as vulnerable since they are all surface-water dominated.

Now, if contamination is restricted to a specific reach of the stream or if a specific reach supports sensitive aquatic habitat, it may be more desirable to see how much water each well derives/removes from that reach. The ability to determine volumetric capture from multiple features of interest can be made use of for these purposes. Figure 4.22 shows a map with estimates of the volumetric fractions captured by each well from: (1) the tributary at the west end of the model, the Western tributary, (2) the tributary at the east end of the model, the Eastern tributary, and (3) the main stream.

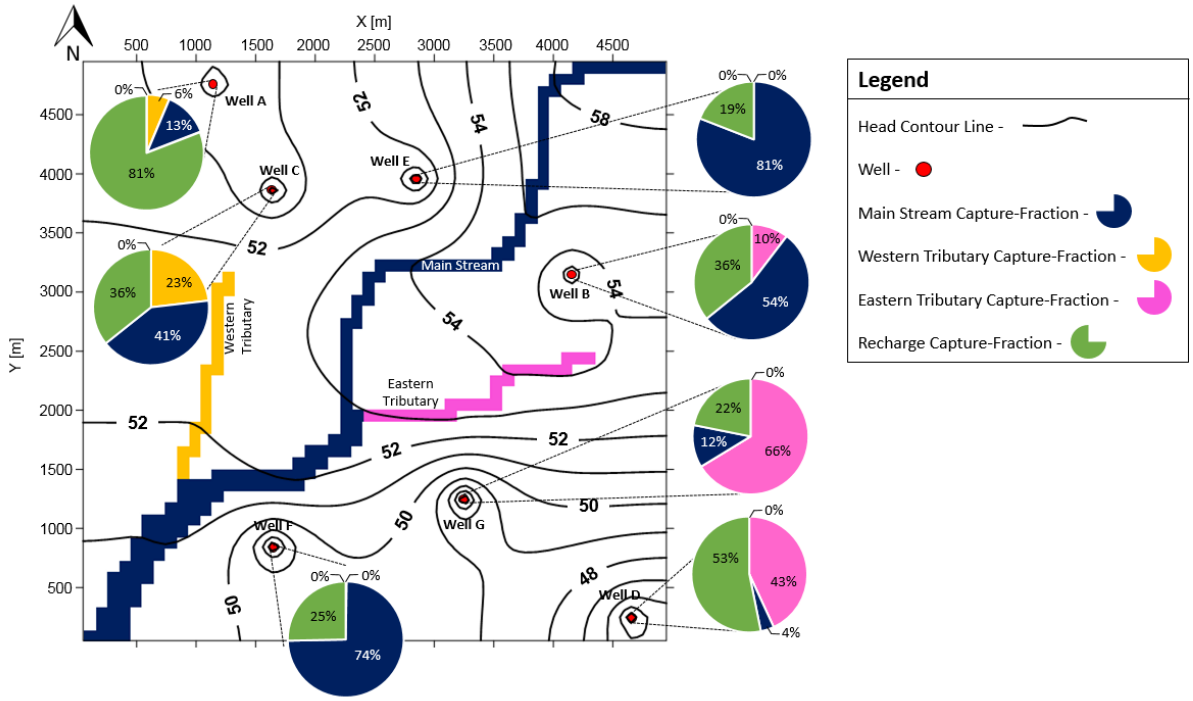

Figure 4.22. Map illustrating connectivity of wells to specified features of interest: the main stream, the Eastern tributary, and the Western tributary.

From Figure 4.22, we may infer which feature of interest each well is at most risk of being contaminated by. For example, the Eastern tributary poses the greatest contamination threat to Well G and Well D, while the main stream is the sole contamination threat for Well E and Well F. Well C derives some water from the Western tributary, but it too is at a greater risk of contamination from the main stream. Now, to illustrate the pumping impacts, Figure 4.23 shows graphs of the daily rates of water removal from the specified features of interest by each well and the cumulative daily removal rates from each feature of interest.

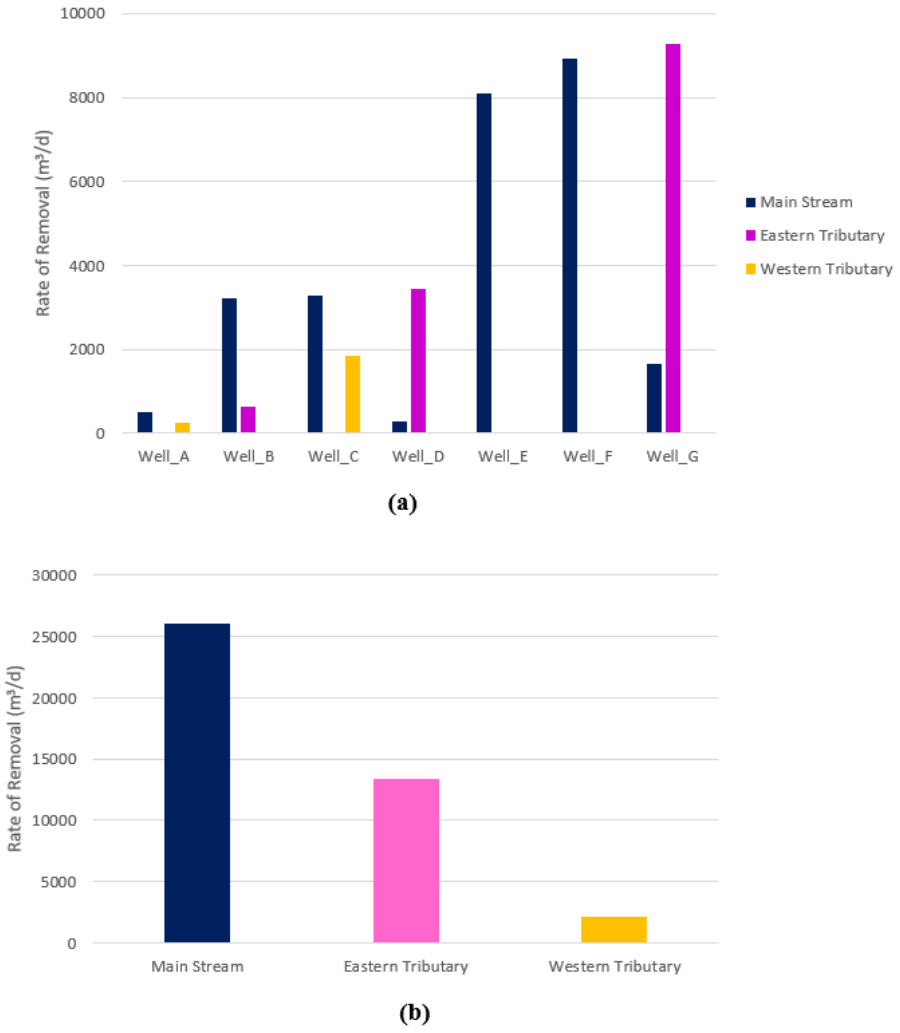

Figure 4.23. Daily rate of water removal by each well from features of interest (a), and the cumulative daily rates of water removal from each feature of interest (b).

Unsurprisingly the highest rates of water removal are at the Eastern tributary and the main stream, which are adjacent to the three wells with the highest pumping rates (i.e., Well G at 14,000 m^3/d near the downstream reach of the Eastern tributary, Well F at 12,000 m^3/d near the downstream reaches of the main stream, and Well E at 10,000 m^3/d near the upstream reaches of the main stream).

Now, the vulnerability of the wells (i.e., which wells are likely to be surface-water dominated) and their pumping impacts (i.e., where the highest rates of removal will be) for this

simple case need not necessarily be inferred from the figures presented here, since they are apparent simply from the pumping rates of the wells and their proximities to the stream. However, what is noteworthy is that the tool provides quantitative estimates of the total volume of well water derived from user-specified features of interest without having conducted any particle tracking or solute transport simulation. This represents a novel contribution for determining the degree of well and surface-water connectivity and consequently for the management of groundwater resources. Generating the estimates of the volumetric capture rates cost seven FlowSource runs, one for each well and the average of which was on the order of ten times the MODFLOW-2000 run for the model. The time taken to establish the volumetric capture from features of interest is negligible as it simply entails reading the FlowSource output files and summing the metrics for the cells comprising the features of interest. Thus, provided a model exists, the tool can provide estimates of the volumetric capture rates from user-specified features of interest. The accuracy of the estimates will depend on how well characterized the model is and obviously the number of active model cells and features of interest will affect the time required to obtain the estimates. Transient models can also be used and volumetric capture-rates may be obtained for specific time periods or the 'maximum' option in FlowSource may be selected to obtain the maximum volumetric capture rates for the entire simulation. However the results should be interpreted with caution since FlowSource treats transient models as quasi steady-state.

4.3.2 Assessing Connectivity to Non-Point Source Pollution

For the discussion in Section 4.3.1, the features of interest were restricted to the stream. However, that need not be the case. The ability to specify any cell as a feature of interest, provided that the feature lies entirely within one layer, affords another useful application – the

determination of the fraction of recharge flowing through potentially threatening agricultural or industrial lands that reaches the wells. Since in this case it is necessary to evaluate the fractional volume passing through the cells of interest that is ultimately captured at the well, we use the 'fraction-through' metric in FlowSource. To illustrate, let us assume that there are two hypothetical parcels of agricultural lands known not to employ best management practices: Agri A and Agri B. Note, best management practices refer to the use of accepted equipment, facilities and/or farming methods that may reduce and/or prohibit the discharge of harmful contaminants generated at the farm to the environment. Figure 4.24 shows a map with estimates of the volumetric fractions captured by each well from the two farms. Agri A is located west of the headwaters of the main stream, shaded brown in Figure 4.24, and Agri B is located east of the headwaters of the Eastern tributary, shaded green in Figure 4.24.

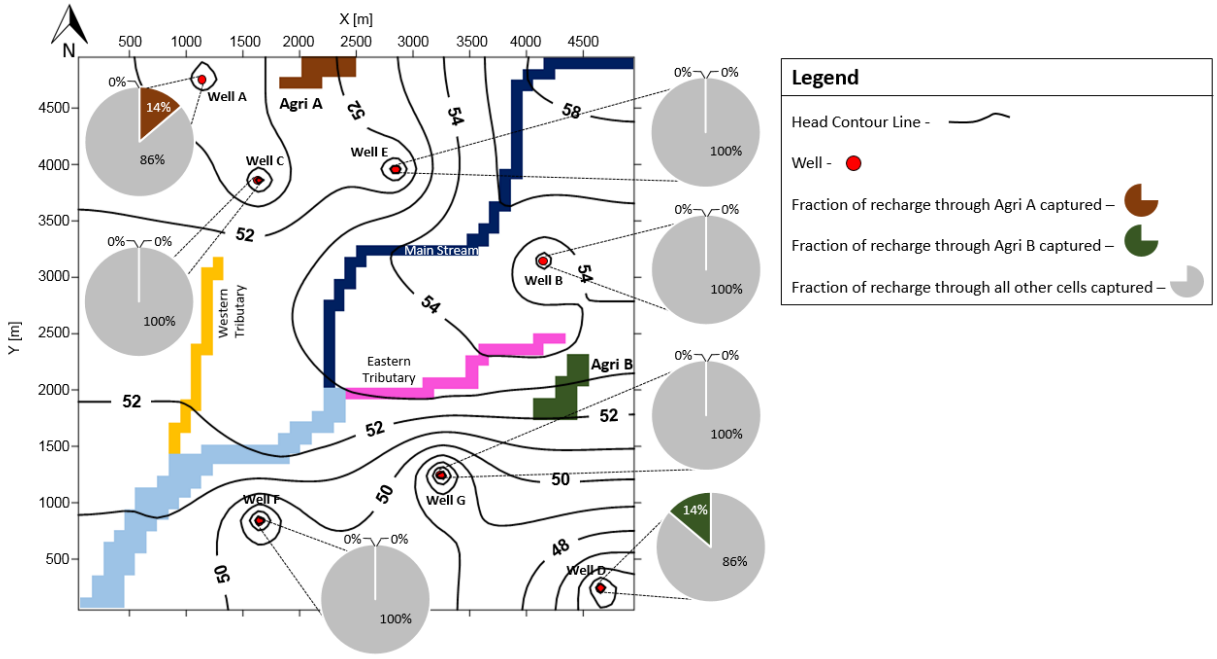

Figure 4.24. Map illustrating the fraction of recharge obtained by each well from adjacent farms.

Figure 4.24 shows that recharge flowing through Agri A is captured only by Well A, while recharge flowing through Agri B is captured only by Well D. The other wells do not draw any

recharge that has flowed through either of the agricultural lands. Recall from earlier that Well A and Well D were the only wells that were not surface-water dominated. So, while the stream may not pose as great a threat to these wells, they may be deemed vulnerable on account of the threat posed from Agri A and Agri B respectively.

4.4 Applications for Planning New Well Sites

The second type of applications of the tool lie in the planning of new well sites. For these applications, FlowSource is deployed in the framework of the LRD-method to generate contour maps of the spatial distribution of volumetric capture-fraction of a new pumping well from user-specified features of interest. The same synthetic steady-state MODFLOW-2000 model shown in Figure 4.20 is used to demonstrate the various applications. The details of the model setup are outlined in Table 4.7 and Table 4.8.

4.4.1 Volumetric Capture-Fraction Contour Maps

The volumetric capture-fraction contour maps for the stream were generated for a well with a constant pumping rate of 2,000 m^3/d for 180 days. A single stress period was specified with six time steps. Pumping locations were considered in every second row and every second column, requiring 625 MODFLOW and FlowSource runs each. Again, the 'fraction-from' metric of FlowSource was used for the maps. Figure 4.25 shows the contour maps for pumping in layer 1 and layer 2 of the model after 180 days. The 50% capture-fraction contours are indicated with dark black lines. Also note, that the well is supplied by capture from the stream, areal recharge and transient storage.

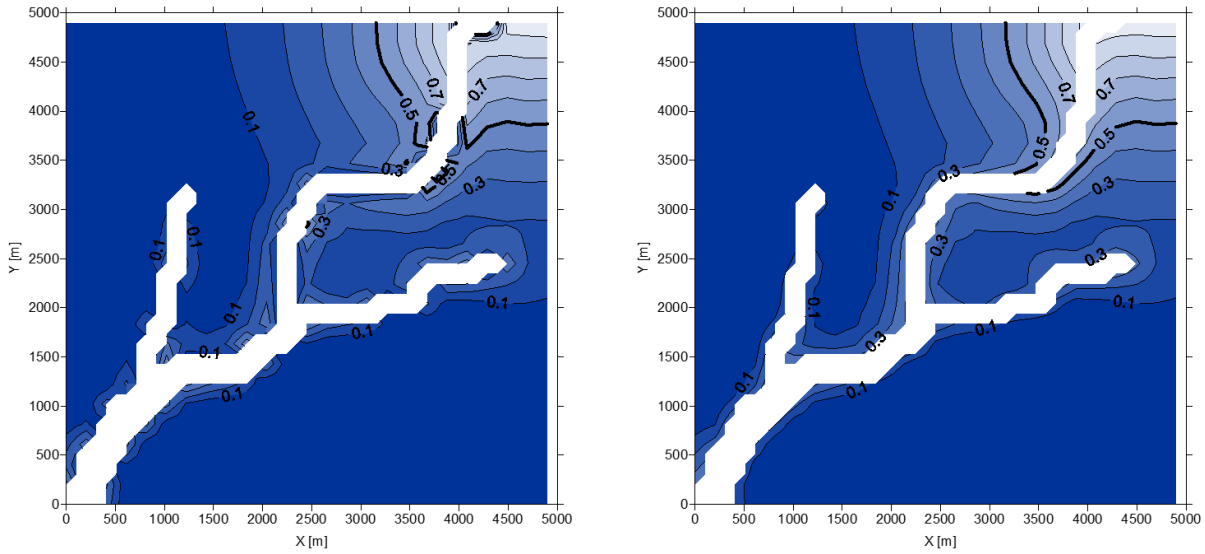

Figure 4.25. Contour maps of fractional volumetric capture from the whole stream after 180 days of pumping at 2,000 m^3/d along layer 1 (a), and layer (2).

To generate the contour map of the whole stream along layer, shown in Figure 4.25 (a), took 177 seconds, where the MODFLOW runs accounted for 56% of the time, the FlowSource runs accounted for 43% of the time and the map generation took the remaining 1%. The total time was on the order of 1,500 times a single MODFLOW run. The cost of generating a single map is a factor of the model size, number of stress periods and time steps, and the desired resolution of the map.

Again, if we are concerned about capture from specific reaches of the stream, reach-specific maps may be generated as well. Figure 4.26 shows a map of three stream reaches that were defined as features of interest: the main tributary, the Western tributary, and the Eastern tributary. Figure 4.27, Figure 4.28, and Figure 4.29 show the corresponding contour maps respectively. The setup of the runs were the same as of one used for generating the maps for the whole stream.

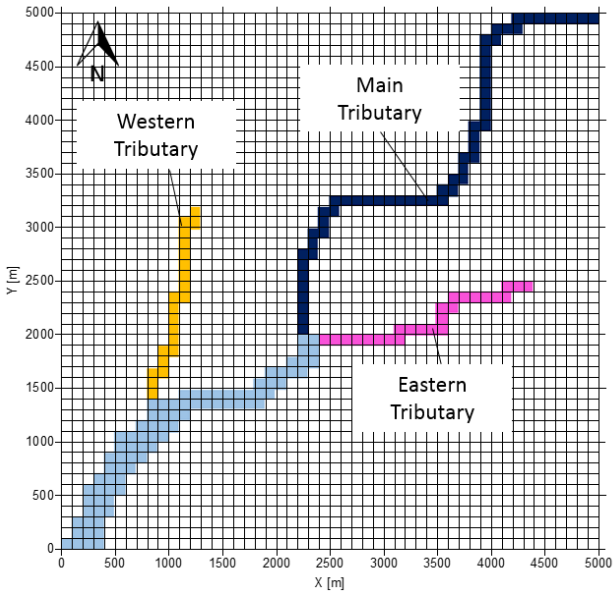

Figure 4.26. Specified reaches of interest along the stream for contour maps: the main tributary (cells shaded dark blue), the Western tributary (cells shaded yellow), and the Eastern tributary (cells shaded pink).

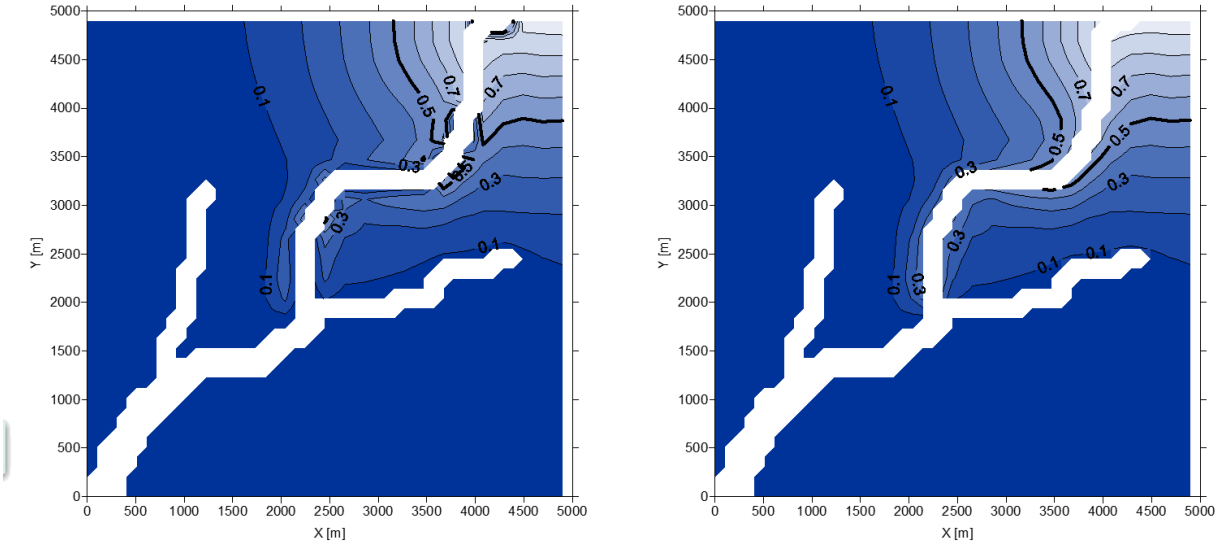

Figure 4.27. Contour maps of fractional volumetric capture from the main tributary after 180 days of pumping at 2,000 m^3/d along layer 1 (a), and layer (2).

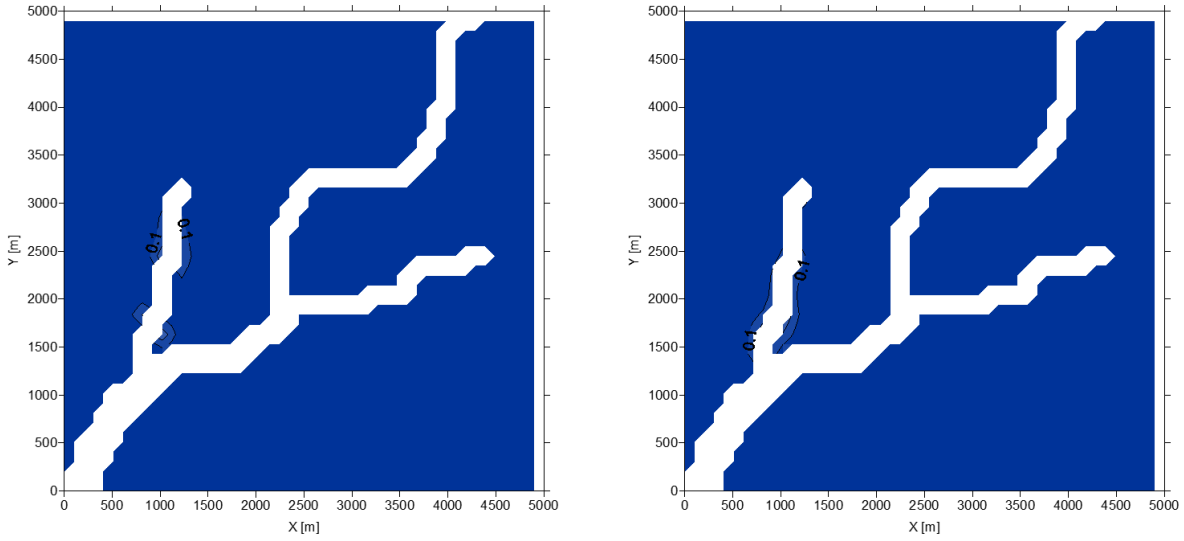

Figure 4.28. Contour maps of fractional volumetric capture from the Western tributary after 180 days of pumping at 2,000 m^3/d along layer 1 (a), and layer (2).

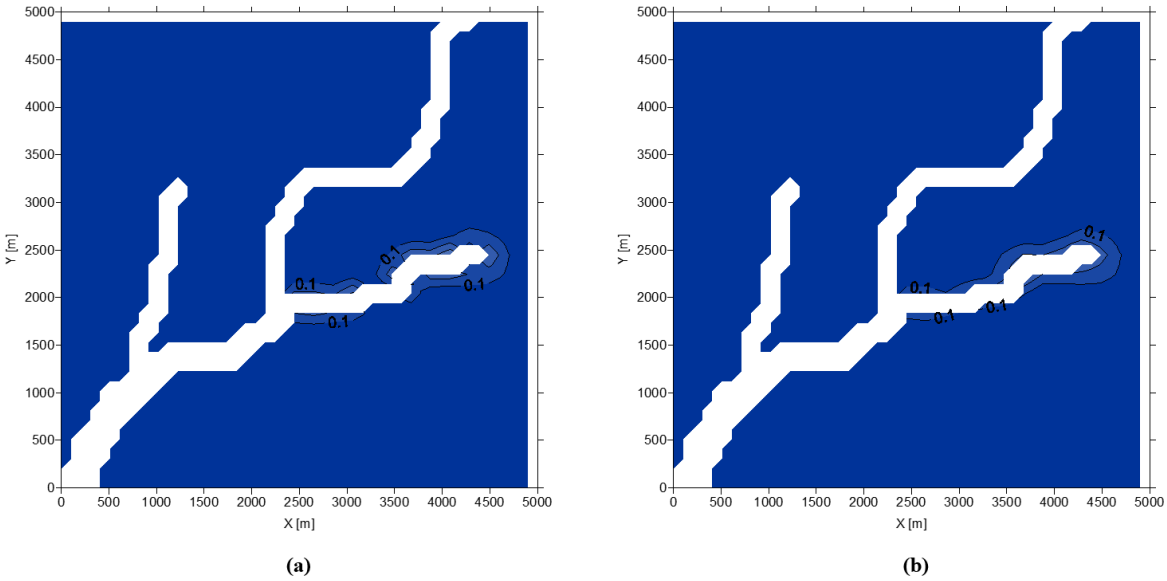

Figure 4.29. Contour maps of fractional volumetric capture from the Eastern tributary after 180 days of pumping at 2,000 m^3/d along layer 1 (a), and layer (2).

Thus, for each specified reach an area can be delineated within the model domain for the placement of a new well such that it obtains the least amount of water from that reach.

So, where the maps generated using the LRD-method show how the location of pumping and time since pumping began affect capture, these maps show how those same factors affect the

degree of well connectivity with surface-water. Importantly, it is not necessary to understand the concept of capture to interpret these maps. The information they convey is simple – how the location of the well and time since pumping began, affects the fraction of water that it will derive from surface-water. This is something that may be communicated to a non-technical audience with relative ease. The other important takeaway from these maps is that they provide clear delineation of areas within which a new well can be drilled such that it will not be surface-water dominated (e.g., less than 50% of the well water will be derived from surface-water).

4.4.2 Impact of Seasonality

The contour maps may be used to demonstrate the impact of seasonality on the connectivity of wells to surface-water. To illustrate, consider the contour maps of volumetric capture from the stream for pumping at 11,000 m^3/d along layer 2 for 180 days under three different magnitudes of uniform areal recharge: 2e-03 m/d, 1e-03 m/d, and 5e-04 m/d for pumping, as shown in Figure 4.30.

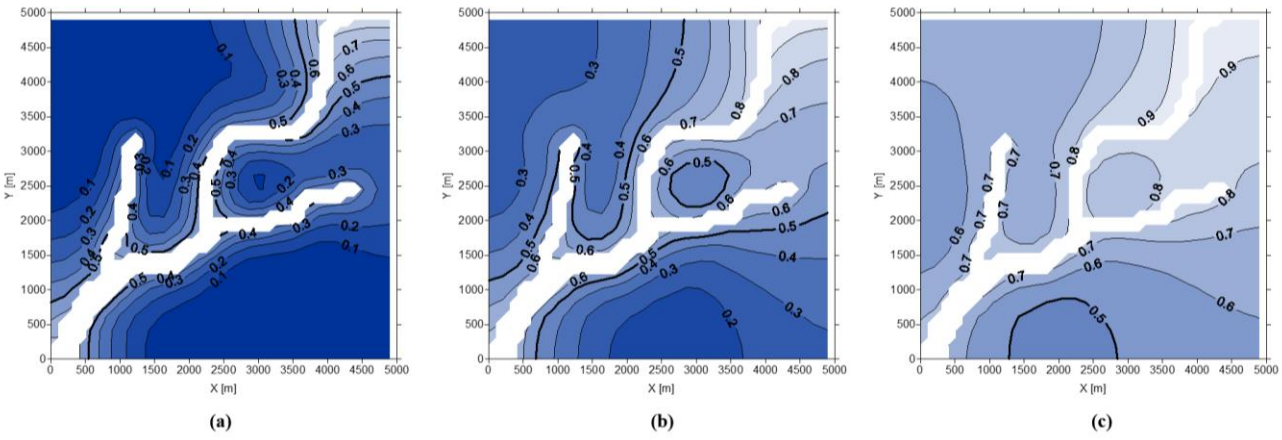

Figure 4.30. Contour maps of fractional volumetric capture from whole stream after 180 days of pumping at 11,000 m^3/d along layer 2 under uniform areal recharge of 2e-03 m/d (a), 1e-03 m/d (b), and 5e-04 m/d (c).

As expected, the maps show that the volumetric capture increases as areal recharge decreases, since with lower recharge, a higher fraction of the withdrawn water needs to be supplied by the stream. These maps can provide insight into the sensitivity of capture areas to

changes in areal recharge. Note for this system, when the areal recharge rate is reduced by half from 1e-03 m/d to 5e-04 m/d, as shown in Figure 4.30 (b) and (c), the entire domain of the model becomes surface-water dominated. If the capture areas for a system change very drastically in response to changes in areal recharge, then water managers should ensure that the recharge is adequately characterized in the model.

4.4.3 Impact on Existing Wells

The tool can also generate contour maps showing how the location of a new pumping well may affect the surface-water connectivity of an existing well. The most surface-water dominated well, Well E, and the least surface-water dominated, Well A, as established from Section 4.3.1, were chosen for the demonstration. The wells are illustrated again on the map shown in Figure 4.31.

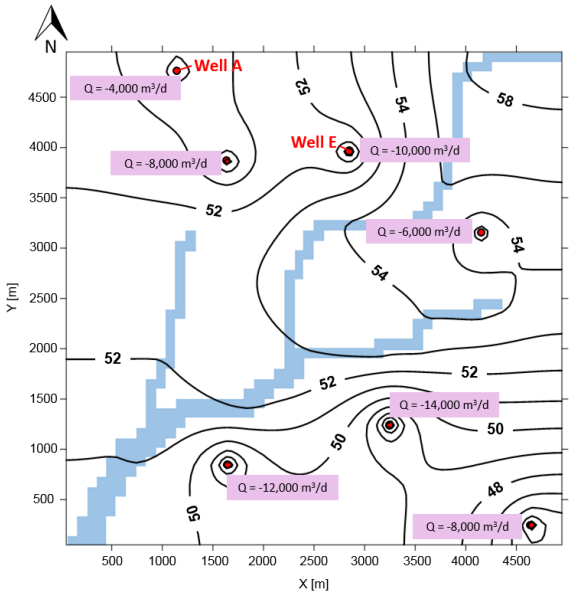

Figure 4.31. Locations of Well A and Well E; wells are indicated with red circles and the pumping rates of all the wells are shown adjacent to the well; the steady-state head distribution of layer 2 and the stream has also been overlaid the map.

Figure 4.32 shows contour maps of the how the volumetric capture-fraction from the stream would change in Well E and Well A from the addition of a new well pumping at a constant rate of 11,000 m^3/d for 180 days anywhere along layer 2.

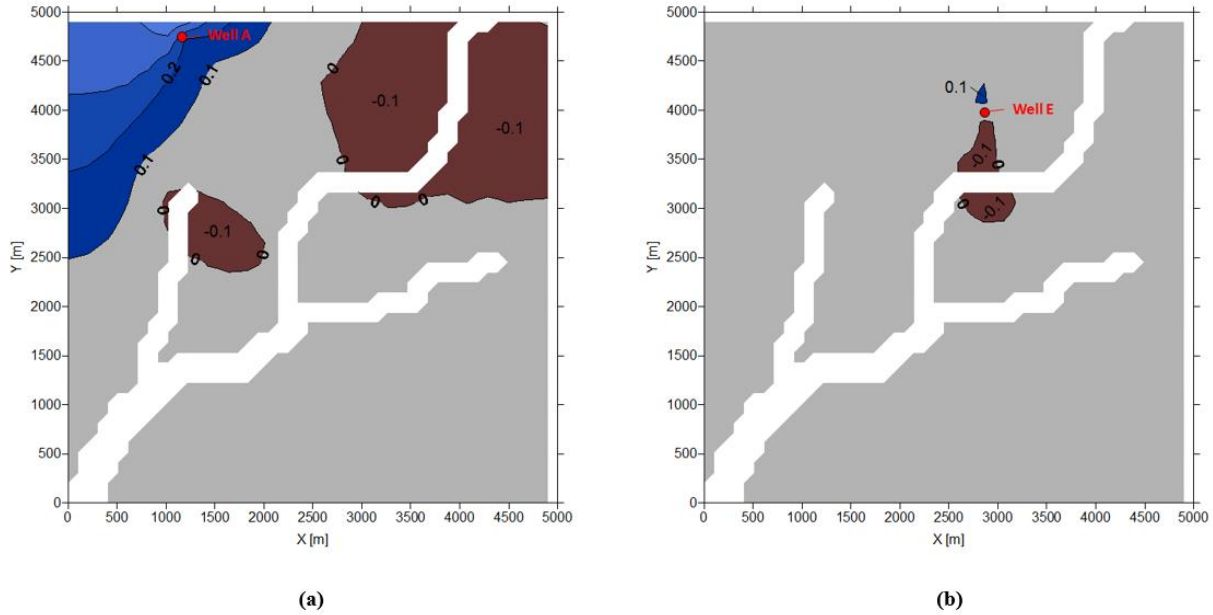

Figure 4.32. Change in volumetric-capture fraction in Well A (a), and Well E (b) for pumping at 11,000 m^3/d along layer 2 for 180 days.

In Figure 4.32, the grey regions indicate the areas where the addition of the well would induce minimal changes in the volumetric composition of the water in the Well A and Well E, the blue regions indicate the areas where the addition of the new well would increase connectivity with the stream and the brown regions indicate areas that would induce decreased connectivity. Recall from Section 4.3.1, that Well A was the least surface-water dominated, with a volumetric-capture fraction of 19%. Figure 4.32 (a) shows that there is a region in the north end of the model domain where the addition of the new well would incur up to a 40% increase in the connectivity with the stream in Well A and thereby convert it into a surface-water dominated well. Conversely, Well E would be relatively unaffected by the addition of the new well.

Now, if the stream represented a source of contamination, then from the contour maps in Figure 4.32, we see clear delineation of areas where the addition of the new well would increase connectivity with the stream and thereby degrade the water quality in the two existing wells. Alternatively, if there was a contamination plume in the aquifer nearby the existing wells and the stream represented a source of clean water, then it would be desirable to add a treatment well in those same areas to drive the existing wells to draw more water from the stream and less from storage and recharge.

4.4.4 Impact on Hyporheic Flows

The hyporheic zone refers to the interface between surface-water and deep groundwater (Boulton et al., 1998). Hyporheic zones typically exist where there are abrupt changes in the stream geometry (i.e., either the streambed slope or sharp meanders) and "the stream water flows through short segments of its adjacent bed and banks", as illustrated in Figure 4.33 (Winter et al., 1998).

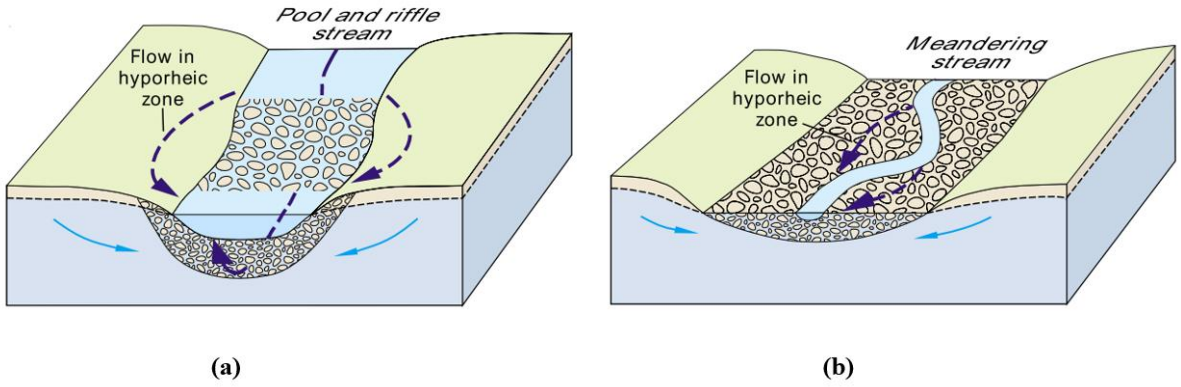

Figure 4.33. Manifestation of hyporheic zones due to abrupt changes in streambed slope (a) and stream meanders (b) (modified from Winter et al., 1998)

The hyporheic zone serves important stream ecosystem functions such as facilitating primary productivity and nutrient cycling, and supporting diverse microbe and invertebrate communities and fish spawning habitats (Wondzell, 2011). The modeling tool developed here

can provide insight into how flows within hyporheic zones may be affected as a result of pumping. For example, consider the two reaches of the stream from the synthetic model shown in Figure 4.34. The steady-state head distribution for layer 1 shows that the meandering of the stream may support hyporheic flow from Reach A to Reach B.

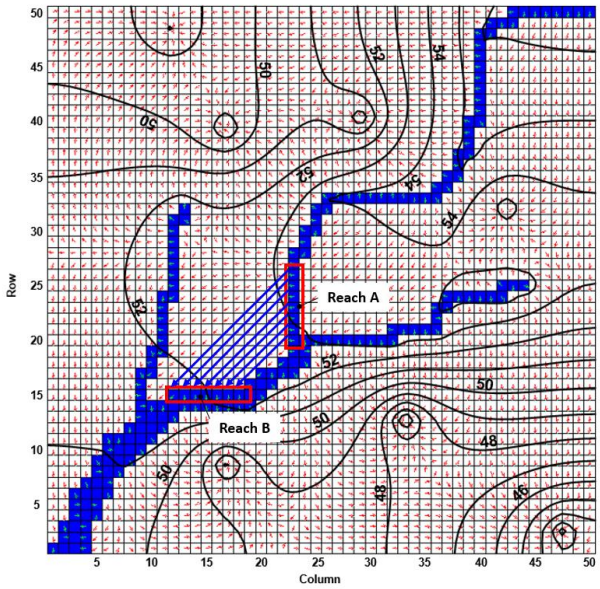

Figure 4.34. Potential hyporheic zone between Reach A and Reach B of the synthetic model.

Using FlowSource, we may directly estimate the hyporheic flow from Reach A to Reach B at a given period in time (i.e., the volume of flow passing through the cells in Reach A that ultimately ends up in the cells in Reach B). Under steady-state conditions, this was computed to be 11 m^3/d. In addition, we can generate contour maps using the 'volume-through' metric of FlowSource to demonstrate the how the volumetric flow within the identified hyporheic zone would change as a result of pumping at 11,000 m^3/d for 180 days along layer 2. This is shown in Figure 4.356. In Figure 4.35, the grey region indicates the area where the pumping would induce minimal changes in the flows from Reach A to Reach B, the blue region indicate the areas where it would increase hyporheic flow between the two reaches and the pink region indicate areas that

would induce decreased hyporheic flow. As expected, the greatest reduction would result from pumping anywhere directly within the area where the hyporheic flow occurs.

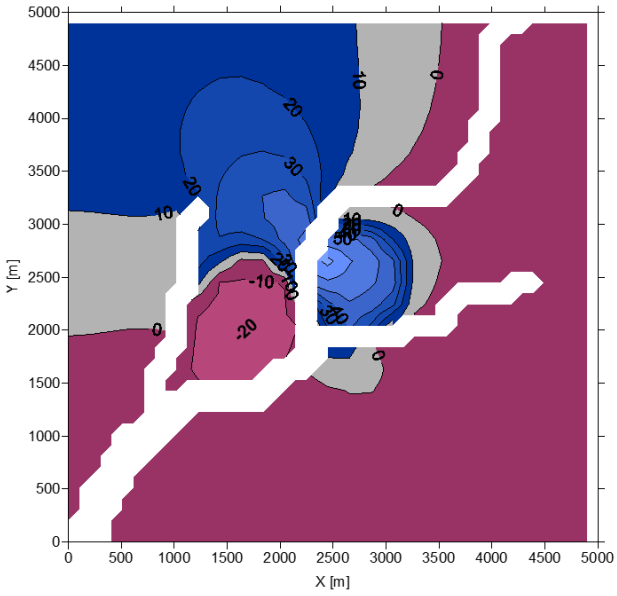

Figure 4.35. Change in hyporheic flow (m^3/d) from Reach A to Reach B after 180 days for pumping at 11,000 m^3/d along layer 2.

The applications of FlowSource are not necessarily limited to examining the impact of pumping on hyporheic flows. Hyporheic zones are an active area of research and an important theme is the difficulty in determining the boundaries of hyporheic zones and characterizing the flows within (Boulton et al., 1998; Wondzell, 2011). In this regard, FlowSource can be used to determine the maximum and minimum flows that occur over a given time period within the hyporheic zone between two reaches. Additionally, different cells may be tagged in a reach and using the always/sometimes/never metric, it would be possible to determine if any of the cells in that reach convey any flows to other specified reaches over the course of the simulation.

Chapter 5

Conclusions and Recommendations

The first part of the work in this thesis entailed the development and testing of a method to reduce numerical dispersion in FlowSource (Black and Foley, 2013) calculations that result from the assumption of fully mixed groundwater model cells. A method was developed to determine the volumetric flow connections between all the faces of a three-dimensional rectilinear finite-difference cell by either applying mass balance inside the cell or analytically recreating the internal streamtube geometry using extensions of the equations from Pollock's semi-analytical particle tracking method (Pollock, 1988). The method inherits simple linear interpolation of the velocity vector inside the cell from Pollock's method and assumes that there are no zero-velocity gradients inside the cell. When zero-velocity gradients are present in all three coordinate directions inside the cell, which represents a very specific group of cases, a low magnitude flow correction is applied. A flow correction of 0.009% was found to yield near exact results for all zero-velocity gradient cases. In addition, the method assumes that there is no internal addition or removal of water inside the cell (i.e., no weak sinks or sources), which is a condition that may not be violated. The method has been embedded into an algorithm to produce all the volumetric flow connections inside a single model cell for any given set of flows along the cell faces.

A number of single cell test cases were shown to demonstrate that the algorithm can accurately determine the volumetric flow connections inside the cells. The performance of the algorithm using an unoptimized code is on the order of or less than a single MODFLOW (Harbaugh et al., 2000) simulation.

As the actual incorporation of the algorithm into FlowSource was outside the scope of this research, its potential to reduce numerical dispersion issues in FlowSource was demonstrated with a hypothetical case with planar flow. Using the existing FlowSource, the whole domain of the hypothetical case is determined to be contributing some flow to the 'destination cell', or the cell at which all the water is extracted. However, if the dividing streamtubes that develop inside the cells are taken into account, it can be seen that periphery cells that do not have any advective flow lines flowing into the destination cell become included in the existing FlowSource calculations as a result of the fully mixed assumption. Using the algorithm on a cell-by-cell basis to represent each cell face flow as the sum of all its 'un-mixed' components prior to performing the flow connectivity calculations in FlowSource, it was demonstrated that the actual area from which the destination cell derives its water from can be accurately determined. Thus, the algorithm can serve as suitable solution to address the numerical dispersion issues in FlowSource.

Of course, the actual effectiveness of the method can only be determined once it has been successfully incorporated into FlowSource. As such, future work would entail comparing results of the existing FlowSource with the updated version for a model with varying grid sizes to examine the amount of reduction in numerical dispersion from the implementation of the algorithm and the corresponding computational cost.

The second part of the work in this thesis entailed the development of a computer program that uses FlowSource to assess the degree of hydraulic connectivity of groundwater wells to adjacent surface-water features. Most notably, the use of FlowSource enables a direct quantitative estimation of the degree of well and surface-water connectivity without the use of any particle tracking or solute transport modeling. The computer program, referred to here as the

modeling tool, is MODFLOW-based and has two general features: (1) computing the volume of water, or fraction thereof, in a well that is derived from user-specified features of interest, where the feature has to be contained entirely within one model layer and, (2) generating contour maps that show how the location of pumping and time since pumping began affect the connectivity wells and surface-water. In the latter case, FlowSource is deployed in a manner similar to the mapping method developed by Leake et al. (2010), referred to here as the LRD method. FlowSource enables quantification of the total volume of water a well sources from surface-water, whereas the LRD method provides only the volume of water that will reach the well as a result of pumping (i.e., the pumping induced stream leakage, which does not account for the water that reaches the well due to natural hydraulic gradients).

Numerous applications of the modeling tool were demonstrated using a synthetic model. For example, an existing well field may be screened rapidly to determine which wells are surface-water dominated (i.e., more than 50% of its water is derived from surface-water). The impact on the connected surface-water features may also be inferred implicitly from this information – since the volume of water that each well sources from surface-water is known, it is possible to determine the rates at which water is removed from adjacent surface-water bodies. In addition, the features of interest need not be surface-water. As long as the feature does not span multiple layers, any model cell can be assigned as a feature of interest. Thus, it is possible to determine which wells are most at risk of contamination from non-point sources of pollution (i.e., the volumetric fractions of water in each well that is derived from recharge that has passed through the cells underlying adjacent agricultural lands). The information obtained can be portrayed on a map of the well site to visually depict the degree of connectivity of the wells to features of interest.

The contour maps generated using the modeling tool can not only be used to illustrate how the location and time of pumping affects volumetric connectivity with surface-water features, but also how this connectivity is impacted by seasonality (i.e., changing areal recharge), how it affects the connectivity of existing wells to surface-water, and even how it may affect hyporheic flows. The maps are also easy to interpret and may be compatible for use with non-technical audiences. To generate the maps a large number of model runs are required, which may be on the order of a hundred and upwards depending on the size of the model. Nevertheless, since run times of both MODFLOW and FlowSource are very quick, the cost of generating a contour maps is relatively inexpensive (i.e., for the synthetic model used, it was 1,500 times a single MODFLOW run, which amounted to approximately three minutes). Hence, the modeling tool developed here can aid water managers to rapidly and accurately screen for wells that may potentially become GUDI and/or adversely impact connected surface-water features and also assess the threats posed to public health and local ecology by new pumping operations.

Again, the true utility of the modeling tool can only be realized once it has been applied to a real world scenario. Consequently, it is recommended to extend the study to first attempt to successfully demonstrate the same applications shown here with a real world model and then use that same model to determine well and surface-water hydraulic connectivity using a solute transport modeling approach (i.e., a tracer study). The results of the latter should be compared to those of the modeling tool to assess its effectiveness. Furthermore, the modeling tool should be developed to handle features that span multiple layers, which would enable it to determine the hydraulic connectivity of wells not only to surface-water but also subsurface contaminant plumes, thereby making it an invaluable assessment tool for well protection and management.

References

Alberta Environment, Drinking Water Branch, Environmental Policy Branch, Environmental Assurance Branch. (2006). *Assessment Guideline for Groundwater Under the Direct Influence of Surface Water (GWUDI); Appendix E of Standards and Guidelines for Municipal Waterworks, Wastewater and Storm Drainage System*. Pub. No.: T/840, ISBN 0-7785-4395-1

Anderson, E. I. (2000). The method of images for leaky boundaries. Advances in Water Resources, 23 (5), 461–474.

Anderson, M. P., Woessner W. W., and Hunt, R. J. (2015). Applied Groundwater Modeling: Simulation of Flow and Advetictive Transport. 2nd ed. Academic Press. ISBN: 978-0-12-058103-0

Asadi-Aghbolaghi, M., Rakhshandehroo, G. R., and Kompani-Zare, M. (2013). An analytical approach to capture zone delineation for a well near a stream with a leaky layer. *Hydrological Sciences Journal*, *58*(8), 1813–1823. doi:10.1080/02626667.2013.840725

Bakker, M. and Anderson, E. I. (2003). Steady flow to a well near a stream with a leaky bed. *Ground Water*, 41 (6), 833–840.

Bakker, M., and Strack, O. (1996). Capturte zone delineation in two-demensional groundwater flow models. *Water Resources Management*, *30*(5), 1309–1315.

B.C. Ministry of Health (MOH). (2005). *Guidance document for determining ground water at risk of containing pathogens (GARP), version 2.*

Black, A., and Foley, C. (2013). FlowSource: A program to efficiently delineate volumetric capture areas , pathways and source areas in groundwater models. In *MODFLOW and More 2013: Translating Science into Practice*.

Boulton, A., Findlay, S., and Marmonier, P. (1998). The functional significance of the hyporheic zone in streams and rivers. Annual Review of Ecology and Systematics, 29(1998), 59–81. doi:10.1146/annurev.ecolsys.29.1.59

Ceric, A., and Haitjema, H. (2005). On using simple time-of-travel capture zone delineation methods. *Ground Water*, *43*(3), 408–412. doi:10.1111/j.1745-6584.2005.0035.x

Environmental Protection and Enhancement Act: Potable Water Regulation. (2003). Retreived from http://www.qp.alberta.ca/documents/Regs/2003_277.pdf

Foley, C., and Black, A. (2013). Efficiently delineating volumetric capture areas and flow pathways using directed acyclic graphs and MODFLOW; description of the algorithms within FlowSource. In *MODFLOW and More 2013: Translating Science into Practice*.

Frind, E. O., Muhammad, D. S., and Molson, J. W. (2002). Delineation of Three-Dimensional Well Capture Zones for Complex Mutli-Aquifer Systems. *Ground Water*, *40*(6), 586–598.

Government of Newfoundland and Labrador. (2013). Groundwater Under Direct Influence of Surface Water (GUDI) – an Evaluation for Public Water Supplies in Newfoundland and Labrador. Halifax, NS.

Grubb, S. (1993). Analytical Model for Estimation of Steady-State Capture Zones of Pumping Wells in Confined and Unconfined Aquifers. *Ground Water*, *31*(1), 27–32.

Hantush, M. S. (1965). Wells near streams with semipervious beds. *Journal of Geophysical Research*, 70, 2829–2838.

Hunt, B. J. (1999). Unsteady stream depletion from ground water pumping. *Ground Water*, 37 (1), 98–102.

Harbaugh, A. W. (2005). MODFLOW-2005, The U.S. Geological Survey Modular Ground-Water Model — the Ground-Water Flow Process. *U.S. Geological Survey Techniques and Methods, Book 6-A16*. Reston, VA

Harbaugh, A. W., Banta, E. R., Hill, M. C., and Mcdonald, M. G. (2000). MODFLOW-2000, The U.S. Geological Survery Modular Ground-Water Model User Guide to Modularization Concepts and Ground-Water Flow Process. *U.S. Geological Survey Open-File Rpeort 00-92*. Reston, VA

Harbaugh, A. W., and McDonald, M. G. (1996). User's Documentation for MODFLOW-96, an update to the U.S. Geological Survey Modular Finite-Difference Ground-Water Flow Model. *U.S. Geological Survey Open-File Rpeort 00-92*. Reston, VA

Intaraprasong, T. and Zhan, H. (2009). A general framework of stream–aquifer interaction caused by variable stream stages. *Journal of Hydrology*, 373 (1–2), 112–121.

Keefe, S. H. (2004). Conservative and reactive solute transport in constructed wetlands. *Water Resources Research*, *40*(1), W01201. doi:10.1029/2003WR002130

Konikow, L. F. (2011). The Secret to Successful Solute-Transport Modeling. *Ground Water*, *49*(2), 144–159. doi:10.1111/j.1745-6584.2010.00764.x

Konikow, L. F., Goode, D. J., and Hornberger, G. Z. (1996). A three-dimensional method-of-characteristics solute-transport model (MOC3D). *U.S. Geological Survery Water-Resources Investigations Report 96-4267*. Reston, VA.

Leake, S. A., Reeves, H. W., and Dickinson, J. E. (2010). A New Capture Fraction Method to Map How Pumpage Affects Surface Water Flow. *Ground Water*, *48*(5), 690–700. doi:10.1111/j.1745-6584.2010.00701.x

McDonald, M. G., and Harbaugh, A. W. (1984). A modular three-dimensional finite-difference ground-water flow model. *U.S. Geological Survey Open-File Report 83-875*. doi:10.1016/0022-1694(86)90106-X

McDonald, M. G., and Harbaugh, A. W. (1988). A modular three-dimensional finite difference ground-water flow model. *Techniques of Water-Resources Investigations of the United States Geological Survey, Book 6-A1*. Washington. doi:10.1016/0022-1694(70)90079-X

McLane, C., and Cecan, L. (2009). Discussion of Papers - "MODALL: A Practical Tool for Designing and Optimizing Capture Systems," by Scott T. Potter, Elena Moreno-Barbero, and Craig E. Divine, March-April 2008, 46, no. 2:335-340. *Groundwater*, *47*(2), 172–173. doi:10.1016/j.echo.2015.07.024

Medema G. J., Shaw S., Waite M., Snozzi, M., Morreau A., and Grabow W. (2003). Catchment characterisation and source water quality. In *Assessing Microbial Safety of Drinking Water, Chapter 4, pp 111–158.* OECD, World Health Organization.

Nova Scotia Environment (2002). *Protocol for Determining Groundwater Under the Direct Influence of Surface Water.*

Ontario Ministry of Environment (2001). *Terms of Reference for Hydrogeological Study to Examine Groundwater Sources Potentially Under Direct Influence of Surface-Water.*

Ontario Ministry of Environment (2008). *Technical Rules: Assessment Report,* Clean Water Act, 2006.

Pollock, D. W. (1988). Semianalytical Computation of Path Lines for Finite-Difference Models. *Ground Water*, *26*(6), 743–750.

Potter, S. T., Moreno-Barbero, E., and Divine, C. E. (2008). MODALL: A practical tool for designing and optimizing capture systems. *Ground Water*, *46*(2), 335–340. doi:10.1111/j.1745-6584.2007.00410.x

Rock, G., and Kupfersberger, H. (2002). Numerical delineation of transient capture zones. *Journal of Hydrology, 269,* 134–149. doi:10.1016/S0022-1694(02)00238-X

Rushton, K. (2007). Representation in regional models of saturated river–aquifer interaction for gaining/losing rivers. Journal of Hydrology, 334 (1–2), 262–281

Saskatchewan Ministry of Environment. (2004). *Groundwater Under the Direct Influence of Surface Water (GUDI) Assessment Guideline.* EPB 284

Sophocleous, M. (2002). Interactions between groundwater and surface water: The state of the science. *Hydrogeology Journal*, *10*(1), 52–67. doi:10.1007/s10040-001-0170-8

Stauffer, P. H., and Stone, W. J. (2005). Surface Water–Groundwater Connection at the Los Alamos Canyon Weir Site. *Vadose Zone Journal*, *4*(3), 718. doi:10.2136/vzj2004.0121

The Environmental Management and Protection Act: The Water Regulations. (2002) Retreived from http://www.saskh2o.ca/DWBinder/Water_Regs_e10-21r1.pdf

Todd, D. K. (1980). Groundwater Hydrology. New York: John Wiley and Sons

U.S. Environmental Protection Agency (USEPA). (1992). Consensus method for determining groundwaters under the direct influence of surface water using microscopic particulate analysis (MPA). *Tech. Rep. EPA 9009-92-029*. Washington, D.C.

Winter, T. C., Harvey, J. W., Franke, O. L., and Alley, W. M. (1998). Ground water and surface water: A single resource. *U.S. Geological Survey Circular 1139*. Denver, CO.

Wondzell, S. M. (2011). The role of the hyporheic zone across stream networks. Hydrological Processes, 25(22), 3525–3532. doi:10.1002jhyp.8119

Zheng, C. (1994). Analysis of Particle Tracking Errors Associated with Spatial Discretization. *Groundwater, 32*(5), 821–828.